2016

Stress-induced Phase Change Sintering: A Novel Approach to the Fabrication of Barium Chloride Transparent Ceramic Scintillators

William Shoulders
University of Central Florida

STRESS-INDUCED PHASE CHANGE SINTERING:

A NOVEL APPROACH TO THE FABRICATION OF BARIUM CHLORIDE

TRANSPARENT CERAMIC SCINTILLATORS

by

WILLIAM TAYLOR SHOULDERS

BS Ceramic and Materials Engineering, Clemson University, 2011
MS Materials Science Engineering, University of Central Florida, 2013

A dissertation submitted in partial fulfillment of the requirements
for the degree of Doctor of Philosophy
in the Department of Materials Science Engineering
in the College of Engineering and Computer Science
at the University of Central Florida
Orlando, Florida

Fall Term
2016

Major Professor: Romain Gaume

ABSTRACT

For the precise in-field identification of dangerous radioisotopes, the desire for higher resolution, cheaper, and more rugged gamma-ray scintillator detectors has pushed the materials science community to investigate new compounds and processing techniques. One particular solution is Eu:$BaCl_2$ transparent ceramics processed by the novel phase-change sintering technique. Typically, optical transparency in $BaCl_2$ would be limited by birefringence scattering at grain boundaries due to mismatch in refractive index. Traditional ceramic processing routes would also predispose this volatile and hygroscopic material to the formation of defects, which interrupt the energy transfer in the scintillation process. Literature shows that these challenges have prevented halide gamma-ray scintillator ceramics, including Ce:$LaBr_3$, Eu:SrI_2, and Ce:Cs_2LiYCl_6, from reaching the performance of their single-crystalline counterparts. The sintering method explored in this thesis utilizes a polymorphic orthorhombic to cubic phase transition followed by plastic deformation. The experimental implementation of this method necessitated the design of a unique airtight hot-pressing device, capable of developing conditions for this phase conversion, and the synthesis of high purity powders. Systematic experiments on powder synthesis and on densification were carried out to demonstrate the feasibility of this approach and understand the conditions for phase-change sintering. These experiments, supported by characterizations including x-ray diffraction, electron microscopy, and thermal analysis, lead to the production of optically isotropic cubic barium chloride ceramic samples. Finally, the optical and scintillation properties of Eu:$BaCl_2$ ceramic samples were investigated, revealing an energy resolution of 6% at 662 keV, an unprecedented value for a halide ceramic scintillator.

I dedicate this thesis to my wife, Heidi Lindler Shoulders. She embarked on this journey with me from the very beginning with a reluctant move to Florida. Our marriage happened two years into my studies, so perhaps she has felt obligated to see this thing through. Regardless, she has displayed undeniable patience and delayed her own career and life goals in order to support me (emotionally and financially). We have both matured tremendously in our relationship and our respective careers during my studies. Although we may be a little older than most of our peers when we start a family and begin our first real jobs, we have at least have put in the extra effort to climb a few more rungs of the ladder to bring us closer to our dreams. Heidi, wherever in the universe our careers take us, I am happy to have you by my side.

ACKNOWLEDGMENTS

I began my graduate studies with an overinflated sense of my state of knowledge and a very stubborn approach. I am ever grateful for the support of my adviser, Romain Gaume, and the administration of both the College of Optics and the College of Engineering, who helped me move past the academic issues I brought upon myself during that first year. As Prof. Gaume's first student, I endured many of the growing pains of a new research group including moving all the lab equipment twice across campus. However, I wouldn't trade that experience with any other on account of all the learning and laughs that happened along the way. Many of these experiences were shared with the third founding member of the ceramics group at UCF, Dr. Samuel Paul David, who, above all else, passed on his always-positive outlook on science and beyond. Over the years the group welcomed more postdocs and students, who each contributed to my progress in their own way. I am also grateful for the opportunity to collaborate with scientists Gregory Bizarri and Edith Bourret-Courchesne at Lawrence Berkeley National Lab as well as Lynn Boatner at Oak Ridge National Lab. They were each grateful enough to host me for experiments related to my thesis work.

The technical aspects of my studies may have been the most critical, however I must thank my professors for their countless life lessons over the years. Your advice has confirmed and built upon that from my parents, who have been very supportive of my studies even though I have chosen a very different path than anyone else in the family. I could not have maintained my sanity during my studies if it weren't for my family and friends. Between the many runs shared with my wife and other Orlando running buddies and the concerts, festivals, and many other adventures shared with friends, I have been able to maintain a work-life balance.

I can say with confidence that my years at UCF have been the most formative to my career and life and I can't thank all of you enough for playing your part in making this a reality.

TABLE OF CONTENTS

LIST OF FIGURES

LIST OF TABLES

1. INTRODUCTION

Since the discovery of x-rays by W. Roentgen in 1895, using the visible fluorescence of $K_2Pt(CN)_4$ powder on a glass plate, the use of scintillators for the detection of ionizing radiations has proven most useful in medical imaging [1], high-energy physics [2], geophysical exploration [3] and to prevent the proliferation of nuclear weapons materials [4]. Despite the advent of other means of detection, these materials provide high detection efficiency due to their high radiation-stopping power. Since the turn of this century, resurgence in scintillator material research, mostly driven by applications in medical imaging and nuclear surveillance, has led to the development of an active research community.

This thesis work inscribes itself in this global effort to propose alternative methods for the scalable fabrication of high-performance inorganic scintillators. Our approach proposes the use of transparent ceramics as substitutes of single-crystals to lower manufacturing costs and increase active scintillator volumes. The present manuscript focuses specifically on the fabrication of Eu:$BaCl_2$ ceramics, a research that was part of a joint project with the Lawrence Berkeley National Laboratory, where this material, along with other high-performance barium-based scintillator materials have recently been discovered [5,6].

This first chapter provides a general overview of the scintillator characteristics as well as some recent developments in the fabrication of halide ceramic scintillators relevant to this work. This review aims at identifying the challenges associated to the fabrication of these materials and at outlining the concept of a novel sintering approach that we developed for Eu:$BaCl_2$.

1.1 Overview of scintillator characteristics

When a scintillator material is subjected to high-energy radiations, a sequence of processes lead to the emission of UV, visible or IR photons [7,8]. This energy conversion begins with the generation of electron-hole pairs during the interaction between the material and high-energy photons (Figure 1). The energy relaxation process involves core-valence transitions occurring deep within the valence band of the material, or the migration of the charge carriers to luminescent centers positioned within the forbidden bandgap of the material. In the case of bright scintillators for gamma spectroscopy, intra-bandgap luminescent centers, usually produced by doping, have the advantage of generating photons well-matched to the maximum efficiency of photo-detectors in the visible region, while core-valence transitions emit X-ray or deep UV wavelengths. Hence, the advantage of rare-earth dopants with allowed d-f level transitions, which emit in the visible. Other dopants or crystalline defects may also allow transitions in the visible, but d-f transitions have the advantage of being fast and efficient. In the case of $BaCl_2$, Eu^{2+}-doping has been found to provide good radioluminescence properties, as it is isovalent and shares a similar size with Ba^{2+} (r=130 and 147 pm, respectively) and has narrow 4d and 5f bands lying within the bandgap of the host material [9].

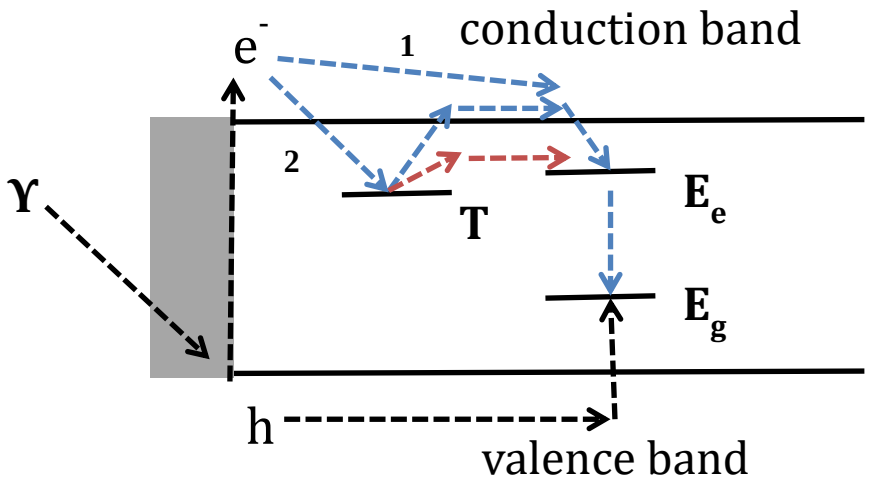

Figure 1 Electron trapping and recombination by (blue) excitation to the conduction band and (red) tunneling in scintillators. T represents a trap energy, while Ee and Eg represent the excited state and ground state of the luminescent center.

Scintillator materials used in gamma-spectroscopy require specific properties including high bulk and electronic densities, light yield and energy resolution:

- **Bulk density (ρ) and electronic density (Z_{eff}):** The density determines the thickness of material needed to fully stop gamma rays and ensures a maximum energy transfer by the photoelectric effect. A high electronic density is also needed to enhance the photoelectric conversion. The figure-of-merit for the photoelectric interaction scales as ρZ_{eff}^5 [7,8].

- **Light yield (Y):** The light yield is defined as the number of photons generated per unit of deposited energy (ph/MeV) and is related to the bandgap energy of the material: a narrow band gap material is required for a high light yield. Dorenbos has described a simple relationship for the dependence of light yield on the bandgap (E_g) [10].

$$Y = \frac{E_\gamma}{\beta E_g} SQ \tag{1.1}$$

where E_γ is the energy of an incident gamma ray; βE_g the energy required to create an electron-hole pair; S is the efficiency of the electron and hole thermalization process; and Q is the quantum yield of the electron-hole pair recombination. This inverse light yield-bandgap dependency explains why halides scintillators are usually brighter than most oxides compounds.

- **Energy resolution (R):** In a traditional gamma-ray spectroscopy experiment, the pulse-height spectrum is recorded and plotted in the form of a histogram pulse intensities as shown in Figure 2. The so-called photopeak, resulting from the full deposition of the gamma photon energy by photoelectric interaction, occurs at a position characteristic of the gamma energy, E_γ. The energy resolution of a scintillator is related to the variance in the number of visible photons generated at the photopeak. In a so-called 'proportional scintillator', the photopeak position on the channel number axis is linearly-related to the gamma energy of the incoming radiation.

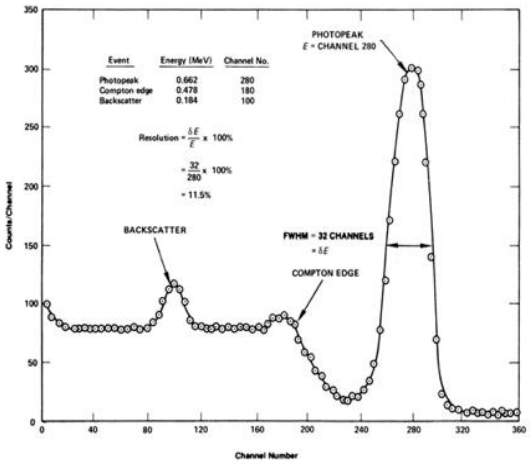

Figure 2 Example of a pulse-height spectrum obtained with Tl:NaI under ^{137}Cs excitation.

A large number of scintillator materials have been investigated and material discovery, either through experimental or theoretical means, is still an active part of research. To contextualize our interest for Eu:$BaCl_2$, it is worth looking at the development of halide scintillators. The interest for these materials started in the early 50s [11] with the use of thallium-doped sodium iodide, Tl:NaI, as gamma detectors. After over sixty years, Tl:NaI is still considered a reference material in the field, and used heavily in the medical and security industries. Later, another simple halide crystal, BaF_2, was found to have a sub-nanosecond decay component [12]. This material was commercialized for fast timing applications such as time of flight PET scanners, but possessed a very low light yield as expected for an intrinsic scintillator. For this reason, research trends moved towards rare-earth doping to achieve higher light yields. As another example, europium-doped CaF_2 has found applications as the scattering element in Compton cameras. It exhibits high sensitivity and high resolution but its use in gamma spectroscopy is limited due to its low Z_{eff} [13]. A string of exciting discoveries, including the dual thermal neutron and gamma ray scintillators from the elapasolite family and the bright and high resolution lanthanum bromide (Ce:$LaBr_3$) at TU Delft in the Netherlands in the late 1990s and early 2000s [14], was followed, in the late 2000s at LLNL, by the reinvestigation of the long forgotten scintillator compound SrI_2 [15], first identified by Hofstadter in the late 60s [16]. To this date, Ce:$LaBr_3$ and Eu:SrI_2 currently offer the highest light yields (80,000 and 110,000 ph/MeV, respectively) and best energy resolutions (2 to 3% at 662 keV) available in a scintillator. Ce:$LaBr_3$ is currently in the catalog of *Saint Gobain Crystals* under the name *BrilLanCe*, while the manufacture of Eu:SrI_2 and the elpasolites Ce:Cs_2LiYCl_6 (CLYC) and Ce:$Cs_2LiLaBr_6$ (CLLB) are still being evaluated by companies including *RMD, CapeSym* and *Saint Gobain*. It is more recently that promising alkaline-earth

halides, including Eu:$BaCl_2$, as well as Eu:BaBrI and Eu:$CsBa_2I_5$, were identified by both theoretical and experimental work at Lawrence Berkeley National Lab (LBNL) [6,17]. The reasons for this choice lie in the fact that barium is an abundant element and that its compounds are much less hygroscopic than some of the current gold-standards in the field, including Tl:NaI, Ce:$LaBr_3$ and Eu:SrI_2 (Table 1). It is believed that these attractive features might ultimately lower the fabrication costs.

Table 1 Properties of different halide scintillator materials under 662 keV irradiation.

Properties	**Tl:NaI**	**Ce:$LaBr_3$**	**Eu:SrI_2**	**Eu:$BaCl_2$**
Crystal symmetry	cubic	hexagonal	orthorhombic	orthorhombic
Density (g/cm^3)	3.67	5.1	4.55	3.89
Light yield (ph/MeV)	43,000	80,000	115,000	52,000
Energy resolution at 662 keV (%)	7	2.0	2.8	3.5
Hygroscopicity	High	High	High	Moderate
Reference	[18]	[14]	[15]	[19]

1.2 Transparent ceramic scintillators

Motivated in part by the high cost of single-crystal production[1], many recent research studies aimed at demonstrating the feasibility of transparent scintillator ceramics (Figure 3). Transparent ceramics are polycrystalline aggregates with macroscopically homogeneous refractive index, in which light can propagate freely. While their physical properties are similar to their

[1] Currently, it is estimated that Ce:$LaBr_3$ costs 20-40 times higher than Tl:NaI, with larger crystals having a higher cost gap. This price ratio can be attributed in part to the larger market, easier growability, higher growth yield and R&D amortization of Tl:NaI

single-crystalline counterparts, the ability to form these materials quickly[2] using near-net-shape and size-scalable processes (with methods including powder sintering, chemical-vapor deposition, and fusion-casting) has contributed to their success as armored vehicle windows, IR optics, missile domes [20–22], high-power laser gain media [23–26] and scintillators [27]. Studies targeting the scintillator application have focused on materials of cubic symmetry (optically isotropic) such as (Ce,Pr):$Y_3Al_5O_{12}$ (YAG) [28,29], Y_2O_3 [30,31], Lu_2O_3 [32], Ce:$La_2Hf_2O_7$ [33,34], Ce:$BaHfO_3$ [34], Ce:$(Gd,Y)_3(Al,Sc)_2(AlO4)_3$ [35], CLLB and CLYC [30], as well as on a few birefringent materials including Ce:Lu_2SiO_5 (LSO) [36], Ce:$LaBr_3$ [36] and Eu:SrI_2 [37].

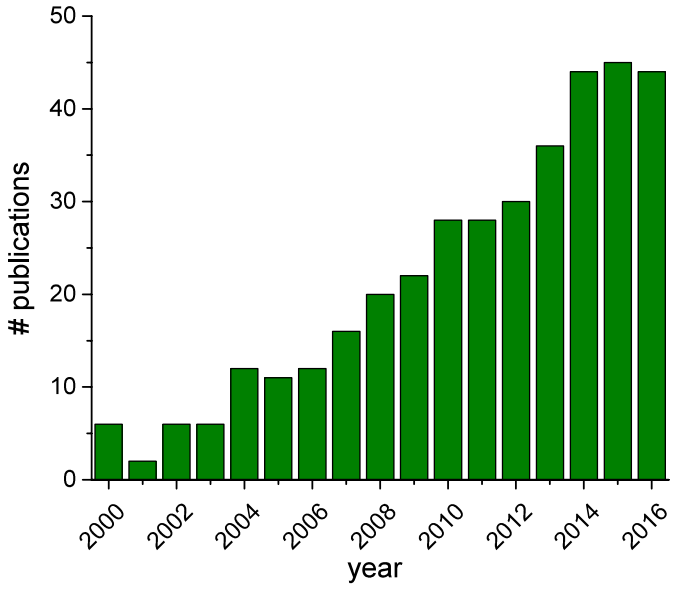

Figure 3 Publications satisfying a search for keywords 'ceramic' and 'scintillator' from 1988 to the present day on Web of Science

[2] Crystal growth runs can often take weeks to complete, while ceramic processes are usually no longer than a few days.

Most of the alkaline-earth halides are birefringent, with a mismatch in refractive index between the three principle directions on the order of 0.02. Specifically in orthorhombic barium chloride, the average difference is 0.012 [17,38,39] (Figure 5) between the three principle leading to significant scattering from birefringence at grain boundaries (Figure 4). To quantify this effect, it is useful to refer to the work of Apetz on Al_2O_3 ceramics using a combination of Rayleigh-Gans-Debye and Mie scattering theory [40].

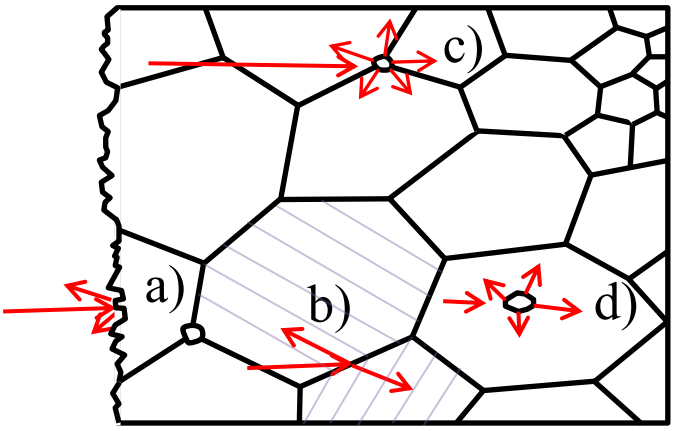

Figure 4 Schematic of the scattering sources in optical ceramics including a) Fresnel losses at the surface, b) birefringence at grain boundaries, c) pores at grain boundaries, and d) intragranular pores.

Example calculations for the dependence of scattering on both grain size and porosity in $BaCl_2$ are given in Figure 6 below. The models clearly show that smaller grain size helps the inline transmission approach the theoretical value, which accounts for Fresnel reflection losses. Likewise, the presence of just 0.1% porosity (99.9% density) shows a rapid decrease in transmission as the size of those pores increases. Experimental work on other optical ceramics have confirmed this trend of decreased scattering of visible wavelengths with decreased grain size

in the nanometer range [41]. That is not to say that acceptable scintillation performance cannot be achieved as long as absorption and trapping in the material are minimal.

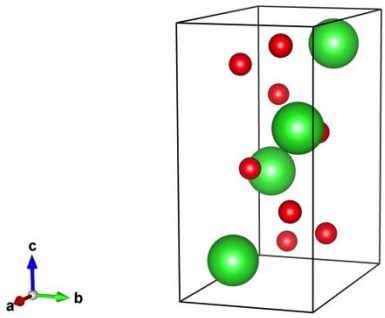

$n_a = 1.73024$

$n_b = 1.73611$

$n_c = 1.74196$

Figure 5 A representation of the orthorhombic cell of $BaCl_2$. The refractive indices of the orthorhombic phase are shown as reported in the Gmelin materials property handbook [42] at a wavelength of 589 nm.

To limit the effect of birefringence on the transmittance of ceramics, the use of so-called 'fine-grained' nanoceramics can be considered [22,43]. Yet, this strategy necessitates the development of new nanopowder preparation techniques that are often difficult to scale up, and drastic protocols to prevent surface contamination of these powders with high specific surface. Another pathway often pursued is the use of spark plasma sintering [44,45] or two step sintering [46] to lower the time a sample spends at high temperature and, in turn, limit grain growth. However, it is clear that the chemistry of halides studied in this thesis present a unique set of challenges beyond the control of microstructure and prevention of scattering.

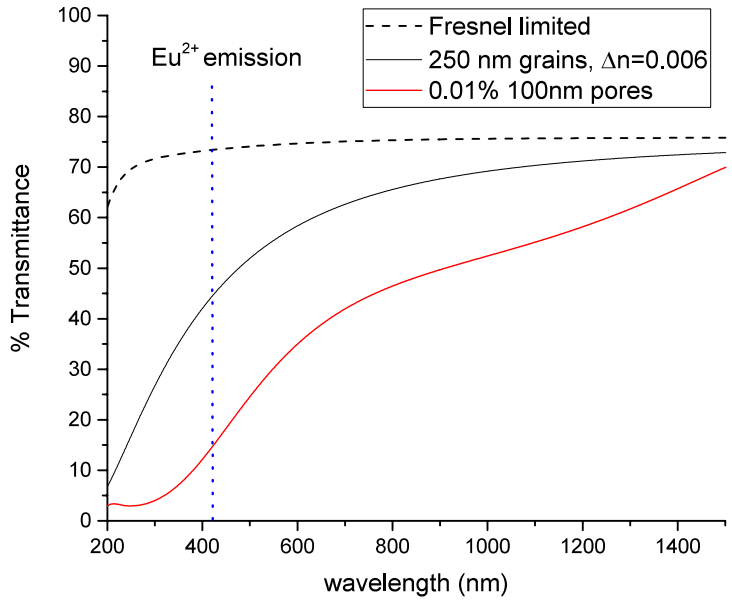

Figure 6 Theoretical inline transmission for a single crystal of $BaCl_2$ (dotted line), and ceramics accounting for scattering by grain boundaries (black line) and porosity (red line). The emission wavelength of europium (2+) is also shown to put the transmittance in the context of Eu:$BaCl_2$ scintillators.

1.3 Fabrication of polycrystalline halide ceramics

1.3.1 Atmosphere-sensitivity and defect formation

Most halide scintillators are atmosphere-sensitive. For example, moisture sensitivity generally increases moving down the halide group in the periodic table (iodides>bromides>chlorides>fluorides) [47], with a few exceptions like $LaBr_3$ which absorbs moisture at a rate 5x higher than materials like NaI [47,48]. While this drawback complicates the integration of a scintillator in a detector (off-the-shelf Tl:NaI scintillator modules typically arrive packaged in a sealed case to prevent atmospheric exposure), this sensitivity directly affects material fabrication due to possible moisture, CO_2 or O_2 pickup during processing. To avoid the formation of stable defects, that in turn, decrease performance, crystal growers handle materials

inside gloveboxes (<10 ppm H_2O and O_2 typically) and implement degassing steps. Experiments have shown that these steps are crucial to producing high quality colorless scintillation crystals. Ceramic studies have tried to the best of their ability to transfer these steps to their processes. However, hot-pressing and crystal-growth have some unavoidable differences in terms of cleanliness. Crystal-growth by the Bridgman-Stockbarger method for example involves the melting and controlled solidification of material inside a sealed ampoule. Once sealed, the materials remain confined during the entire processing. Hot-pressing, on the other hand, involves the transfer of powders loaded in a die (high surface area and high moisture sensitivity) from a glovebox, through air, and into a hot-press. This protocol is problematic as many optical materials are sensitive to residual moisture content as small as 40 ppm [49,50]. In scintillators specifically, low oxygen contamination levels have been shown to adversely affect optical absorption [51–54], electron trapping [55], and radiation hardness [56].

These defects are problematic because they trap electrons or holes and either prevent or slow the recombination process that results in the emission of light. In the alkaline earth halides, it is commonly known that one defect leading to electron trapping is the oxygen (O^-) interstitial associated with a neighboring anion vacancy (V^+). In addition, oxygen can act as an emission center, which is less efficient than rare-earth emission centers often used to achieve high brightness and energy resolution in gamma scintillation applications. Boatner *et al.* have reported a strategy of holding a melt of commercial SrI_2 raw material under vacuum for over 24 hours to establish stoichiometry before growing a crystal. As-received powders are showed to contain an excess of iodine [57,58]. Similar practices have been employed on $BaCl_2$, whereby raw powders must be outgassed at 150^{o}C under high-vacuum before crystal-growth [59].

We now briefly review various approaches for the fabrication of halide ceramics, and most specifically, $BaCl_2$.

1.3.2 Current fabrication approach: melt-quenched $BaCl_2$

Edgar's group at Victoria University, New Zealand, has used a variant of the fusion-casting technique to produce polycrystalline sample of cerium-doped $BaCl_2$. Their method consists in melting $BaCl_2$, and slowly cooling the melt through the cubic region of the phase diagram (925-960^oC), and then quickly quench to an optimized low temperature to prevent cracking [60–62]. It is not possible to quench the cubic phase in pure bulk $BaCl_2$, so alloying elements of La^{3+} and Ce^{3+} are added in amounts up to 12.5 atomic % to stabilize the cubic phase. The results show very high transparency, which is expected due in the absence of refractive index homogeneities and porosity, even though the grain size is expected to be very large. Impurities leading to coloration of samples are avoided by carrying out the melt-quench process in a sealed quartz ampoule. Nonetheless, scintillation measurements at 662 keV give a fairly poor energy resolution of 23%. This could perhaps be improved by defect engineering and exploring what roles intrinsic point defects as well as La^{3+} and Ce^{3+} play in the energy transfer. Colleagues at LBNL have extended the studies on casting and preliminary results point toward improved scintillation performance measured on samples such as that pictured in Figure 7. Although this particular processing route was not successful in providing high scintillation performance, it does highlight the orthorhombic-to-cubic phase transition in $BaCl_2$.

Figure 7 2x2 mm melt-quenched lanthanum stabilized, europium doped $BaCl_2$ ceramic synthesized at LBNL. The picture was provided by LBNL colleagues Drs. E. Bourret and Gregory Bizarri.

1.3.3 Possible fabrication approaches:

- **Press Forging:** In the technique of press-forging, a single-crystal is plastically deformed at high temperature to a point where dislocation pile-up and stacking faults force the material to recrystallize in the form of a polycrystalline body. The process occurs in radially-unconstrained conditions so as to allow for significant plastic deformation, much like in severe plastic deformation processes using rolling or equal channel angular pressing (ECAP) in metallurgy [63]. This technique has been successfully applied to CaF_2 laser ceramics [64] and NaI scintillators [65], and was also attempted on elpasolites [66]. The main advantage of this technique is the avoidance of porosity, because the starting material is already in a fully densified state. The main drawbacks relate to the looser control over microstructure during the recrystallization process, and the requirement of knowledge about the ductile to brittle transition temperature (DBTT), below which the crystals will be prone to cracking. Although temperature and pressure profiles can be used to control nucleation and growth of the new ceramic grains, as well as avoid fracture, the interdependency of these processes may cause issues in some systems. For example the appropriate forging range of ruby and sapphire crystals is very narrow leading up to their melting points and thus grain growth occurs

easily [67]. These methods have their niche in applications where high purity crystals are available and increased mechanical strength due to ceramic conversion is of utmost importance, however $BaCl_2$ is not easily grown, and good control over microstructure is important to limit the effects of birefringence.

- **Hot-pressing:** Sintering is the name given to thermally-driven powder densification processes traditionally used in the fabrication of ceramics. The driving force for powder densification, i.e. the elimination of porosity by matter transport, results from capillary forces due to curvature gradients at the surface of the pores, plastic or viscous flow. Concurrently to densification, however, elevated temperatures lead to grain and pore growth, thereby reducing the driving force of capillary-driven densification. Hence, ceramic densification strategies (including pressureless, vacuum, hot-pressing and field-assisted sintering techniques) consist in decoupling the kinetics of these two competitive processes to first promote the collapse of porosity before letting the microstructure coarsen. The halides have high volatility with sharp increases in vapor pressure under vaccum heating appearing as low as 350^{o}C [68], and thus will have an active vapor transport component to matter transport. Relying on the addition of externally applied pressure (hot-pressing) to counteract the negative effects of vapor transport is often necessary for halide ceramics. The fabrication of halide materials by hot-pressing has a long history of success. Over 30 years ago, General Electric (GE) investigated the compaction of Eu:BaFCl powders for gamma scintillators by hot-pressing powders at loads up to 5 GPa and temperatures from 20^{o}C up to 650^{o}C [69]. The high end of the pressure is not practical for reasonably sized (1" diameter and above) optical elements, however it is a good example of how moving beyond the pressure limits of conventional hot-pressing methods is

necessary. The defense industry has also been monumental in the development of halide ceramics, primarily for the production of infrared transparent windows and missile domes and very similar hot-pressing methods have been used by Eastman Kodak [70,71], Schott Glass Co. [72], and Bausch and Lomb [73] to produce magnesium fluoride (MgF_2), barium fluoride (BaF_2), and lithium fluoride (LiF). In fact, MgF_2 was a longtime commercial product under the name "Irtran-1" for Kodak. In the case of MgF_2, powders were filled into molybdenum, nickel-chromium, or stainless steel molds, and pressed into shape at loads up to 150 MPa and temperatures near 750°C. MgF_2 missile domes typically have a translucent milky appearance due to birefringence-induced scattering ($\Delta n \approx 0.012$) and some remaining porosity. *Momentive Performance Materials* has worked on cubic Tl:NaI ceramics, which have been processed at temperatures of 580°C and pressures between 207 and 1400 MPa [74]. As expected, transparency in the visible for cubic polycrystalline NaI is much improved over that of MgF_2 (tetragonal) and BaFCl (orthorhombic) ceramics. In the same vein, several groups investigated the use of hot-pressing for the preparation of birefringent halide scintillator materials, including $LaBr_3$ [36,66] and SrI_2 [37]. In the latter case, highly translucent samples (Figure 8) exhibited light yields above 20,000 ph/MeV (i.e. one fifth of that of single-crystal counterparts), mainly limited by absorption.

Figure 8 Transparent SrI2 ceramic produced by hot-pressing [37]. Picture provided courtesy for Prof. Romain Gaume

1.3.4 Background on Sintering

Depending on the temperature and pressure conditions of hot-pressing, the densification of a powder compact proceeds either through diffusion or plastic deformation:

- ***Hot-pressing by diffusional flow:*** The work of Coble explains that a flux of ions in the direction required to relieve stress may occur under the application of an external pressure [75]. This phenomenon is known as creep and is analogous to the sintering of powders under pressure. In a ceramic powder compact, an externally applied pressure is related to the true stress at particle interfaces by a stress intensification factor (Φ). As explained in [76]. The stress intensification factor is approximated by 1/ρ, where ρ is relative density, when the density is above 90% of the theoretical. Typically this pressure driving force outweighs the surface energy driving force. The pressure is effective in driving the diffusion of atoms from the particle interface (grain boundary) or bulk of the particle to the pore surface. This diffusive process can occur through the grain boundary (Coble creep, equation 1.2), or through the crystalline lattice (Nabarro-Herring creep, equation 1.3). The creep expressions in terms of the measurable quantity, strain rate, are derived in [76] and take the following form:

$$\varepsilon' = A_1 \frac{D_1 \Omega}{G^2 kT}\left(\phi p + \frac{2\gamma_s}{r}\right) \tag{1.2}$$

$$\varepsilon' = A_2 \frac{D_1 \delta_{gb} \Omega}{G^3 kT}\left(\phi p + \frac{2\gamma_s}{r}\right) \tag{1.3}$$

The two are distinguished by their grain size dependence, i.e. the total grain boundary volume vs. total grain volume in the material. Ω is the atomic volume, D is diffusivity, G is grain or particle size, γ_s is surface energy, δ_{gb} is the width of the grain boundary, and k is Boltzman's constant.

- ***Hot-pressing by plastic deformation:*** In the case of MgF_2 densification, where pressures of hundreds of MPa are used, a different mechanism of densification is expected. This mechanism is related to dislocation motion. Unlike the diffusion process, dislocation motion can also occur at low temperatures, hence the lower temperatures relative to the melting point in MgF_2 processing versus SrI_2 processing. The glide of dislocations during this so-called plastic deformation is controlled by the dislocation density, Burgers' vector, and the velocity of dislocation motion. The velocity is determined by the number and energy of obstacles, kinks for example. Again, this mechanism can be expressed in terms of the strain rate of the material as derived in [77] and shown in equation 1.4. μ is the shear modulus, β is a constant, b is the Burgers' vector, ν is a frequency of obstacles, ΔF is the activation energy required to overcome an obstacle, and τ is the stress to overcome an obstacle. This could be the Peierls resistance to lattice motion or a stress due to impurities. Typically, for plastic deformation to proceed homogeneously, 5 independent slip systems are required (Von Mises criterion). Due to their higher symmetry, cubic materials have more available independent slip systems (six primary in the fluorite structure), so they should be more easily deformable by plastic sintering than non-cubic materials such as MgF_2 or $BaCl_2$. However, increased temperature can increase the number of active slip planes. Also very high pressure can cause slip along planes, where slip wouldn't usually occur. Finally, limited movement of planes can occur along twin boundaries. These last three points are important to show that the conditions of plastic deformation for non-cubic $BaCl_2$ are likely more extreme in both temperature and pressure than those required for cubic materials.

$$\varepsilon' = \frac{\alpha}{b}\left(\frac{(\phi p)^2}{\mu}\right)^2 \beta b v exp\left[-\frac{\Delta F}{kT}\left(1-\frac{\phi p}{\tau}\right)\right] \quad (1.4)$$

Still another mechanism may come into play at higher temperatures, where the dislocation can climb by a diffusion-limited process to overcome an obstacle, rather than requiring a specific force to bypass the obstacle. Thus, the strain rate for high temperature glide plus climb is increased with respect to glide alone as seen from equation 1.5. A general rule of thumb from experimental observations of dislocation motion is a stress exponent ≥ 3, thus the exponent in equation 7 is not rigorously defined.

$$\varepsilon' = A_1 \frac{D_v \mu b}{kT}\left(\frac{\phi p}{\mu}\right)^3 \quad (1.5)$$

For halides sintered at relatively high pressures, both creep and dislocation glide appear to be reasonable mechanisms. Pressure sintering studies of CsI by Kim (34 MPa and 100 ^{o}C) [78], have shown experimental agreement with the dislocation glide theory presented above. Sintering studies of non-cubic halides under pressure and lower temperatures are not documented in the literature, however the yield strength of these materials is generally much higher than that of alkali halides. Again, lower temperatures are preferred in order to limit volatilization and the creation of point defects. Thus, the ideal pressing conditions for densification of $BaCl_2$ near room temperature by plastic flow are expected to fall somewhere in between the 34 MPa and 100^{o}C of CsI and the pressures >1 GPa for soft metals and oxide ceramics. These pressures are not experimentally feasible, so slightly higher temperatures should allow for slightly lower pressures to be used as in the case of MgF_2.

- **Pressureless Sintering:** Powder compacts can also sinter in the absence of pressure as explained using a simple expression of surface energy at the interface between two spherical

particles. Here the total surface energy of the system has a contribution from the curved spherical surface, whose energy and area are given by γ_s and A_s, and a new interface or neck between the particles, whose energy and area are given by γ_{ss} and A_{ss}.

$$\partial G_{sys} = \partial \int \gamma_s dA_s + \partial \int \gamma_{ss} dA_{ss} \quad (1.6)$$

Equation 1.6 shows that the driving force for pressureless densification is increased with higher surface curvature, i.e. smaller particle sizes. We already know that small particle size is a requirement to limit birefringence, so it is interesting to discuss whether small particle size can also help drive densification. In addition to lattice and grain boundary diffusion, other transport pathways are also possible during pressureless sintering.

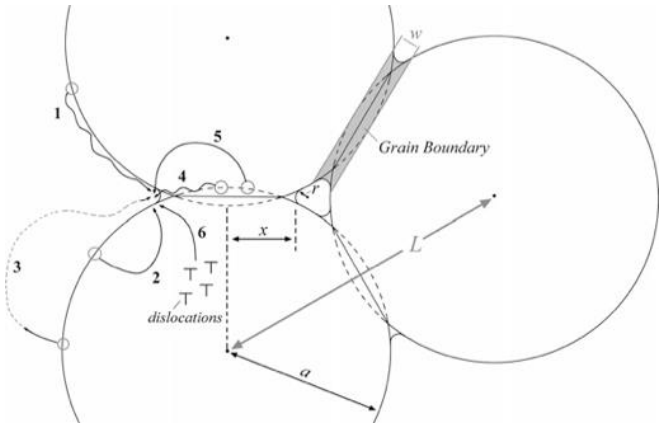

Figure 9 A schematic representation of the different modes of diffusion acitive in a powders compact at eleveted temperature

Referring to Figure 9, matter can also be transported by vapor phase from a particle surface to the pore surface (3), surface diffusion from a particle surface to the pore surface (1), and lattice diffusion from a particle surface to the pore surface (2). However, in contrast to lattice to pore surface diffusion, these mechanisms do not lead to densification and participate to grain growth, hence decreasing the driving force for densification. Because the hot-pressing

methods discussed above greatly increase densification rates, the effects of the non-densifying mechanisms can be minimal. However, in pressureless sintering all active mechanisms are competing. This is especially problematic for halides, because high volatility can lead to the dominance of vapor transport mechanisms. Goodall found good agreement with diffusional transport theories in the study of pressureless sintering of NaCl between 500 and 800ºC at varying particle sizes [79]. Not surprisingly, due to vapor transport, the highest relative density achieved is below 0.9, which is in no way suitable for optical ceramics. However, pressureless sintering does work for halides in some rare cases, as described in a recent publication by M. Mortier. CaF_2 laser ceramics derived from nanopowders (<50 nm) show high transparency after pressureless sintering at ~0.5 T_m for 1 h and without the need for a secondary hot isostatic pressing step [25]. Small grain size is likely a reason for increased densification in this case. Furthermore, vacuum sintering is also used in the field of transparent ceramics (mostly for oxides) to decrease the counteractive pressure of gas inside pores. Gas filled pores are especially problematic when porosity is closed and the densification can be halted when the pressure of gas inside the pore is enough to offset the driving force for pore closure. Although it has worked in limited cases, pressureless sintering of halides is generally not recommended due to high volatility and dominance of vapor transport and grain growth.

1.4 A new approach to the sintering of $BaCl_2$

In cubic phase $BaCl_2$ (fluorite structure), there are six available primary slip systems {100} <110> and hence a greater likelihood of densifying $BaCl_2$ at a given temperature and pressure than in the orthorhombic phase. We could prepare cubic $BaCl_2$ powders by rapidly quenching from the

high temperature cubic region of the phase diagram in the spirit of the work by Edgar. Quenching pure cubic $BaCl_2$ is a challenge on its own but preserving the cubic phase on reheating to the hot-pressing temperature would be an additional challenge. Another option is to utilize the state-of-stress during the pressing operation to upset the phase equilibrium and stabilize the cubic phase. In 1970, Coe reported that the so-called "thermodynamic effect of shear stress" causes a significant shift in the orthorhombic-to-monoclinic transformation of mineral enstatite $MgSiO_3$ such that the slope of the temperature phase diagram ($dT/d\tau$) is found to be near $3^oC/MPa$ [80,81]. By these numbers, a moderate applied load of 100 MPa is expected to shift the transition temperature by 300^oC. In metallurgy, work on transformation induced plasticity (TRIP) steels and shape memory alloys have done a lot to strengthen the theory behind stress-induced structural transformations in polycrystalline materials. So called martensitic transformations in non-metallic, synthetic ceramics are less prevalent than for minerals and metals, and the most notable remains that of stress-activated tetragonal-to-monoclinic transition in zirconia (ZrO_2) to increase toughness [82,83]. Furthermore, a disordered hexagonal-to-wurtzite phase transition in a rotational diamond anvil cell has been shown to occur at pressures 45 GPa lower than previously reported under hydrostatic conditions [84].

On the basis of prior DFT-modeling of cotunnite-to-fluorite transition in CaF_2 [85], an isomorph of $BaCl_2$, we can hypothesize that the transition temperature of the orthorhombic-to-cubic phase transition in $BaCl_2$ can be lowered by the application of a shear stress. To our knowledge, the stabilization of the cubic phase under shear stress has never been reported. The only reported high pressure phases of $BaCl_2$ take on a hexagonal or monoclinic structure [86,87]. These phases are observed by in-situ x-ray diffraction while loading to above 6 GPa in a diamond anvil cell, a mostly isostatic loading condition. Thus, the prospect of a shear-induced, moderate-

pressure transition in still unexplored. As a first order estimate of the stress required to bring the transition temperature down to 400°C (i.e. about 500°C below the normal transition temperature of 925°C at 1 atm), one can use an analog of the Clausius-Clapeyron equation for shear stress condition [88]:

$$\Delta T = \frac{\gamma_{\alpha\beta}}{S_{\alpha\beta}}\,\tau \tag{1.7}$$

where $S_{\alpha\beta}$ stands for the variation in entropy at the phase transition, $\gamma_{\alpha\beta}$ the value of the transformation shear strain and τ the resolved external shear. With the transformation strain $\Delta b/b$=1-0.65 (ICDD references) and temperature shift ΔT=500°C, an entropy variation $\Delta s_{\alpha\beta}$=14 J/mol/K [89], and a molar volume $v_o=55\text{x}10^{-6}$ m^3/mol, one finds τ=45 MPa. This is a very reasonable pressure for a laboratory hot-press, however the Clausius-Clapeyron relationship applies to the resolved shear stress in a single-crystal. In reality, powder compacts of randomly oriented $BaCl_2$ grains would transform at a higher nominal pressure. We have no reliable way to estimate this pressure more precisely than this lower bound, but assume that a laboratory hot-press might reasonably achieve it.

1.5 Objective of this work and outline of the manuscript

If achievable, this 'phase-change' sintering concept, whereby a ceramic could be densified at a lower temperature than with traditional methods, would be an exciting new pathway. Naturally, potential issues pertaining to the homogeneity of stress during the process, and possible phase-reversion upon pressure-release on the transparency of the sample will need to be investigated. Additionally, the presence of extended defects resulting from the deformation of the material may alter the scintillation properties and some additional post-treatment are envisioned. Our work addresses some of these questions and the present thesis is structured as follows:

In Chapter 2, we review our initial attempts at demonstrating the densification of $BaCl_2$ ceramics by the 'phase-change sintering' technique using standard hot-pressing equipment. While these experiments were mostly inconclusive, they nonetheless helped us narrow down the sintering schedule for this material, and provided 'baseline' reference ceramic materials for traditional hot-pressing. They were also essential in helping us design an improved and unique hot-pressing equipment for our following investigations. The design criteria, capabilities and performance of that device are addressed in the remaining part of that chapter.

Chapter 3 presents our results regarding the preparation and characterization of undoped and europium-doped starting $BaCl_2$ powders by the spray-drying technique. For transparent ceramic fabrication, powders have to present specific requirements such as being free-flowing, small (usually under 1 µm) and of narrow size distribution to allow the arrangement during the initial stages of compaction. Beginning with small particle size allows for better control of the grain size, however fine powders are more susceptible to Van der Waals interactions between particles leading to poor flowability [90,91]. To preserve small crystallite size while increasing dry-flowability, spherical and dense agglomerates, we chose to investigate the technique of spray-drying, a method often applied to oxide ceramics, which had not been evaluated before for halide compounds such as $BaCl_2$.

In Chapter 4, we review our phase-change sintering experiments and modeling.

And finally, Chapter 5 summarizes the optical and scintillation performance of the materials produced in this work, before opening a few perspectives on future endeavors in the conclusion.

2. HOT-PRESSING OF $BaCl_2$

2.1 Graphite die hot-pressing

The baseline pressing experiments to compare to the previous studies of $LaBr_3$ and SrI_2 are completed in a commercial hot-pressing system (Thermal Technologies). $BaCl_2$ is less hygroscopic than the bromide and iodide compounds listed, so on this basis it should have a higher probability of success when exposure of powders to the ambient atmosphere is difficult to avoid.

2.1.1 Experimental details

High purity anhydrous beads of $BaCl_2$ (Sigma Aldrich 99.999%) were gently ground inside a glovebox using an alumina mortar and pestle to achieve an average particle size of 50 μm. Powders were held inside a 1" diameter floating graphite die. The "floating" design allows free movement of both upper and lower pistons and better compaction homogeneity.

Figure 10 Hot-press (Thermal Technologies, Inc.) used for initial sintering experiments.

Graphite foil lining material was used to prevent possible sticking between the sample and the die. The die was loaded with 5 g of powder inside the glovebox and transferred quickly to the hot-press. The hot-press was evacuated to 10^{-3} torr and purged with argon three times, before maintaining under a constant flow of argon. Samples were pressed at temperatures between 600 and 900^{o}C. The pressure was increased to 45 MPa once the sintering temperature was reached and the pressure was not released until after the sample had cooled back down to room temperature. After pressing, the densification curves were analyzed according to the strain rate equations presented in Chapter 1. Sample microstructures were analyzed using a Zeiss Ultra 55 scanning electron microscope (SEM) equipped with a Thermo Fisher Noran System 7 energy dispersive x-ray spectrometer (EDX) for elemental analysis. Crystalline phase was analysed with a Bragg-Brentano geometry Rigaku d/max x-ray diffractometer utilizing Cu-K_{α} radiation. Structure was also analyzed using Bruker Senterra micro-Raman spectroscopy setup with a 785 nm excitation source. A 5x objective corresponding to a spot size of ~12 μm is used.

2.1.2 Results

After testing sintering temperatures between 600 and 900^{o}C, the minimum temperature leading to full densification was found to be 850^{o}C. A 4 h soak at this temperature was sufficient to achieve sample densities in excess to 99%.

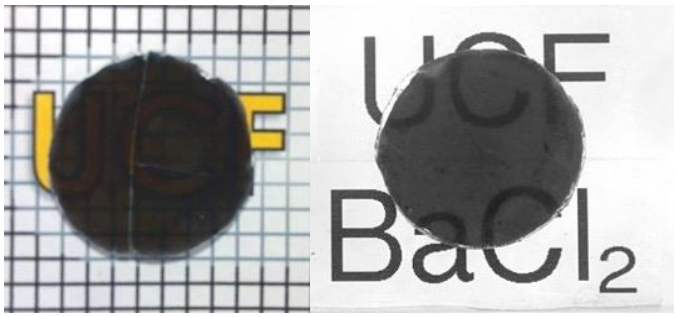

Figure 11 BaCl2 ceramic samples hot-pressed at 850oC and 47 MPa a) only illuminated from the front and b) backlit to clearly show inclusions

Samples pressed under these conditions appear dark and have visible inclusions seen in the backlit image in Figure 11b. Using micro-raman spectroscopy, we have been able to collect structural information on these inclusions. Figure 12 shows the Raman spectra of an inclusion compared to that of the bulk ceramic.

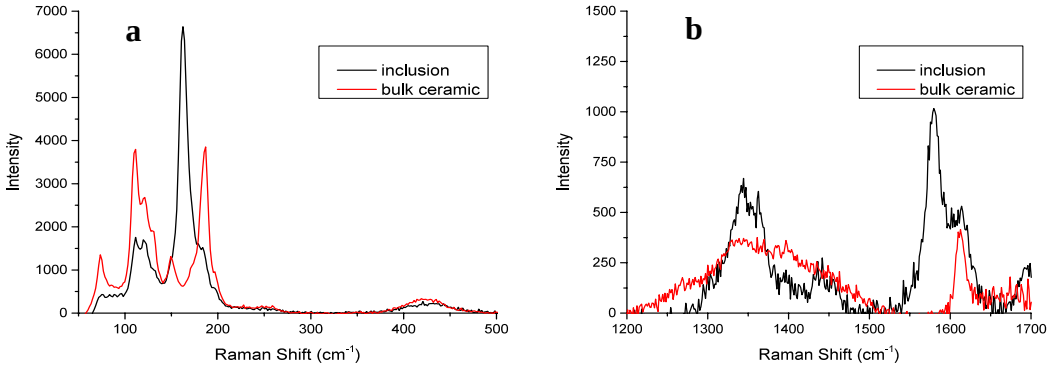

Figure 12 Raman spectra of the bulk ceramic and an inclusion given in both the a) low and b) high frequency windows.

The spectra from the inclusion in the window 1300 cm^{-1} to 1700 cm^{-1} shows the major peaks attributed to carbon at 1355 and 1575 cm^{-1} [92]. There is an additional peak from the inclusion in the low frequency window at 162 cm^{-1}. The bulk sample shows all peaks expected from $BaCl_2$ in

the low frequency range [93] and one unexplained feature centered at 430 cm^{-1}. In the higher frequency range, the bulk shows a broad feature centered at 1350 cm^{-1} and a narrower feature at 1610 cm^{-1}, both possibly arising from the hydration of the surface of the sample [94].

The temperature, pressure, and displacement curves recorded during a typical run are shown in Figure 13. A protocol was developed to further analyze the displacement curves in the context of sintering mechanism (diffusional flow vs plastic deformation). These results, although incluclusive, are covered in Appendix 1. During the temperature increase, the relative density begins to increase rapidly at a temperature near 400°C. This could be the indication of creep, or the indication that plastic deformation is initiated at this temperature.

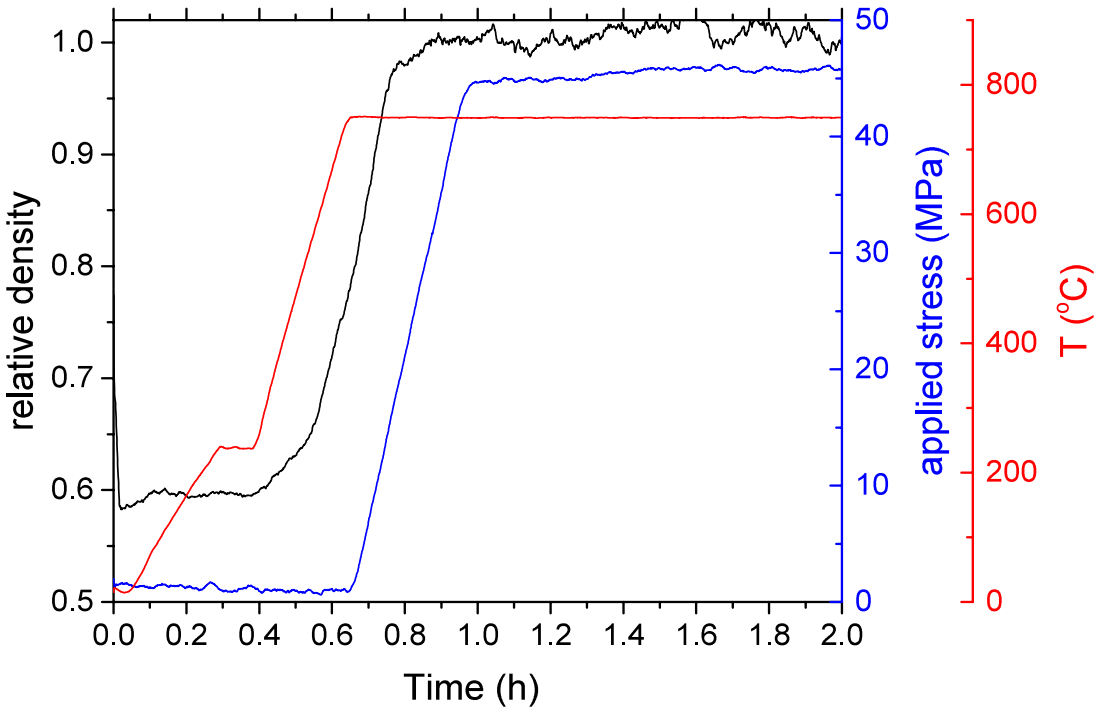

Figure 13 Relative density, temperature, and stress curves for a typical $BaCl_2$ hot-pressing experiment

Once the dwell temperature is reached, the application of the 45 MPa load further increases the density of the ceramic.

The fracture surface of a hot-pressed sample is shown in the SEM micrograph of Figure 14 and the grain size is calculated to be above 5μm on average. This is smaller than the beginning particle size (), so significant fragmentation and/or recrystallization of particles must have taken place. Fracture appears to be largely intra-granular due to the lack of angular protrusions in most areas of the image. No significant porosity is noted in the micrographs, suggesting near theoretical density.

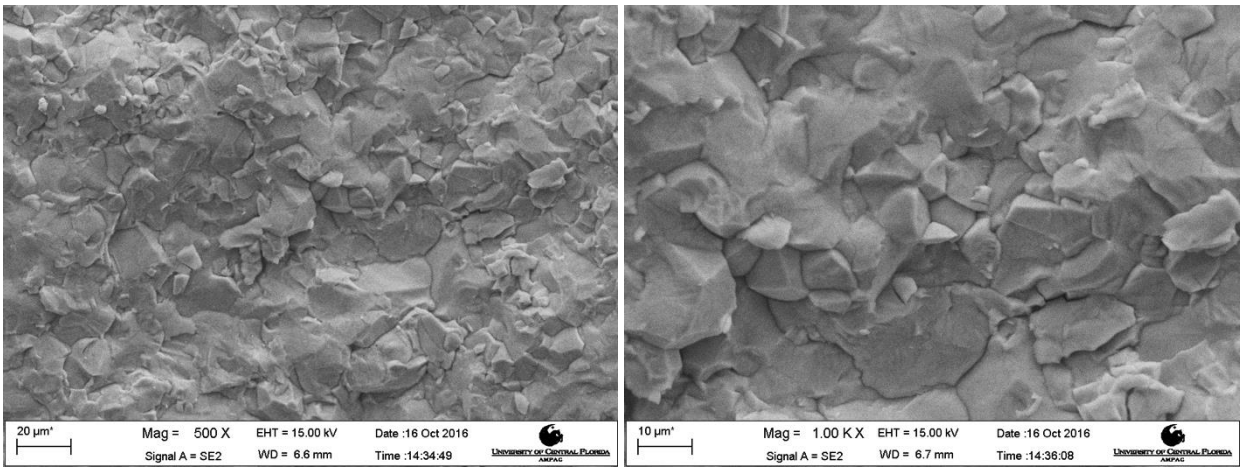

Figure 14 SEM micrographs of a fracture surface in a $BaCl_2$ sample hot-pressed at a temperature of 850°C and pressure of 47 MPa for 4 hours at magnifications of 500x and 1000x.

The final sample fabricated this by method showed some very surprising results. The sample was first part of a baseline presureless sintering run at 750°C for 2 h, followed by a hot pressing run at 750°C for 10 h. The sample is less darkly colored than the many samples that came before it, and the edges are highly translucent as seen in Figure 15.

Figure 15 Sample prepared by cold-pressing, conventional sintering at 750ºC, followed by a hot-forging operation at 750ºC.

Examining the sintering curve for this sample in Figure 16, we can see that not only the radial constraint, but the sintering schedule is different compared to the sample presented above.

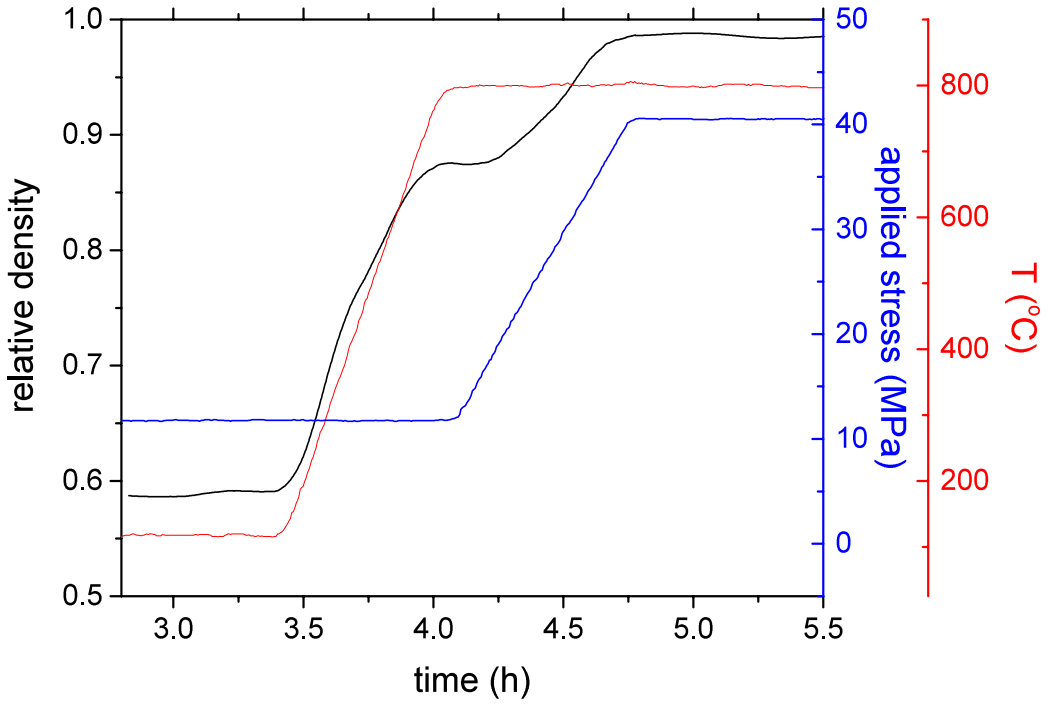

Figure 16 Sintering schedule and densification curve for the sample pictured in Figure 13.

The load is applied at the temperature of 300ºC and significant density is gained at this temperature. The densification is finalized when the temperature is increased to 750ºC. Although this sample could not be replicated, it is the first glimpse at how shear deformation (radial spreading) at low temperatures is effective in producing transparent ceramics of $BaCl_2$.

2.1.3 Discussion

Overall, sintering $BaCl_2$ powders in a commercial hot-pressing system does not produce the sample transparency required for the scintillation application. Samples have carbon inclusions from the graphite pressing dies. The bulk volume of the samples is also darkly colored. The grain size is large, such that the birefringence of the material is a major limitation to high transparency even if issues of sample coloration leading to absorption are solved. During this thesis work, there was not sufficient time to explore the origins of sample coloration. Studies found in the literature suggests that coloration can come from vacancy centers and contamination from impurities such as oxygen, however defect studies must conducted to confirm this [57,95]. The spectroscopy results in Chapter 5, show some examples of how we can probe these optical defects.

In these initial hot-pressing studies, full density is obtained at the pressure limitation of 50 MPa and temperatures between 750-850ºC. This temperature is such that the controlling mechanism to densification occurs very rapidly by either plastic deformation or diffusional creep. Phase analysis by XRD confirms samples are purely orthorhombic after hot pressing, however nothing can be said about the phase during the hot pressing operation. Finally, a lone sample exhibiting high transparency only on the edges was produced. This has been interpreted as an effect of inhomogeneity in the stress field (significant shear component) leading to an increased plastic deformation along the edge. After several unsuccessful attempts to replicate this sample,

it was decided higher pressures and lower temperatures would be required to ensure this densification occurs by the plastic shearing required by the phase change sintering hypothesis. Likewise, the transparency will not improve unless carbon contamination and the effects of atmospheric impurities are also controlled.

2.2 Design of an atmosphere-controlled hot-press

To minimize or prevent powder contamination during the loading and transfer of the die to the hot-press, some approaches include the miniaturization of a hot-presses for use inside a standard glovebox [96] or building a large air-tight enclosures around industrial-sized spark plasma sintering systems [97] such that it can be connected directly to the glovebox. Here, we attempt to take a more practical approach towards a low-cost, compact and elastic pressing chamber, which can be loaded and sealed inside a glovebox and transferred to a floor-standing external hydraulic press with 12 US ton capacity, translating to over 200 MPa acting on a 1" die. The modular design of the chamber can accommodate a heater and function as an airtight hot-press for the consolidation of a wide range of materials, most importantly the scintillator ceramics of interest in this thesis, under vacuum or inert atmosphere. As we will see, this concept solves the issue of sample contamination by ambient air.

2.2.1 Physical description

The setup consists of a double-ended floating die assembly placed inside a flexible airtight container (Figure 17). The container is made of a standard iso-160 stainless steel vacuum bellows (Kurt J. Lesker Company), measuring 150 mm internal diameter by 150 mm tall. The bellows is hermetically clamped to a stainless steel base and an iso-160 lid using two sets of silicone O-rings and twelve aluminum claw clamps. Inside the chamber, the compaction die is surrounded by a

1.4 kW 100 mm-diameter cylindrical resistive heater (Hyndman Industrial Products) and by a 25 mm-thick layer of quartz wool to provide thermal insulation. The base is drilled out to allow the installation of an electrical feedthrough for powering the heater. Additional holes and feedthroughs allow for connections to a vacuum/purge port and to a type K thermocouple for monitoring the die temperature. The entire assembly weighs about 25 kg and can be easily positioned on a 20-ton shop press (Figure 18a). This compact assembly fits the antechamber of most commercial gloveboxes (Figure 18b). This is a key feature of the present design, which enables keeping the raw powders, loaded in the die, and the final pellet obtained after pressing away from any atmospheric contamination during the entirety of the compaction process.

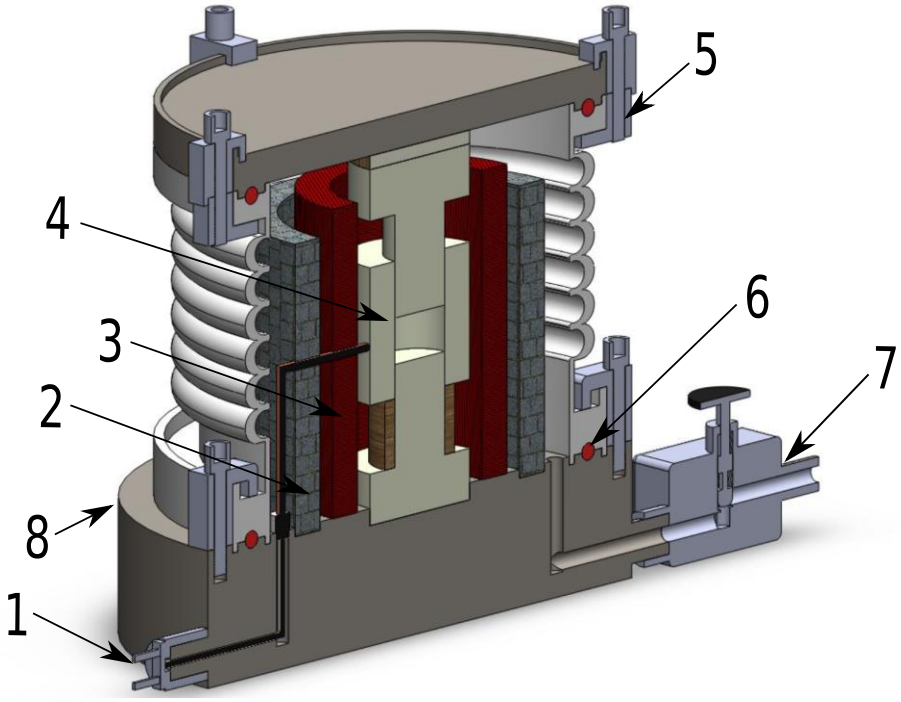

Figure 17 Schematic view of the flexible chamber showing 1) thermocouple feedthrough, 2) quartz wool insulation, 3) heater, 4) die assembly, 5) claw clamp, 6) silicon O-ring, 7) vacuum/purge port, and 8) power feedthrough (hidden).

When used as a hot-press, the heater is connected to an external power unit equipped with a temperature controller (Eurotherm). For powder compaction and sintering studies, a linear variable differential transformer (LVDT) is mounted on the outside of the chamber, between the base plate and the lid, to monitor sample displacement, while an electronic pressure gauge is installed on the hydraulic line actuating the press. Additional sensors such as oxygen, moisture or residual gas analyzers can easily be mounted on the chamber. The output of these sensors can be then simultaneously recorded using a data acquisition device. An example of a sintering curve is found in Figure 19.

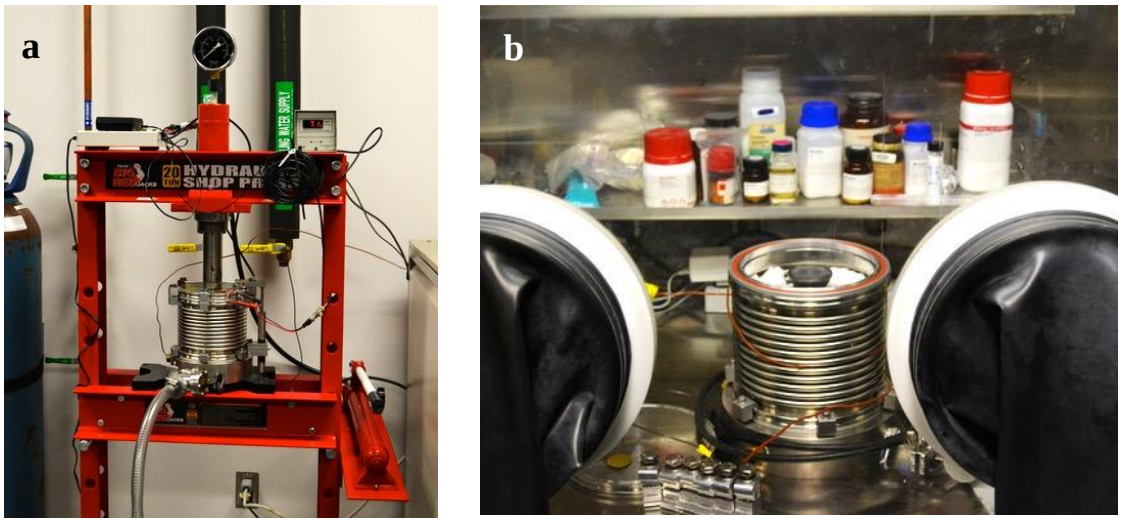

Figure 18 (a) The pressing chamber mounted to a hydraulic pressing frame. (b) Inside view of the pressing chamber as it sits inside the glovebox during loading/unloading with the top lid removed. The top plunger of the die assembly and the quartz wool insulation are visible in the center of the canister.

The limited machining of the base and the use of off-the-shelf components make the present design low-cost and easy to assemble. Furthermore, the limited use of fibrous insulation and dust-generating graphite dies provide less opportunity for particulate contamination than many

commercial systems. A comparison of the key properties of our device with those of widely used commercial hot-press and spark-plasma sintering (SPS) systems is highlighted in Table 2. The temperature, pressure, and atmospheric capabilities are largely dictated by material selection and, to a lesser extent, by the design of the press. These aspects are discussed in the section below.

Table 2 Selected properties of major pressure-assisted sintering technologies.

	This press	*Hot-press*	*SPS*
Cost (k$)	1	250	500
System height (m)	0.3	3	3
Temperature (^{o}C)	1000	2000	2500
Pressure (MPa)	400	400	100*
Heating rate (^{o}C/min)	10	10	1000
Cleanliness	++++	++	+

*** SPS is limited to graphite tooling, while this press and conventional hot-presses can employ high-strength steels, refractory metals or carbides.**

2.2.2 Pressure capability

The maximum pressure rating of the chamber is determined by the strength of the die-set material and by the footprint of the plungers at the base plate and top lid, so as to prevent permanent deformation by yielding. Die-sets are made of stiff and strong materials including graphite, high-strength steels, molybdenum or tungsten carbide, whose properties as they relate to pressing dies are discussed at length elsewhere [98–100]. With compressive strength on the order of 100 MPa, high-density fine grain graphite is most commonly used in high-temperature hot-presses. It is however brittle and its purity and reducing behavior at high temperature can lead to sample contamination issues [101,102]. With average room temperature compressive strengths of 400 MPa, high-strength steels and molybdenum are well suited to drive performance to higher pressures, but the significant temperature dependency of their behavior must be taken into account

in the design. Cemented tungsten carbide die assemblies on the other hand, allow extending applicable pressures towards the gigapascal range.

2.2.3 Temperature capability

Throughout the design, thermal modeling (Energy2D software [103]) was used to test possible implementations of the press and their effect on (i) the maximum achievable temperature at the sample location, (ii) the temperature profile across the sample, and (iii) the maximum achievable heating and cooling rates, as these characteristics affect the sintering behavior of materials. To this end, a 2-dimensional cross-section of the setup was drafted and the appropriate thermal properties of each component were defined. The heating element was treated as a source of constant heat flux and conductive and convective heat transfer were monitored over time. In this compact system, the maximum temperature achievable at the sample location is largely determined by the power of the heating element and the maximum temperature that the O-rings can withstand (200^{o}C). Simulations also found that adding an alumina ceramic spacer between the plungers and the base or top flange limit heat flux loss by up to 32% for a 14 mm spacer thickness. Consequently, the maximum average heating rate between 25 and 600^{o}C is expected to increase by 7% and 10% for a 7 mm and 14 mm spacer, respectively.

In testing, the die temperature was raised to 600^{o}C. After a 1-hour dwell at this temperature, the top flange, just above the O-ring, reached 85^{o}C and 100^{o}C after 2 h. This is in reasonable agreement with our simulation, which indicates that the O-ring reaches 84^{o}C and 147^{o}C after one and two hours, respectively. Safe and prolonged use of the press at temperatures well beyond 600^{o}C should pose no issue, however active air or water-cooling of the bellows and top flange would be required. In addition, our simulation indicates that, after 1 hour equilibration, radial

temperature gradients at the sample location are minimal and range from 0.1 to 0.3°C/mm in the case of graphite and high-strength steel dies, respectively. During pressing runs, typical heating rates are 8°C/min with the heater operated at 55% of its capacity (Figure 19). Simulations indicate that the maximum heating and cooling rates can reach 15°C/min.

2.2.4 Sample preparation procedure

The pressing chamber is loaded in the glovebox as shown in Figure 18. A typical procedure consists of loading the press with a 13 mm-diameter, 6 mm-thick powder-compact made with a separate arbor press located inside the glovebox. These consolidated pellets are embedded in a soft pressure-transmitting medium, such as anhydrous sodium chloride. Anti-adhesive gaskets (e.g. graphite) or coatings (e.g. boron nitride spray) are used on the plungers to prevent the sample from sticking or cracking due to friction during extraction. Once loaded, the top plunger is placed into the die and the top flange is clamped down to seal the chamber. A 1-mm deep recess machined in the base prevents the die from shifting during transport. The hermetically sealed chamber is then transferred through the antechamber of the glovebox and mounted on the hydraulic press frame. The electrical and ground wiring are connected as well as the sensors, vacuum and inert-gas lines. After compaction, the chamber is transferred back into the glove box for unloading.

2.2.5 Experimental tests of the atmosphere controlled press

A few brief experiments were devised to test the functionality of the press. For these experiments, the temperature was ramped at 450°C/h to a temperature of 450°C, a temperature where deformation begins in the hot-pressing experiments conducted in the commercial hot-press.

After a short dwell of 15 min, a load of 400 MPa was applied [3] in a stepwise manner to achieve a pressure ramp rate of 200 MPa/h. The press was cooled naturally at an initial rate near 500°C/h.

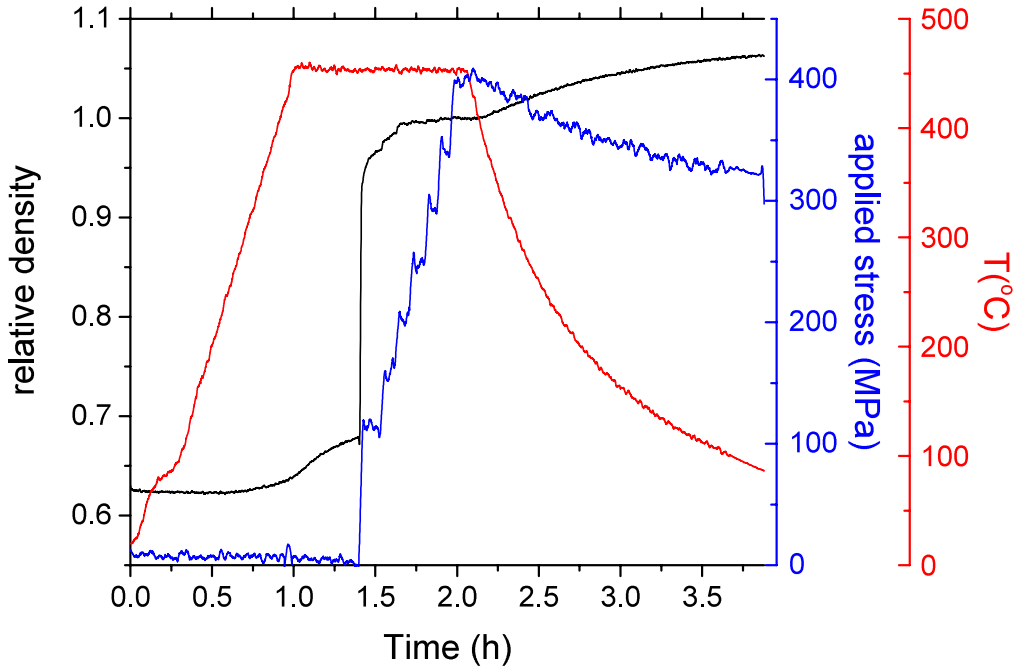

Figure 19 Example of a sintering curve obtained with the newly designed hot-pressing system.

In optimization tests, NaCl was picked as a pressure transmitting medium because it is commonly used in the high-pressure mineralogy field (diamond anvil cells).

[3] This is the hydraulic pressure over the 13 mm face of the $BaCl_2$ pellet. The nominal pressure experienced at the 25 mm die face is about one fourth of this value. The NaCl pressure transmitting medium will certainly have an effect on the state of stress, but it cannot be accurately calculated or measured at this time.

2.2.6 Results and Discussion

Examples of highly transparent samples produced in the custom-designed press are shown in Figure 20. Qualitatively, it was found that the transparency of pure barium chloride samples did not depend on whether the press was loaded inside the glovebox or not. It is important to note that the moisture absorption rate of $BaCl_2$ is much lower than other promising halide scintillators ($LaBr_3$, SrI_2), so perhaps the extreme measures for handling these hygroscopic raw materials are not necessary for pure $BaCl_2$. In later-stage experiments on europium-doped $BaCl_2$ (covered in Chapter 5), it is clear that the powder loaded inside the glovebox produces better scintillation performance than if loaded outside in the ambient air. Thus, the new press design is critical for the Eu:$BaCl_2$ scintillator application.

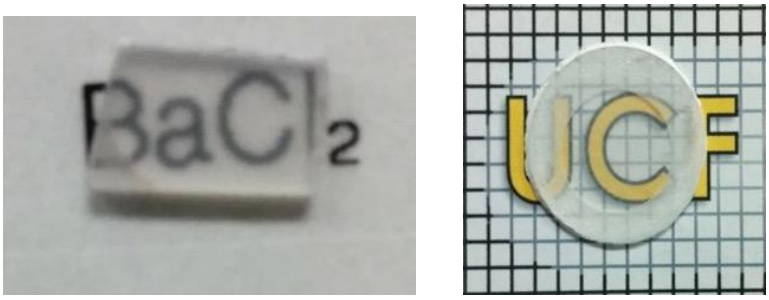

Figure 20 Pictures of pure $BaCl_2$ ceramics hot-pressed at 450°C and a nominal pressure of 120MPa. The left image shows a piece salvaged from a broken sample in an early experiment while the right sample shows a full sample with the NaCl pressure transmitting medium around the outside.

By examination of the densification curves, the sintering mechanism appears to be different than that identified for the high temperature hot-pressing. The density increases very rapidly at first, then slowly (due to a slow pressure ramp rate) reaches a maximum near 100 MPa of nominal applied pressure. Relation of sintering curves to a sintering mechanism is difficult given the manual rate control and the relatively few number of points collected during each pressure ramp

step. Appendix A covers the protocol in development for analysis of sintering in the newly designed press.

2.3 Conclusion

Sintering of $BaCl_2$ to high density is possible at both high (850°C) and low (450°C) temperatures. Samples pressed in a commercial hot press with carbon dies suffered from low transparency and strong dark coloration. A single ceramic sample showed a highly transparent edge after a forging operation in this commercial hot press, providing hope that the shear induced sintering mechanism outlined in Chapter 1 could be a reality. A new press was designed and built for low-temperature and higher pressure (with shear component) densification studies in accordance with the goal of achieving phase change sintering. This device proved useful in the production of high-transparency, colorless pure $BaCl_2$ samples with no carbon contamination. As discussed later in Chapter 5, this design was also critical in limiting the oxygen contamination of europium (2+) doped samples. Results are very promising even before any optimization of powder morphology. As the powder morphology and the uniform incorporation of the dopant ion are critical steps in the sintering process, the next chapter focuses on powder processing.

3. PREPARATION OF $BaCl_2$ POWDERS

The results of hot-pressing experiments in the atmosphere-controlled press utilizing high-purity commercial powders are very promising, however the picture of the 2 mm-thick sample in Figure 20 clearly show cloudiness likely originating from scattering. Regardless of the source of this scattering, tailoring the powder morphology for the sintering process can help reduce both grain size and pore population. For a temperature activated diffusion process, a smaller crystallite size in the precursor powder typically results in a smaller grain size after sintering. In this case, smaller particles with higher curvature enhance the mass transport at particle interfaces and also lead to a higher density at a given sintering temperature. However, in phase change sintering technique proposed in this thesis, powder morphology (i.e. particle shape and crystallite size) may play a different role. Considering the Hall-Petch inverse relationship between grain size and mechanical strength, smaller particles will have a higher strength and require higher pressures to deform. Furthermore any residual strain in mechanically milled particles may also limit the ability to deform particles in a plastic sintering process.

Powder size aside, another important aspect of powder processing is to uniformly incorporate europium into the $BaCl_2$ lattice, which is important for an optimal energy transfer in the scintillation process. This cannot be done effectively by a solid-state diffusion process at 450^{o}C, where we find promising results in the newly designed hot press. Higher temperatures would be required for $BaCl_2$ and $EuCl_2$ to form a homogeneous solid-solution, Even at high temperature, depending on the segregation coefficients of the species, clustering of dopants is possible. Another route towards dopant incorporation is to crystallize the Eu:$BaCl_2$ solid-solution

from an aqueous solution of Eu^{2+}, Ba^{2+}, and Cl^{-}. This chapter discusses the technique of spray-drying as the preferred route for doping powders and controlling their morphology.

3.1 Spray-dried pure $BaCl_2$ powders

Controlling powder characteristics such as particle size, size distribution, morphology, agglomeration rate, bulk density and moisture content is essential to many aspects of ceramic processing [104]. In particular, spherical particles provide good packing density and lead to higher sintered density [90]. To this end, the technique of spray-drying, which allows the continuous production of dry granulated powders from an aerosol phase, is one of the most widely used techniques in the industry because of its ability to control these characteristics accurately [105,106]. The aerosol is either made of fine droplets of dispersions (slurry) or solutions, which undergo controlled evaporation by contact with a warm carrier gas in a drying chamber. The drying conditions (air flow, temperature, and partial pressure of solvent) as well as the characteristics of the aerosol (droplet size, temperature and the mass fraction of solid or solute) determine the morphology of the particles that are produced. Spray-dried particles are typically spherical and on the order of a few microns in size. It has long been known that elevated drying temperatures, for example, lead to the formation of large particles with low density, while slower drying conditions favor small, compact particles with higher densities. While the ceramic literature abounds with studies devoted to the spray-drying of slurry aerosols such as alumina, yttrium aluminum garnet or zirconia in water and ethanol [107], [108], fewer papers report on the spray-drying of solution aerosols [109], [110]. Because $BaCl_2$ and $EuCl_2$ are highly soluble in water and should produce a homogeneous solid solution at the exit of the spray-drier, pursuing the solution-based route is most interesting for the goals of this thesis. In response to the obvious concerns

about contamination from excess moisture in the powders, we hope to devise a method to heat treat powders either under a flow of inert gas or a reactive gas to remove contaminants.

3.1.1 Theoretical background of spray drying saline solutions

The basic steps of the spray drying process are: (1) the atomization of the feed solution into droplets, usually through a pneumatic nozzle, (2) the mixing of the droplets with the dry air being circulated through the drying chamber, (3) the evaporation of droplets and (4) the separation of the dried powder from the carrier gas. A wide body of work addresses the process of particle formation during spray-drying. These studies mostly report on single droplet drying experiments conducted in controlled environments [111–114], purely theoretical work including mass and heat transfer calculations for droplets [115–117] and a combination of experimental and theoretical work on actual multiple-particle spray dryers [118,119]. Many factors affect the final morphology of the particles, but most published theories focus on the drying mechanism in single droplets under controlled conditions. The following is a summary of the initial stages of drying described by many models and reviewed in the comprehensive article by Mezhericher *et. al* [120]. It only takes milliseconds for the droplet to reach thermal equilibrium with the drying air and begin evaporating at a constant rate. This stage proceeds as long as the surface remains saturated with liquid. If the evaporation proceeds too quickly for the solute to redistribute by diffusion in the liquid droplet, then a solid crust forms. The low permeability of this crust may affect further drying by impeding the evaporation of the solvent trapped in the center. Depending on the nature of the surface layer, several pathways are possible. The temperature of the droplet may increase because of hindered mass transport in the droplet subsurface. This may result in an increase in pressure when the temperature exceeds the boiling point of the solvent. Under these conditions, the shell may either

swell or fracture and a wide variety of particles shapes can be produced through this process. If the crust is porous and allows for the outward percolation of water, then a solid egg-shell can form. It is however possible to obtain dense granules under a particular set of conditions described by Jayanthi *et al*. [121]. This can be understood by considering the slope of the radial concentration profile of the solute in the droplet. Steep concentration profiles at the point of critical supersaturation lead to crust formation before any precipitate forms near the center of the droplet, whereas flatter concentration profiles lead to volume precipitation and dense particles. The development of a specific concentration profile depends heavily on the radial temperature profile as well as on the initial concentration of solute in the droplet. Other factors also affect the formation of irregular particles: if droplets exit the nozzle with a high Reynolds number, their shape oscillates before stable drops are formed. Under high evaporation rate, unstable droplets lead to non-spherical, porous, plate-like or spherulitic aggregates unsuitable for compaction. Similarly, the coalescence of incompletely dried droplets will produce hard agglomerates of smaller aggregates. Some of these aspects are discussed in the experimental work by Lin *et al.* [112] on the influence of processing conditions on the morphology of various water-soluble salts including calcium acetate, sodium chloride, ammonium chloride. These past studies provide a useful basis for the systematic study of the effect of spray drying parameters on the morphology of $BaCl_2$ powders.

3.1.2 Spray drying procedure

$BaCl_2$ can crystallize in the anhydrous, mono-hydrate, or di-hydrate form depending on the partial pressure of water. The transition from one phase to the other is a reversible process [122,123]. Three aqueous solutions of varied $BaCl_2$ concentrations were prepared by dissolving an appropriate mass of barium chloride di-hydrate $BaCl_2 \cdot 2H_2O$ (99.9% purity, Alfa

Aesar) into deionized water. This study focuses only on the 8.66g/100mL concentration as it produced free-flowing spherical powders as well as a wide range of other morphologies if we deviated from ideal processing conditions.

Our experiments were carried out with a tabletop spray-dryer (Büchi B-290), pictured in Figure 22, fitted with the inert loop cooling module (Büchi B-295) set at 17°C. The spray dryer was operated in a closed loop mode, where high purity nitrogen working gas exiting the cyclone was fed into the cooling loop, heated and accelerated back into the drying chamber by the aspirator. To ensure maximum separation rate in the cyclone, the aspirator, which determines the velocity of the gas moving through the system, was set at its maximum capacity (38 m^3/hr).

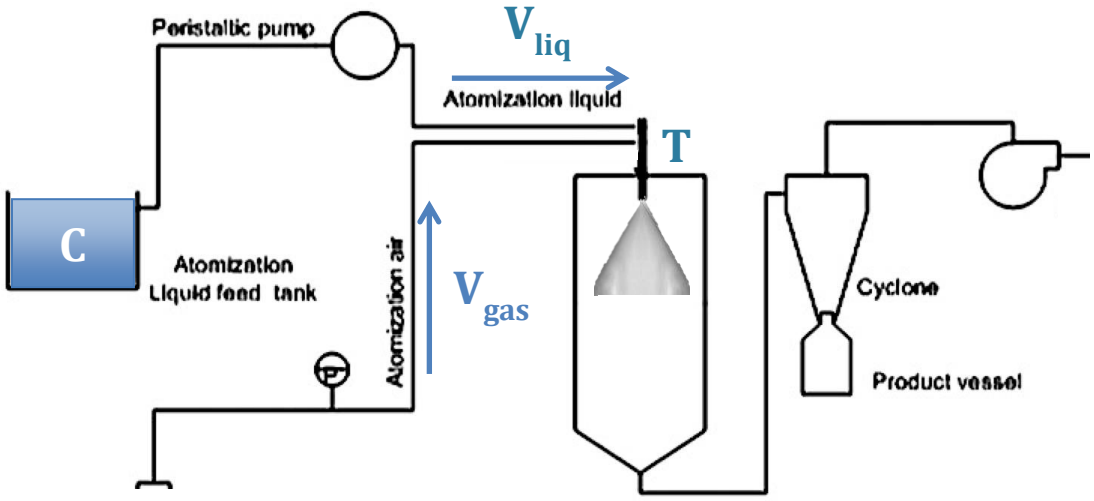

Figure 21 A schematic showing the drying chamber, cyclone and collection vessel component of the spray drier. The blue labels correspond to the varied parameters in Table 3.

Figure 22 Buchi B-290 spray-drier used for the powder preparation experiments.

The spray nozzle has a 0.7-mm opening for the feed solution and a 1.4-mm diameter opening for the gas in the two-fluid geometry. The feed solution of $BaCl_2$ was introduced into the nozzle using a peristaltic pump. Four independent experimental parameters were explored in this study: (1) the solution feed rate, (2) the atomization gas flow and (3) the drying gas inlet temperature (Figure 21). Each of these parameters was varied over a range of values (low, medium and high) as presented in Table 3. A total of 27 separate powder samples, about 2 g each, were produced and subsequently characterized.

Table 3 Range of processing parameters.

Concentration (g/100mL)	Pump rate (mL/min)	Gas flow (L/h)	Temperature (°C)
3.3	12	26	110
10	16.5	52	130
25	21	104	150

The morphology of the powders collected from each experiment was examined by scanning electron microscopy (SEM, Zeiss Ultra-55). The particle size distribution was measured with an acoustic particle size analyzer (AZR-2X, Colloidal Dynamics). For the AZR-2X measurement, powder samples were dispersed into 1,2 dichloroethane using 1% solid loading fraction and dioctyl sodium sulfosuccinate (AOT) as a dispersant. Particle morphology was examined by SEM both before and after preparation of the slurry to confirm that $BaCl_2$ has negligible solubility in dichloroethane. Size distribution was determined by an average of three measurements using the ESA method based on the acoustic absorption of the slurry [124]. The distribution is assumed to be lognormal with the range and center of the distribution being fitting parameters. A statistical analysis of particle sizes in SEM micrographs is used to supplement the particle size data from the AZR-2X. The diameters of 40 particles across 2 SEM micrographs with different magnifications were measured using the ImageJ [125] software measurement tool calibrated to the scale bar produced by Zeiss software. A histogram of particle size versus population was constructed using a bin size of $10^{0.33x}$, where x is an integer, in order to correlate well to the log scale of the AZR-2X. Powder x-ray diffraction (XRD) was performed in the Bragg-Brentano geometry (Rigaku D/Max) using copper-Kα radiation to determine the phase of the powders. Loose powders were pressed lightly into an aluminum sample holder for measurement.

3.1.3 Morphology results

The examination of powder samples by SEM reveals that, compared to the irregular raw commercial powders, the morphology of spray-dried powders fall into five different categories depending on the processing conditions: 1) platelet aggregates, 2) hard agglomerates of spherical

granules, 3) spherulites, 4) hollow shells, and 5) dispersed, denser, spherical aggregates, all of which are shown in Figure 23.

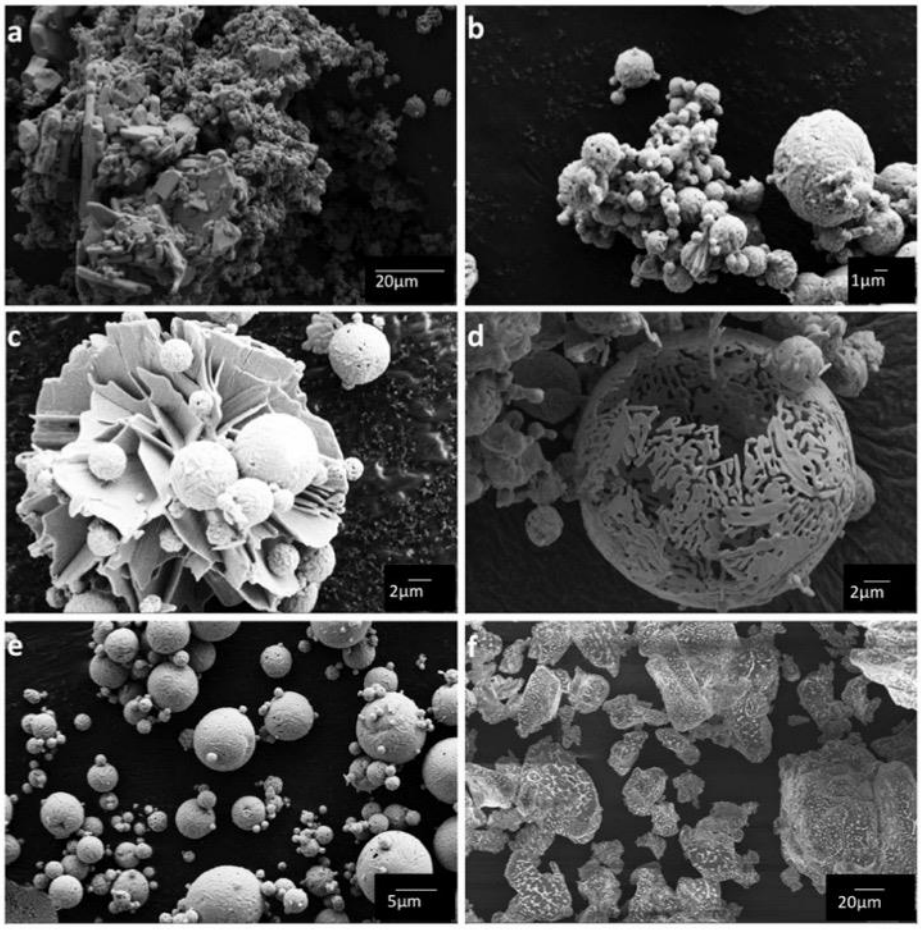

Figure 23 SEM micrographs show a) platelet aggregate particles, b) hard agglomerates, c) spherulites, d) hollow shells, e) dispersed, higher density, spherical aggregates and f) commercial hydrate powders.

The typical size distribution of dispersed, dense aggregate powders is shown in Figure 24. The lognormal distribution obtained by AZR-2X measurements is centered around 0.7 μm with a range of 0.1 μm to 7 μm. This distribution is slightly different than the particle size histogram obtained from SEM micrographs on the same powder sample. The discrepancy could be due to

the slight solubility of $BaCl_2$ in dichloroethane or the assumption of a lognormal distribution by the colloidal dynamics software. These SEM micrographs also show spherical aggregates are composed of elongated crystallites with an average length below 500 nm.

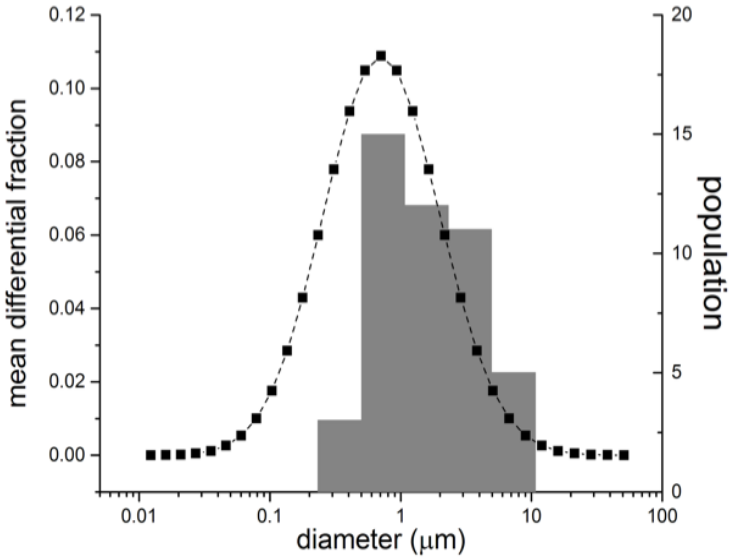

Figure 24 The particle size distribution of a dispersed, higher density, spherical powder sample corresponding to Fig. 2e is measured by the AZR-2x and scaled to the left hand axis. The population of particle sizes in Fig. 2e and a second higher magnification micrograph are represented in the histogram scaled to the right hand axis.

Comparison of XRD patterns collected from both commercial and spray dried powders with patterns from literature reveal the presence of different phases [126], [127]. Figure 25 shows the coincidence of the 4 strong peaks between 20^o and 25^o 2θ for the commercial powder (a) with those of the anhydrous reference pattern (e). The 3 strong peaks between 20^o and 25^o 2θ for the spray-dried powder (b) align with those of the mono-hydrate reference pattern (d).

The di-hydrate, which is the most stable form at atmospheric conditions, displays no strong diffraction peaks in the range of 20^o and 25^o 2θ. The fact that the di-hydrate does not appear in the

two patterns shown suggests that the hydration of powders in air during XRD measurements is not significant.

For a given solution feed rate, the predominance domains for the five powder morphologies described above were plotted as a function of the atomization gas flow and gas inlet temperature. In these processing maps, each domain indicates that a given morphology is more prevalent than any other. Despite the repeatability of the process, the statistical nature of this census yields maps in which domain boundaries are only approximate. Examples of these processing maps are shown in Figures 26 a-c. The next three sections give a qualitative analysis of these figures.

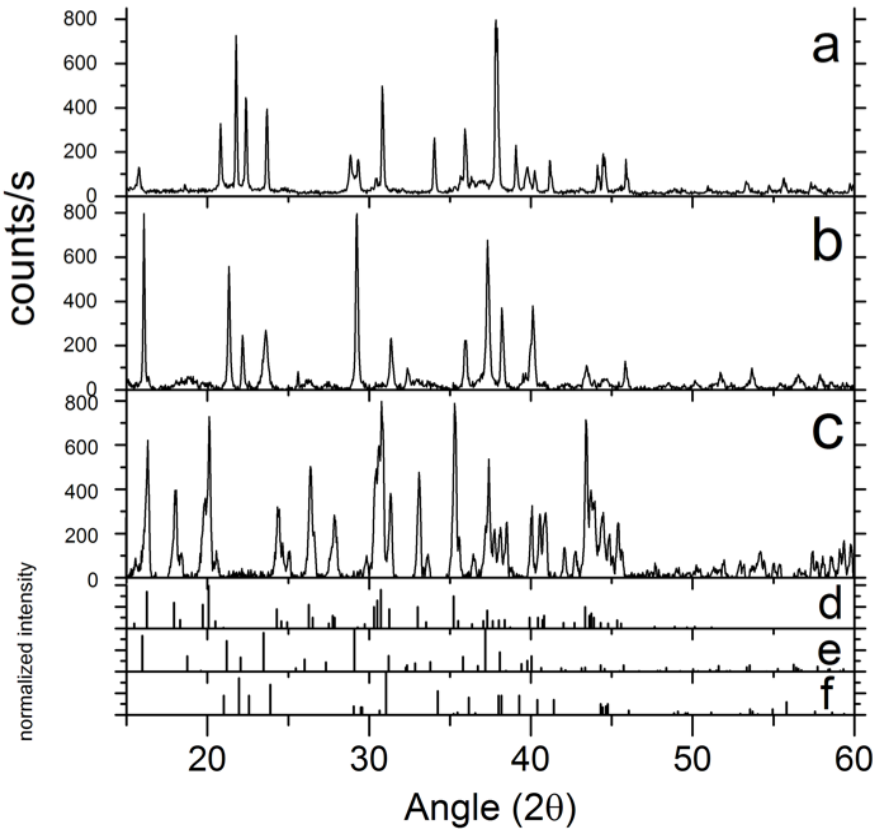

Figure 25 The x-ray diffraction patterns of a commercial powder sample (a) high density (b) and spherical, dispersed powder sample (c) are compared to the di-hydrate [126] **(d), mono-hydrate** [127] **(e), and anhydrous [126] (f) phases of BaCl2.**

At the low solution feed rate, moving from left to right along the temperature axis of Figure 26 (a), the particle morphology transitions from higher density particles to hollow spheres. Evaporation rate is expected to increase with inlet temperature, thus upsetting the balance between the evaporation rate and the ability of the solute to redistribute in the droplet. Moving along the y-axis, the gas flow rate increases. In other words, the solution is sprayed into a finer mist with a more turbulent flow. As a result, drying rates increase as the mean droplet size decreases, and it is expected that a similar change of granule morphology will be observed as in the case of temperature increase. However, large populations of shells are not observed at high gas flow rates. The increased velocity and turbulence with which the mist exits the nozzle at higher flow rate seem to dominate the particle formation process. These conditions may cause an increased number of collisions between droplets early in the drying process, leading to coalescence and the formation of hard agglomerates.

The last particle morphology in the 12 ml/min pump map is the spherulite. Attempts have been made to understand the formation of such particles, the consensus being that a high degree of undercooling and deviation from thermal equilibrium at nuclei-solution interfaces is required. [128,129] Spherulites in this study are always observed at high inlet temperature. According to calculations of Dalmez, the temperature profile within a droplet can be more than 12^{o}C and increases significantly with temperature in the case of spray dried milk [130]. Thus it is not unreasonable to find the conditions for spherulitic crystallization to be met in our experiments.

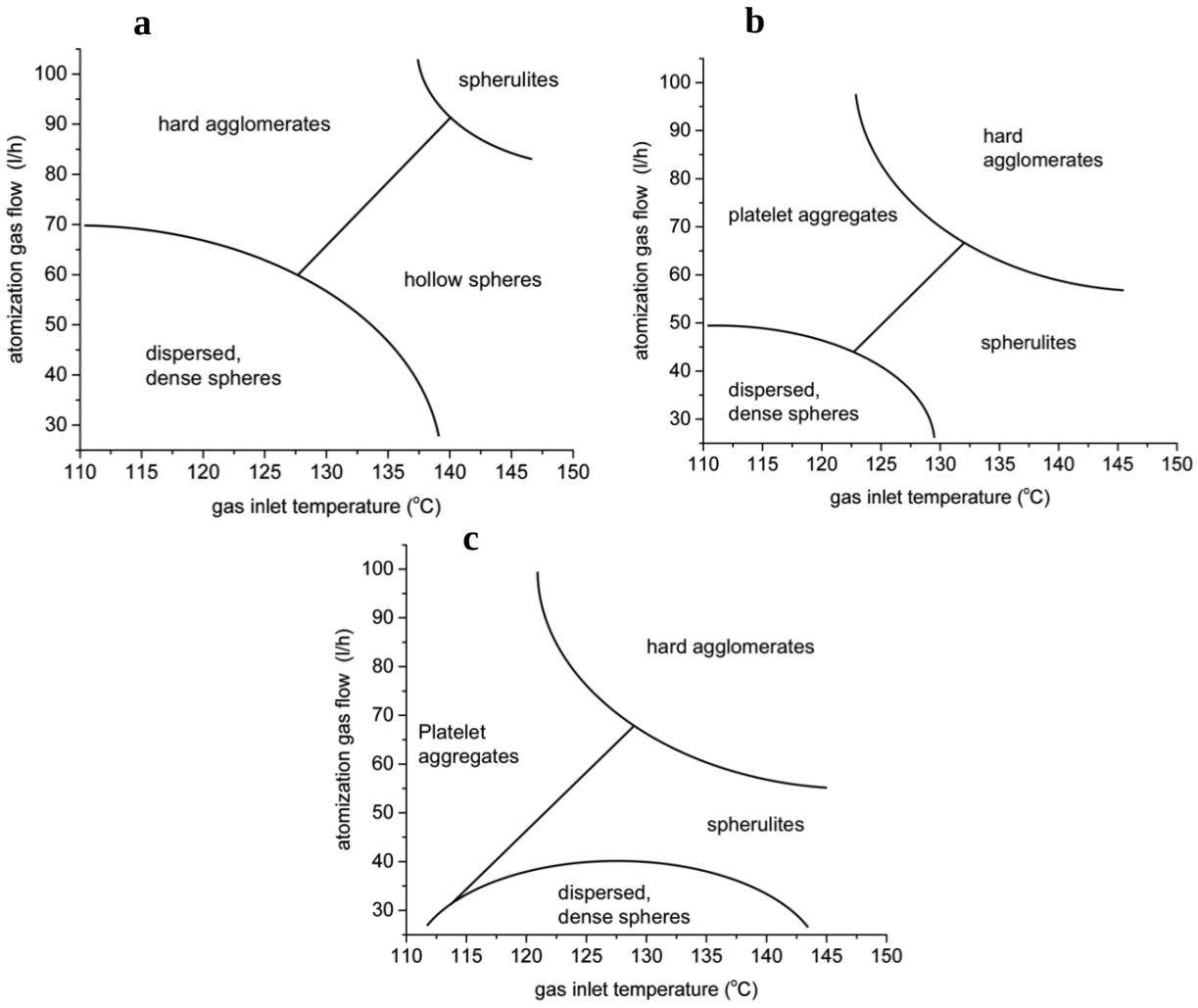

Figure 26 (a) A processing map for a concentration of 8.66g/100 ml and a solution feed rate of 12 ml/min shows morphology regions. (b) A processing map for a concentration of 8.66g/100 ml and a solution feed rate of 16.5 ml/min shows morphology regions. (c) A processing map for a concentration of 8.66g/100 ml and a solution feed rate of 21 ml/min shows morphology regions.

At the intermediate solution feed rate, the spherulite region increases in size, and the hard agglomerate region shifts to the right to make room for a different morphology, platelet aggregates (Figure 26b). The shift and growth of the hard agglomerate region occurs because more solution is introduced into the system, causing water vapor pressure to increase and drying rates to decrease. Collisions between droplets and damp particles are thus more likely. The platelet aggregates can be considered particles with larger primary grain size, which do not favor assembly into spherical

aggregates. At higher feed rates and lower temperatures, the drying rate is lower than at any point on the 12 ml/min feed map. The growth of precipitated nuclei may proceed to a greater extent under these conditions.

At the high solution feed rate, the only notable change in the processing map (Figure 26c) is the shift of all boundary lines towards higher temperatures. Higher feed rates increase the water partial pressure in the drying chamber, hence slowing down the drying rate. This in turn favors the formation of large crystallites and hard agglomerates. The region for formation of higher density, spherical aggregates is very limited at this flow rate.

3.1.4 Modeling the spray drier

In order to better understand the experimental conditions that favor the formation of dispersed, dense, spherical aggregates, and explain our experimental maps more quantitatively, we analyzed the balance between solvent evaporation rate and diffusional mass transport of the solute during the drying process. This approach has been well documented [131–133]. This balance can be written in the form of a dimensionless Peclet number as follows:

$$Pe = \frac{N}{\rho_l L D} \tag{3.1}$$

where N is the evaporation rate in kg/s, ρ_l is the density of the liquid phase in the droplet (hence N/ ρ is the corresponding volume of the liquid phase lost to the gas phase per unit time), D is the ambipolar ionic diffusivity of $BaCl_2$ in water and L is the characteristic length over which ionic diffusion proceeds, i.e. the radius of the droplet d/2. The evaporation rate is a function of the droplet surface area, A, the temperature difference between the drying gas and droplet surface, T_{gas} - $T_{droplet}$, the latent heat of evaporation for water H, and the heat transfer coefficient h at the gas-droplet interface:

$$N = \frac{hA(T_{gas} - T_{droplet})}{H} \quad (3.2)$$

To estimate the value of the heat transfer coefficient, one can use the definition of the dimensionless Nusselt heat transfer coefficient, Nu, (Eq. 3.3) and the Ranz-Marshall (R-M) correlation for combined laminar and turbulent flows in forced convection [134] (Eq. 3.4):

$$Nu = \frac{hL}{k} \quad (3.3)$$

$$Nu = 2.0 + 0.6Re^{0.5}Pr^{0.33} \quad (3.4)$$

with the Reynolds and Prandtl numbers, Re and Pr, given by Eq 3.5 and 3.6 respectively:

$$Re = \frac{\rho_g v L}{\eta} \quad (3.5)$$

$$Pr = \frac{\eta C_p}{k} \quad (3.6)$$

The definition of the Nusselt number involves the thermal conductivity of the droplet, k, and the characteristic length, L, over which the temperature gradient establishes itself at the liquid-vapor interface. It is assumed here that L~d/2. The definition of the Reynolds number involves the hydrodynamic characteristics dimension of the droplet, L~ d, as it moves at relative speed v in the airstream of density ρ_g and dynamic viscosity, η. The Prandtl number for the air flow involves the heat capacity of the gas, C_p, and its thermal conductivity, k. In order to satisfy the R-M relation, the Reynolds and Prandtl numbers must satisfy Re < 200 and Pr < 250, a situation easily fulfilled across the range of operating conditions used experimentally. [114]

The drying gas temperature, T_{gas}, which enters Eq. 3.2, is assumed to be equal to the inlet temperature (x-axis of the maps) measured just before it enters the drying chamber. The feed solution is partially warmed up as it travels down the nozzle and the droplet temperature, $T_{droplet}$, at the beginning of the drying stage, is estimated through the following energy balance equation between the inlet and the outlet of the drying chamber:

$$Cp_{H_2O,l}T_{i,H_2O} + m_{N_2}Cp_{N_2}T_{i,N_2} = m_{H_2O}Cp_{H_2O,v}T_{o,H_2O} + m_{N_2}Cp_{N_2}T_{o,N_2} +$$

$$m_{BaCl_2}Cp_{BaCl_2}T_{o,BaCl_2} + H_v m_{H_2O} - H_c m_{BaCl_2} + hA\Delta T_{wall} \quad (3.7)$$

Equation 3.7 establishes the conservation of free energy between the incoming and outgoing phases and includes the heat absorbed in the conversion of liquid water to vapor, the heat released by the crystallization of the salt and the heat lost through the wall of the drying chamber. The variables m, c_p and T are the masses, heat capacities and temperatures of each phases, and H_v and H_c are the latent heats of vaporization of water and of crystallization of $BaCl_2 \cdot nH_2O$, respectively.

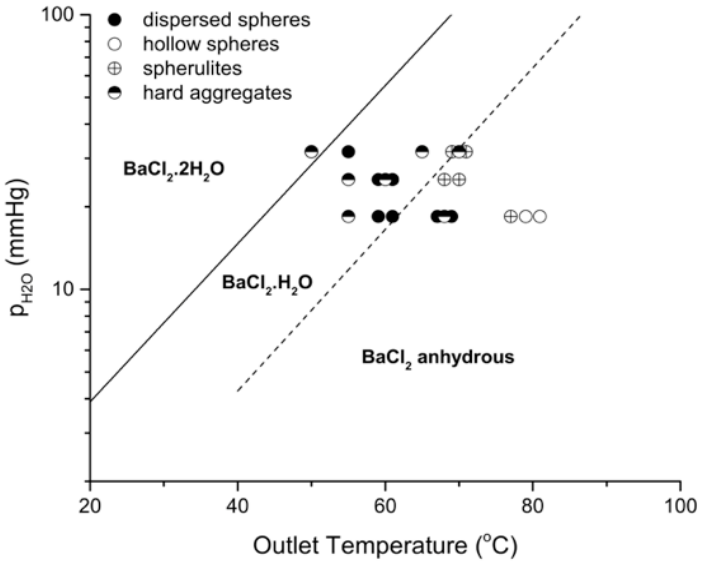

Figure 27 The water vapor pressure above solid $BaCl_2 \cdot nH2O$ at the outlet is calculated for a representative set of spray drying samples. The solid line represents equilibrium vapor pressure between the mono-hydrate and di-hydrate phases, while the dotted line represents the equilibrium vapor pressure between the anhydrous and mono-hydrate phases [42].

During the constant-rate evaporation stage, the temperature of the droplets is equal to the wet-bulb temperature and, at the inlet, $T_{droplet}=T_{i,H2O}$. Because of the small concentration of salt chosen for our experiments, the term corresponding to the release of heat due to crystallization, $H_c m_{BaCl2}$, can be neglected compared to the other terms. The heat loss at the outer surface of the drying chamber is assumed to be in steady state. This balance assumes (1) an isobaric and isochoric process in which no work is produced by the system and (2) all liquid water is converted into vapor. This last assumption is validated by calculating the partial pressure of water for 100% transfer of inlet liquid water to the vapor phase at the outlet. Calculated pressures are compared to the equilibrium partial pressures of water at the anhydrous-to-monohydrate and monohydrate-to-dihydrate transitions in Figure 27. The majority of conditions are expected to produce the mono-hydrate phase with the exception of spherulitic and hollow shell conditions, which are expected to produce the anhydrous phase.

The final term to be calculated for estimating N from Eq. 3.2 is the size of droplets (A), which is determined mostly by the nitrogen gas flow through the nozzle (y-axis in maps).
The average droplet diameter decreases with increasing gas flow. Various relations between the droplet size and operating conditions have been proposed in the literature for the type of two-fluid atomizer we are using. [135] The most accepted of which is given by Eq. 3.8.

$$d_{3,2} = \frac{535 \cdot 10^3}{v}\left(\frac{\gamma}{\rho}\right)^{0.5} + 597 \cdot 10^3 \frac{V_s}{V_g}\left(\frac{\eta}{\sqrt{\gamma\rho}}\right)^{0.45} \quad (3.8)$$

where $d_{3,2}$ is the Sauter mean diameter (SMD) of the droplets in μm; v is the velocity of the air relative to the liquid at the nozzle orifice (m/s); γ, ρ and η are the surface tension (N/m), density (kg/m^3) and viscosity (Pa·s) of the solution; and V_s and V_g are the volumetric flow rates of the solution and gas, respectively (m^3/s).

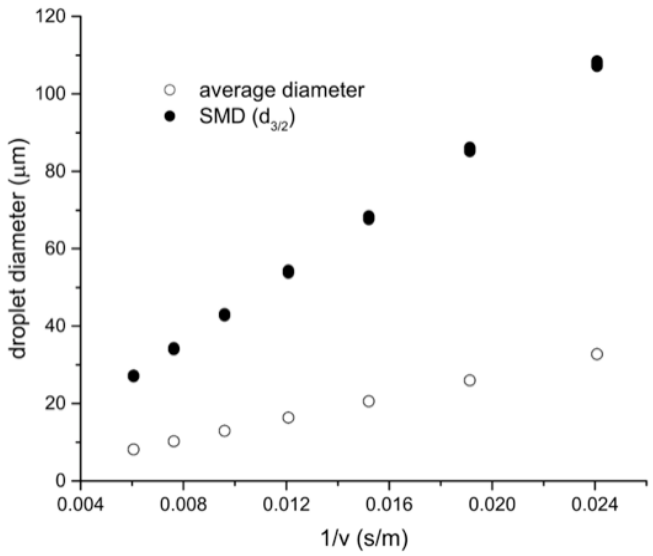

Figure 28 The $d_{3,2}$ deviates from the droplet size data reported in the spray dryer manual.

The SMD, $d_{3,2}$, is the diameter of a droplet having the same volume-to-surface area ratio as the entire spray, at the nozzle exit, and is the relevant measure of droplet size as far as evaporation is concerned. Figure 28 compares the SMD given by Eq. 3.8 and corresponding to the conditions used in this work to the size measured by the manufacturer of our spray-dryer [136]. As expected the SMD slightly exceeds the mean diameter of the droplets. $d_{3,2}$ was used for all calculations that follow.

The various physical quantities relevant to the problem and needed to solve Eq. 3.1 through 3.8 are listed in Table 4

Table 4 Physical constants used in the numerical simulation.

Constant	Value	Units	Ref.
$Cp_{H2O,l}$	4.2	$kJ \cdot kg^{-1} \cdot K^{-1}$	[137]
$Cp_{H2O,v}$	1.9	$kJ \cdot kg^{-1} \cdot K^{-1}$	[137]
Cp_{N2}	1.05	$kJ \cdot kg^{-1} \cdot K^{-1}$	[137]
Cp_{BaCl2}	0.639	$kJ \cdot kg^{-1} \cdot K^{-1}$	[42]
H_v	2260	$kJ \cdot kg^{-1}$	[42]
H_c	116.2	$kJ \cdot kg^{-1}$	[42]
ρ_{N2}	1.25	$kg \cdot m^{-3}$	[138]
η_{N2}	$2.67 \cdot 10^{-5}$	$Pa \cdot s$	[138]
k_{N2}	$3.14 \cdot 10^{-2}$	$W \cdot m^{-1} \cdot K^{-1}$	[138]
D_{Ba}	$3 \cdot 10^{-6} e^{-\frac{20230}{RT}}$	m^2/s	[139]
D_{Cl}	$4.33 \cdot 10^{-6} e^{-\frac{18980}{RT}}$	m^2/s	[139]

The mass flux of each phase is determined from calibration tables provided by Büchi [140]* for both gas flow driven by the aspirator and solution flow driven by the peristaltic pump. The feed solution calibration values were crosschecked by measuring the volume pumped in one minute,

* Solution feed in ml/min is given by 0.3P where P is the percentage setting of the pump. The atomization air flow in l/h follows an exponential relationship given by $109.6e^{0.046G}$, where G is the setting on the flow gauge. Finally, the aspirator influence on drying gas flow is tabulated. The flow is a constant 38 m^3/h for our experiments.

for each setting, using a graduated cylinder. Several simplifying assumptions are made with regard to the thermal masses appearing in equation 3.7: the heat capacity and density of the solution are approximated by those of liquid water since only dilute solutions of BaCl2 are used. Similarly, because the thermal mass of the gas introduced by the atomizer in the system is small in comparison to that of the other fluids entering the drying chamber, its contribution to the energy balance is neglected. It is further assumed that the phases at the outlet of the drying chamber are in thermal equilibrium, thus implying that $T_{o,BaCl2} = T_{o,N2} = T_{o,H2O} = T_{o,meas}$, where $T_{o,meas}$ is the outlet temperature recorded by the built-in sensor of the instrument. At steady state, the rate of heat loss through the walls of the vessel is constant and the heat flux carried by conduction through the walls is equal to that removed by convection from the outer walls by the surrounding air. The average temperature of the vessel's outer wall was measured for three different inlet and outlet temperatures and taken to be a linear function of the temperature drop between the inlet and outlet. Hence, solving equation 3.7 for $T_{droplet}$ and using this solution in equation 3.2, allows one to calculate the evaporation rate and the Peclet number as a function of the inlet temperature and gas flow.

The results of these simulations are represented on Figure 29. We verified that, for the range of parameters explored in this study, Re and Pr are approximately 1.5 and 0.89 respectively, and confirm the applicability of the R-M correlation. The shape of the contour map for the 12ml/min pump rate in Figure 29 shows increasing Peclet number both along the x- and y-axes. As per Fig. 26a, the semi-circular predominance domain for the higher density, dispersed particles at 12 ml/min feed rate intersects the temperature axis at 140^{o}C and the gas flow axis at 65 l/h. The contour line corresponding to a Peclet number of 0.6 approximates this predominance domain. As expected, lower Peclet number favors the formation of denser, dispersed particles. The quantitative

agreement between the calculated and experimental maps validates a posteriori the various assumptions of the model and demonstrates that this approach can be used in the optimization of powder fabrication with controlled morphologies. At the feed rates of 16.5 ml/min and 21 ml/min, the model does not correlate as well to experiments. A possible explanation is that Peclet number predicts trends in particle density without necessarily being correlated to agglomeration and other more complex morphologies. An interesting future study could involve the comparison of the model to a processing map based purely on particle density, and not more qualitative morphology descriptions.

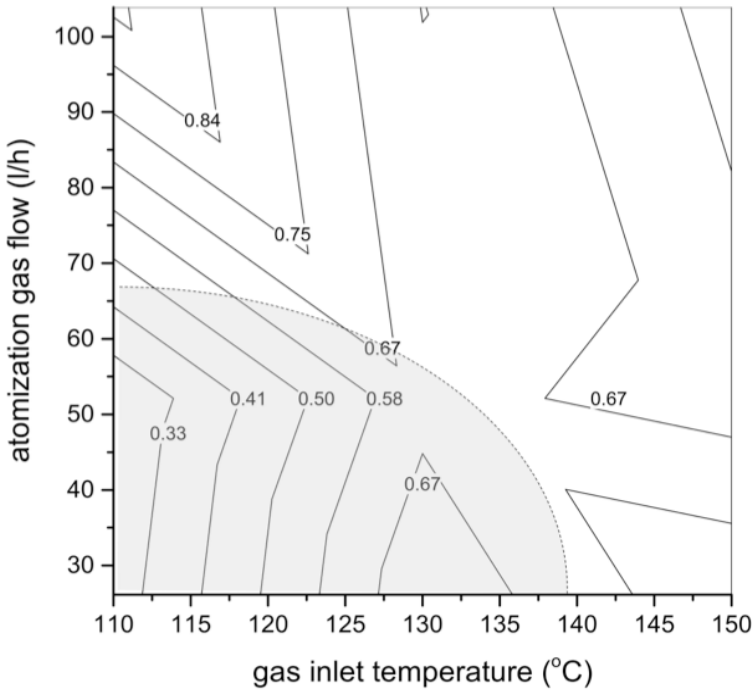

Figure 29 A contour map of Peclet number versus gas inlet temperature and gas flow for a pump rate of 12 ml/min and feed solution concentration of 8.66 g/100 ml shows good agreement with the experimental morphology boundary (grey shaded region) for higher density, dispersed aggregates.

The parametric study and subsequent modeling presented above have taught us how to produce spherical and dispersed particles. After some form of heat treatment to remove moisture

and in some cases close residual porosity, these particles are believed to be favorable for sintering. Still missing is an analysis of the dopant incorporation by the spray drying method, which will be covered in the next section.

3.2 Eu^{2+} dopant incorporation

We have introduced high purity $EuCl_2$ powders (Sigma Aldrich 99.99%) into our feed solutions at concentrations of 3 atomic % and adjusted the spray-drier parameters to produce the most favorable spherical, well-dispersed powders. These powders have been dried thoroughly in a tube furnace at 150^{o}C under a flow of high purity argon. Particle morphology was studied by SEM and doping uniformity was measured by energy dispersive X-ray spectroscopy (Thermo Fisher Noran System 7 EDX). For EDX measurements (Figure 30), working distance from the sample was 4mm and excitation voltage was 15 keV. Detector sensitivity was set at 5 and overvoltage at 1.5.

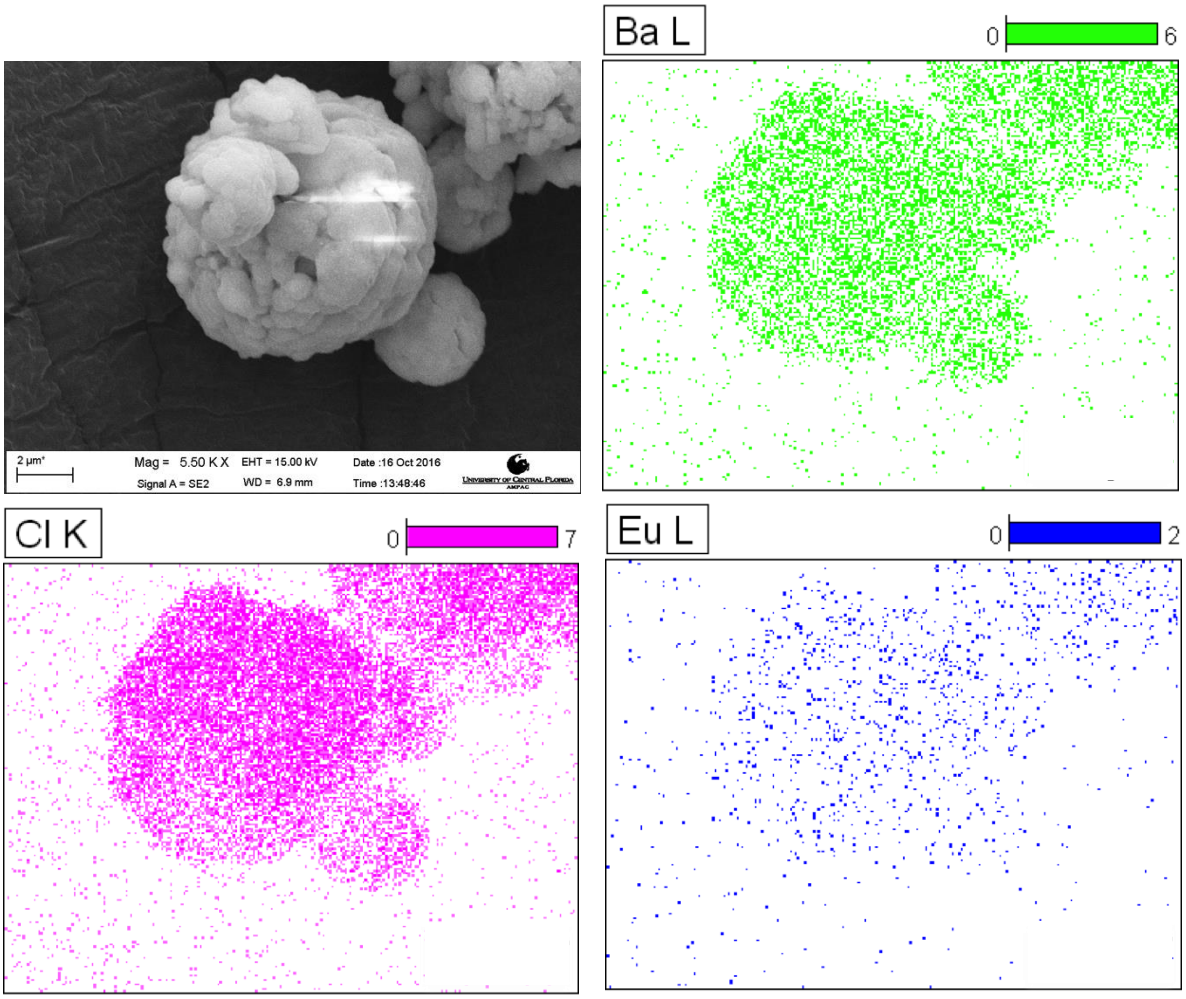

Figure 30 SEM micrograph of spray dried Eu:$BaCl_2$ powders. Three colorized EDX maps correspond to the distribution of Ba, Cl, and Eu within the frame of the image

SEM images show spherical particles with an average grain size well below 1µm. The grains do not have elongated shapes as seen in the pure $BaCl_2$ powders. EDX maps of Cl, Ba, and Eu show an even distribution across the powders.

3.3 Sintering behavior of spray-dried powders

A batch of spray-dried powders was prepared using the parameters suitable for producing spherical and well-dispersed powders as outlined above. Specifically, a solution of 9 g $BaCl_2$ was

prepared in 100 mL deionized water. The spray-drier was set at a solution feed rate of 12 mL/min, gas temperature of 120^{o}C, and gas flow rate of 50 L/h. After spray drying was complete powders were dried at 150^{o}C for 2 h to remove any water of hydration. Sintering experiments were conducted in an identical fashion to those in section 2.2.5 utilizing the custom designed press. Hot-pressing temperature was 450^{o}C and uniaxial applied load was 120 MPa. An example of a sintered sample is shown in Figure 31. The sintering curves at 450^{o}C for spray-dried powders look very similar to those of coarse, irregularly shaped commercial powders (Figure 32). Further analysis of the sintering behavior by way of the displacement curves is discussed in APPENDIX A.

Figure 31 Ceramic sintered from spray dried powder at 450^{o}C and 120MPa (SD1).

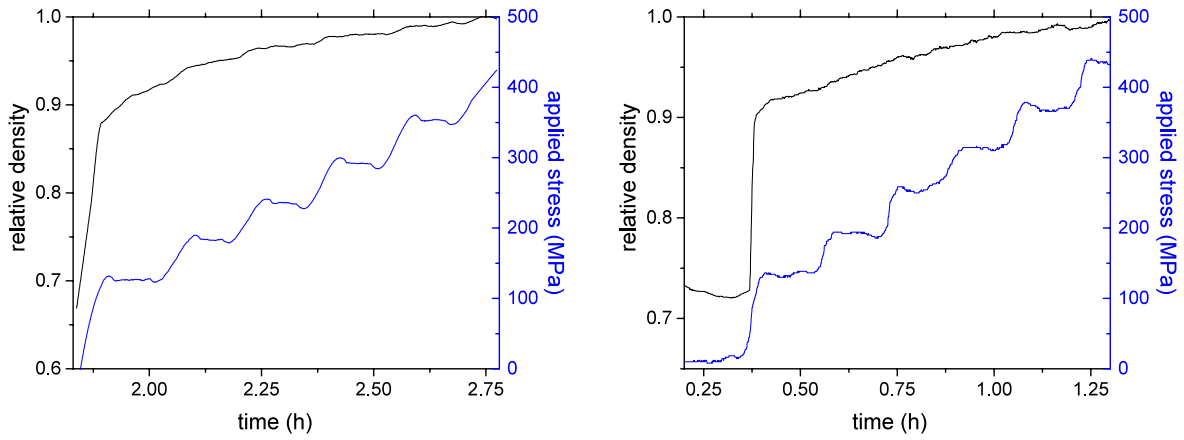

Figure 32 Sintering curves and pressure schedules for commercial (left) and spray-dried (right) powders at the sintering temperature of 450°C.

Transparency is not nearly as high in samples utilizing spray-dried powder as it is in samples utilizing ground commercial powders. Without extensive analysis, two effects are postulated. First, the residual porosity in the center of spherical particles leads to higher residual porosity in the sintered ceramic. Second, the nanometer scale grain size in the spray-dried particles translates to a higher mechanical strength in the powder compacts such that a full densification by plastic flow cannot be achieved at the pressure of 400 MPa.

3.4 Conclusion

Although the sintering behavior of spray-dried powders was not as good as expected, we managed to discover a systematic relationship between solution and spray-drying parameters and particle morphology $BaCl_2$ powders. This is the most comprehensive studies of spray drying of saline solutions in the context of ceramic processing to our knowledge. Initial attempts were made to transfer these findings to 3 atom % Eu^{2+} doped $BaCl_2$ powders. Working within the range of acceptable processing parameters to produce fine-grained, dispersed, and spherical particles,

preliminary results suggest that adding a dopant does not preserve the same processing-morphology relationships (elongated grains) of the pure powder. Nonetheless, doping is found to be uniform across particle surfaces.

The optimization of spray-drying $BaCl_2$ powders for the purpose of homogenous dopant incorporation and sinterability is still in the early stages. Future work should re-visit this subject. One interesting aspect will be to characterize the voids at the center of spherical particles and propose parameter adjustments and/or powder heat treatment guidelines to eliminate them. Furthermore, the use of water as a solvent in a class of materials with known susceptibility to oxygen-based defect formation is a potential concern. The absence of coloration in sintered pure $BaCl_2$ spray-dried powders and the exceptional results for sintering pure commercial $BaCl_2$ powders loaded outside the glove box (Chapter 2) suggest that excess moisture can be driven away at low temperatures ($<400^oC$) without creating high concentrations of color centers. The effect of spray-drying on color centers in Eu:$BaCl_2$ samples remains to be seen. Europium is expected to contribute to a higher susceptibility to color center formation. However, achievement of uniform doping profiles in a powder is the true novelty of the spray-drying technique.

In the remainder of this thesis, the powders used originate as millimeter sized beads from commercial suppliers. These have been more than sufficient to study size effects and temperature effects on sintered density and phase composition. Likewise, they should be sufficient to study the phase change sintering mechanism in the following chapter.

4. THE PRESSURE INDUCED ORTHORHOMBIC-TO-CUBIC PHASE CONVERSION

Sintering studies thus far have acted mainly to narrow in on the powders, pressure, and temperature ranges appropriate for densifying $BaCl_2$ ceramics. This chapter examines the sintering mechanism from the standpoint of plasticity and the stress-induced reverse martensitic conversion in $BaCl_2$. One might propose to map the transition pressure as a function of temperature, however, the targeted application in this thesis has the unique requirement of transforming the phase of a powder compact for the purpose of densification. Thus, the transition must be studied at a microscale. Experiments are designed to access the widest range of pressures at temperatures on the microscale. Altering particle size will have a much greater impact than the macroscopic applied load on the microscopic loads experienced particle-to-particle. Thus, investigations of both particle size and temperature are used to study the phase transition during the sintering of $BaCl_2$

4.1 Effect of particle size on sintering

High purity anhydrous o-$BaCl_2$ powders (99.999% metals basis, Sigma Aldrich) and anhydrous sodium chloride powders (99% metals basis, Sigma Aldrich) were ground with separate alumina mortar and pestles and separated with stainless steel mesh sieves to achieve the four different particle size distributions (Table 5). The mesh sizes of 400, 200, 100, and 50 correspond to opening sizes of 37, 75, 150, and 300 μm respectively. The table entries correspond to powders collected above the stated mesh size unless otherwise indicated. The o-$BaCl_2$ powders were then pre-compacted at 3 MPa into 13 mm-diameter pellets. These pellets were loaded into a 25-mm diameter floating stainless steel die assembly and surrounded by loosely packed sodium chloride.

Table 5 particle size test matrix for 12 ceramic samples

$BaCl_2$ mesh size		<400	200	100	50	unsieved
NaCl mesh size	<400			CP1		
	200			CP2		
	100	CP5	CP6	CP3	CP7	CP8
	50			CP4		

All sieving and press loading was performed in an argon-filled glovebox. The hot-pressing die was held inside the custom-designed hot-press chamber described in Chapter 2 [141]. The first series of 12 samples was pressed at a temperature of 450^{o}C and a uniaxial load of 6350 kg-force (127 MPa). Pressure was increased manually, in a stepwise fashion, at a rate of 1000 kg-force every 10 minutes. Real-time densification and pressure data were recorded for analysis of the sintering behavior

Ceramic samples were analyzed for crystalline phase by x-ray diffraction using a PANalytical Empyrean with PIXcel detector. Scans were in the 2θ-range of 20 to 70^{o}, with a step size of 0.0492^{o} and an integration time of 150 s/step. Such a high integration time is necessary due to the high attenuation of x-rays by barium.

Fracture surfaces were examined for grain size and porosity in the SEM. Samples were scored with a diamond blade and broken seconds before mounting with conductive carbon tape and sputtering 1nm of gold. Grain size was determined from SEM micrographs by the intercept method.

4.1.1 Results

Performing x-ray diffraction experiments on this material while avoiding the reaction of samples with ambient air has proven difficult. The structure begins to transform from anhydrous orthorhombic $BaCl_2$ to hydrated orthorhombic $BaCl_2 \cdot H_2O$ in a matter of minutes. After several hours, the structure has completely transformed into hydrated monoclinic $BaCl_2 \cdot 2H_2O$. Attempts have been made to limit exposure to air by covering samples with Kapton film. Even with this additional precaution, we are not confident in the phase analysis of this set of samples. The new procedure developed for accurate XRD analysis is covered in Chapter 4.2.

Sample transparency ranged from very good when the sieve used was coarser than 100 mesh for both $BaCl_2$ and NaCl (CP7), to moderate at $BaCl_2$ mesh sizes of 400 (CP5), to very poor at an NaCl mesh sizes of 400 (CP1) as represented in Figure 33. It is also clear that the transparency is more sensitive to NaCl particle size than $BaCl_2$ particle size. Through examination of fracture surfaces in a subset of the samples (constant NaCl row, CP5-8, in Table 5) we see that particle size and distribution strongly affect the sintered grain size.

Figure 33 A comparison of 2 mm-thick samples sintered using coarse NaCl and $BaCl_2$ powders (CP7), fine $BaCl_2$ powders (CP5), and fine NaCl powders (CP1).

At a constant NaCl particle size sieved through 100 mesh, the first observation is that average sintered grain size[4] decreases significantly when moving from a wide $BaCl_2$ particle size distribution in an unsieved state (CP8) to a narrower, sieved distribution where only the larger particle population is present (CP3, CP6, CP7) as seen in Figure 35. All grain size relationships in this constant NaCl size sample series is plotted in Figure 34. At its smallest, the sintered grain size seems to be on the order of 1 μm on average as viewed in the SEM (Figure 35, CP7), which is two orders of magnitude smaller than the initial particle size viewed in SEM (Figure 23f).

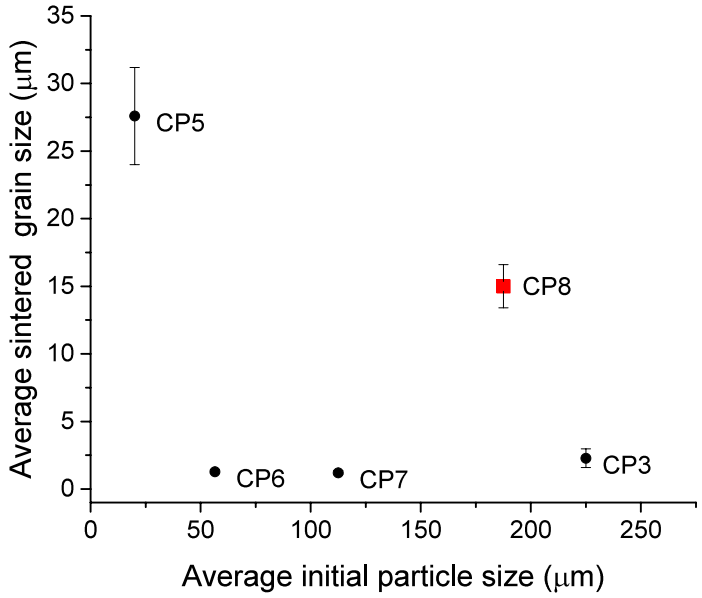

Figure 34 Effect of particle size on grain size at the pressing temperature of 450°C and the sieved NaCl particle size of 75-150 μm. The red point corresponds to unsieved $BaCl_2$ powder.

[4] In this section, grain size is taken as the size of the fracture boundaries viewed in SEM. Later XRD analysis reveals this to not be entirely accurate in the case of cubic samples. However, it is assumed that pre-transformation grain sizes should be reflected in the fracture boundary sizes.

This is evidence of a large degree of fragmentation and/or recrystallization during hot-pressing. In the context of the phase change sintering mechanism, the latter case will be examined later in this chapter. At the constant NaCl particle size, as long as the smallest particles (<400 mesh) are not present, the grain size is small and the transparency is similar to that of sample CP7 in Figure 33. If only small particles are present, as in CP5, the transparency is at a minimum and the grain size is at its maximum.

For the series of samples having a constant $BaCl_2$ mesh size of 100, the main observation is a severe decrease in density when moving towards smaller NaCl particle sizes. This is demonstrated in the SEM images of samples CP4 and CP1 shown in Figure 36. The porosity is clearly visible, but difficult to quantify in these fracture surface images.

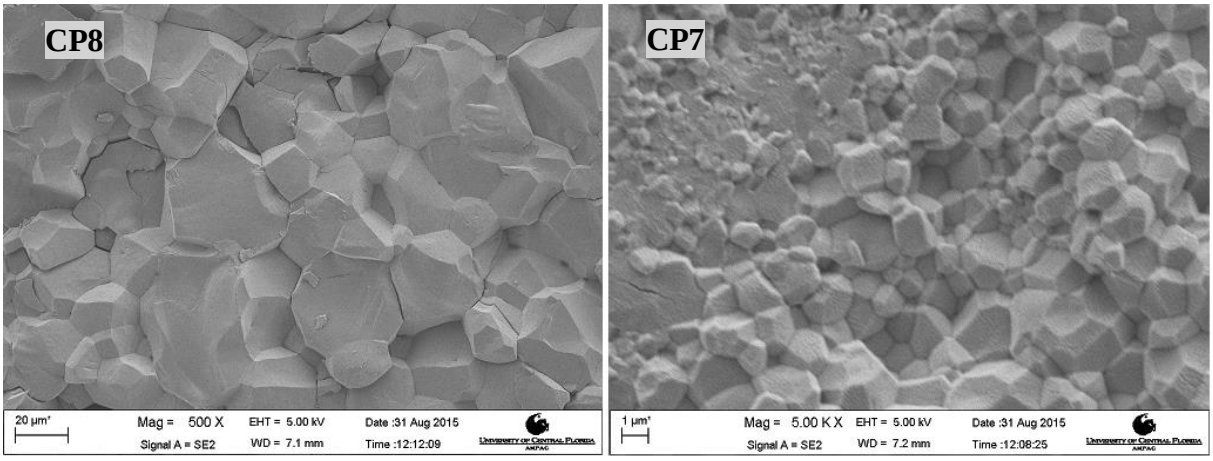

Figure 35 SEM micrographs depicting a) large grain size in unsieved $BaCl_2$ powders (CP8) and b) small grain size in a powder sieved with 100 mesh (CP7).

The clear boundaries visible in the higher density samples are not visible in the low density samples. However, there appear to be a large number of sub-micron grains. In sample CP4, the

boundaries are not as small as those for the coarser sieved $BaCl_2$ particle sizes in the first series of samples (CP3, CP6, CP7). We are not sure of the origin of this discrepancy.

In addition to the SEM analysis of samples using varying particle sizes, densification curve analysis was also attempted. So far, these results do not show any meaningful trends. For more on this analysis, refer to APPENDIX A.

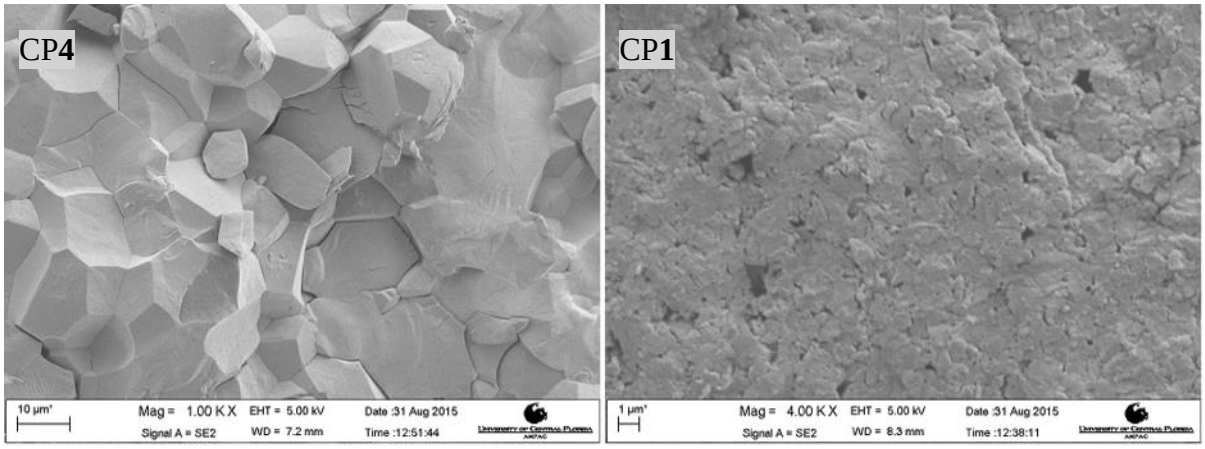

Figure 36 SEM micrographs depicting a) high density in a sample pressed with the large NaCl particle size (CP4) and b) low density in a sample pressed with small NaCl particle size (CP1).

4.1.2 Discussion

By studying the effect of particle size and morphology on sintering, guidelines can now be put in place in order to achieve complete densification, small grain size, and high transparency. Large $BaCl_2$ and NaCl particle sizes (>50 μm) with a narrow size distributions are preferred. Much like the conclusions drawn from sintering experiments of spray-dried powders, the increased hardness and strength of finer powders is expected to be a major limitation to density and transparency. In addition to a Hall-Petch effect, the more vigorous mechanical grinding required to create the finer powders (<38 μm) may have some strain hardening effect on the powders.

Finally, the fine, irregularly shaped powders may lead to higher aggregation during die filling and the initial stages of compaction resulting in lower density.

In terms of the predicted phase-change sintering mechanism, the set of samples presented in Chapter 4, Section 1 have not undergone reliable XRD analysis. It was realized early that examination of samples in the air is insufficient, as successive patterns change drastically. A special sample holder with a Kapton cover sheet is not even sufficient to prevent moisture absorption by samples. A new test method for XRD will be presented in the next section and applied to a new set of samples pressed at different temperatures in order to confirm the phase change sintering method.

4.2 Effect of pressing temperature

The new study investigates pressing temperatures between 400ºC and 500ºC and uses identical powders ground and sieved using 100 mesh sieves as identified in the previous section. The phase of these samples is analyzed by x-ray diffraction using an XPert^3 MRD diffractometer equipped with a Cu/K_α radiation source and a PIXcel detector array in a Bragg–Brentano geometry. Samples were loaded into an Anton-Parr DHS-1100 hot-stage and protected from the atmosphere by a graphite dome held under $3x10^{-1}$ mbar vacuum during the entire measurement. Non-ambient temperature experiments were also performed on the Anton Parr hot-stage within the range of 25 to 350ºC to observe the phase evolution of as-pressed samples. A slow heating rate of 10ºC/min and a dwell of 10 min were programmed between each temperature step. Phase and Rietveld analyses were conducted using the HighScore Plus software version 4.1 from PANalytical.

For characterizations by transmission electron microscopy (TEM), 150 to 250 nm-thick samples were obtained by milling with a Zeiss 1540 focused ion beam (FIB) equipped with a

scanning electron microscope (SEM). A 30-nm layer of Au/Pd was sputtered on the surface and welded to a probe to allow for sample lift off. The surface to be examined was perpendicular to the polished surface of the ceramic. The sample was transferred immediately to the TEM sample holder, with a maximum of 5 min exposure to air for each sample. The resulting specimens were examined in an FEI Tecnai F30 TEM operated at 300 kV using both conventional bright-field imaging, and Selected Area Electron Diffraction (SAED).

Differential scanning calorimetry (DSC) measurements were carried out with a Netzsch model 204. Two successive scans from room temperature to 400°C were performed on 1x2x2 mm chunks of ceramic held inside aluminum crucibles with lids. The scanning rate was between 10°C/min and 20°C/min.

4.2.1 Characteristics of as-pressed samples

Figure 37 shows a side-by-side comparison of samples pressed between 400 and 500°C. On this picture, the $BaCl_2$ core of each sample is surrounded by the outer rim of pressure-transmitting NaCl. The most transparent $BaCl_2$ samples are produced at 450°C and the slight differences in temperature on either side of this temperature optimum drastically reduce the transparency.

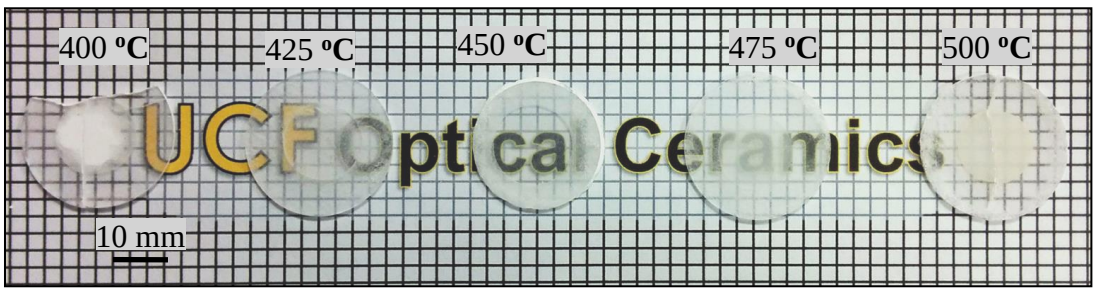

Figure 37 Side-by-side comparison of 1 mm-thick $BaCl_2$ ceramic samples hot-pressed at five different temperatures. The $BaCl_2$ core of each sample is surrounded by an outer rim of NaCl.

XRD patterns have been recorded for samples pressed at a range of temperature between 400 and 500°C (Figure 38). Samples pressed at 400°C mostly exhibit the peaks of o-$BaCl_2$ (cotunnite, Pnma, #62). The intense peaks centered at 28.5° and the plateau beginning at 45° 2θ in figure 32, originate from the graphite dome, used to protect the sample from the ambient atmosphere. Traces of NaCl contamination (peak at 31.5° 2θ) are visible in the samples pressed at 400 and 500°C. When the pressing temperature reaches 425°C, the peaks predominantly correspond to c-$BaCl_2$ (fluorite, Fm-3m, #225) with a small volume fraction of o-$BaCl_2$. Samples pressed at 450°C exhibit a similar phase composition to those pressed at 425°C. At 475°C, only a small fraction of c-$BaCl_2$ is present, and none is found at 500°C.

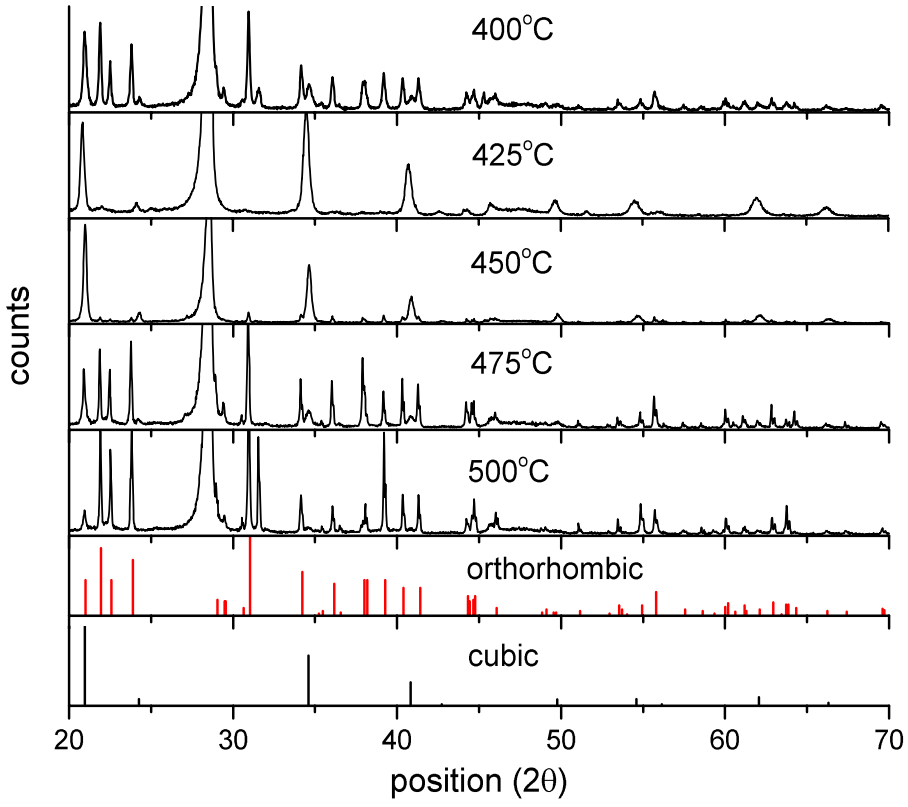

Figure 38 XRD patterns of ceramics pressed between 400 and 500°C under 6350 kg-force. Orthorhombic and cubic peak positions are displayed according to ICD references PDF-98-026-2674 and PDF 00-024-0095 respectively.

The lattice parameters of each phase were found to be within 0.16% of the literature data (Table 6). Contrary to our experiments, the cubic $BaCl_2$ sample referenced in [142] was prepared by rapid quenching from 925°C to room temperature (ICD database PDF 00-024-0095). To our knowledge, it is the first time that cubic $BaCl_2$ is produced by hot-pressing at such a low temperature.

Table 6 Room temperature values of the lattice parameters of barium chloride orthorhombic and cubic phases as determined from x-ray diffraction and compared to literature data. The last row shows the ratios dilation between the parameters and volumes of the orthorhombic and cubic cells (a_{ortho}/a_{cubic}, b_{ortho}/a_{cubic}, c_{ortho}/a_{cubic}, V_{ortho}/V_{cubic}).

	a (Å)	b (Å)	c (Å)	V (Å^3)	Ref
o-$BaCl_2$	7.8776±0.0002	4.7360±0.0001	9.4357±0.0003	352.03	[This work]
(Pnma)	7.865	4.731	9.421	350.55	[143]
c-$BaCl_2$	7.315±0.0002	-	-	391.42	[This work]
(Fm-3m)	7.311	-	-	390.78	[142]
Dilation ratio	1.077	0.647	1.290	0.900	

Quantitative phase analyses performed by Rietveld refinement were used to assess the phase composition of the samples pressed between 400 and 500°C, as well as the residual strain and crystallite size of the major phase (Table 7). In the table, f_{ortho} and f_{cubic} correspond to the calculated weight percent of orthorhombic and cubic phase, respectively. Columns designated with G and ε correspond to the grain size and micro-strain in each sample, respectively. Instrumental broadening was accounted for by calibrating against a coarse, strain-free, tungsten powder sample using the same divergence, receiving slits and beam mask. One can notice from Figure 38, that the c-$BaCl_2$ peaks are broader than those of o-$BaCl_2$, and that, for a given phase, the peak width decreases with increasing processing temperatures. At temperatures of 475°C and above, the peak width of o-$BaCl_2$ is outside the acceptable range for broadening analysis.

Table 7 Rietveld refinement parameters obtained on $BaCl_2$ ceramic samples pressed at varied temperatures.

Temperature (°C)	f_{cubic} (wt %)	G_{cubic} (nm)	ε_{cubic} (%)	f_{ortho} (wt %)	G_{ortho} (nm)	ε_{ortho} (%)
400	15	-	-	85	145±100	0.396±0.015
425	99	44±1	0.262±0.004	1	-	-
450	94	72±2	0.273±0.004	6	-	-
475	11	-	-	89	259±26*	<0.1
500	0	-	-	100	22500±650S	<0.1

* **broadening analysis is typically inaccurate in this size range**

S **calculated by intercept method on fracture surface of SEM image**

Broadening analysis identifies nano-sized and strained grains in the sample pressed at low temperature (400°C). When the temperature is raised and the cubic phase becomes the predominant one, the grain size is even smaller, and some micro-strain remains. These observations are consistent with a recrystallization event with limited growth and subsequent plastic deformation. We would expect the original cubic phase to precipitate as strain-free grains, so we expect that plastic deformation has imparted some strain to the cubic phase. Finally, samples pressed at 475 and 500°C have negligible strain and grain size outside the limits of broadening analysis. These observations suggest that the ductility of particles is higher at higher temperatures (less fragmentation).

The same samples were also examined in the SEM. Samples exhibiting predominantly the cubic phase show small fracture domains on the order of 1 μm (Figure 39). These are significantly larger than the crystallite sizes calculated from XRD line broadening. In higher temperature orthorhombic samples the observed fracture boundaries are much larger (22 μm), but there is no reliable XRD size analysis for comparison.

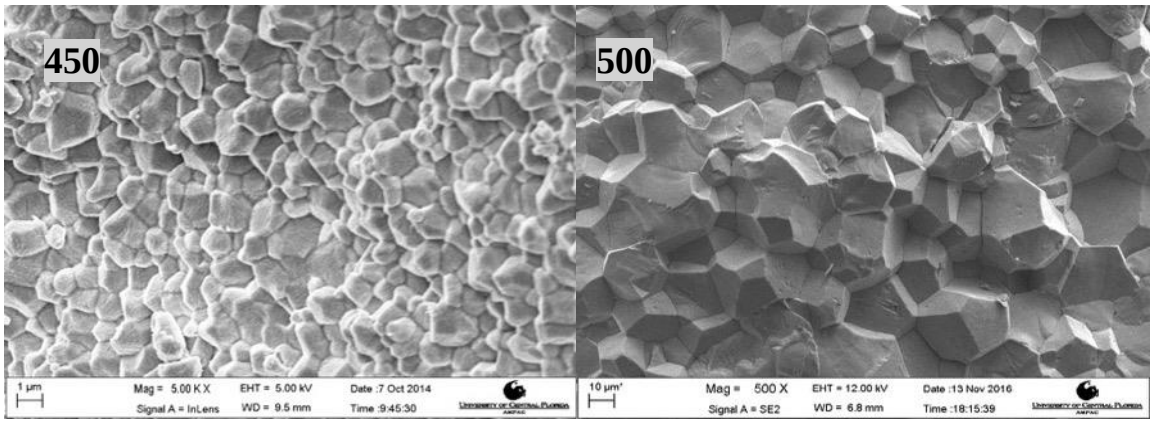

Figure 39 SEM micrographs of the fracture surfaces of a $BaCl_2$ ceramic samples pressed at 450°C and 500°C. The visible boundaries are an order of magnitude higher in the 500°C sample.

To confirm the presence of highly nano grain boundaries and determine the orientation relationship between the cubic and orthorhombic phases in this never before visualized phase equilibrium in $BaCl_2$, TEM analysis was used. A ceramic sample processed at 450°C, and exhibiting the highest transparency and the highest fractions of cubic phase, was selected for TEM analysis. Figure 40a shows a highly porous slice isolated from the bulk of the ceramic. The porosity content, estimated by image analysis on three 2x2 µm square sections, is between 2.7 and 5.8% by area. The average size of circular pores is below 30 nm, but channel like pores have longer dimensions on the order of hundreds of nanometers. SAED confirms the presence of c-$BaCl_2$ and the absence of o-$BaCl_2$. Individual grains are difficult to make out in the images due to their small size relative to the thickness of the sample. The extremely small grain size observed by TEM (30 – 100 nm) in Figure 40b is not consistent with the 0.5 to 1 µm domains viewed at the fracture surface in SEM, but is consistent with the XRD analysis in Table 7.

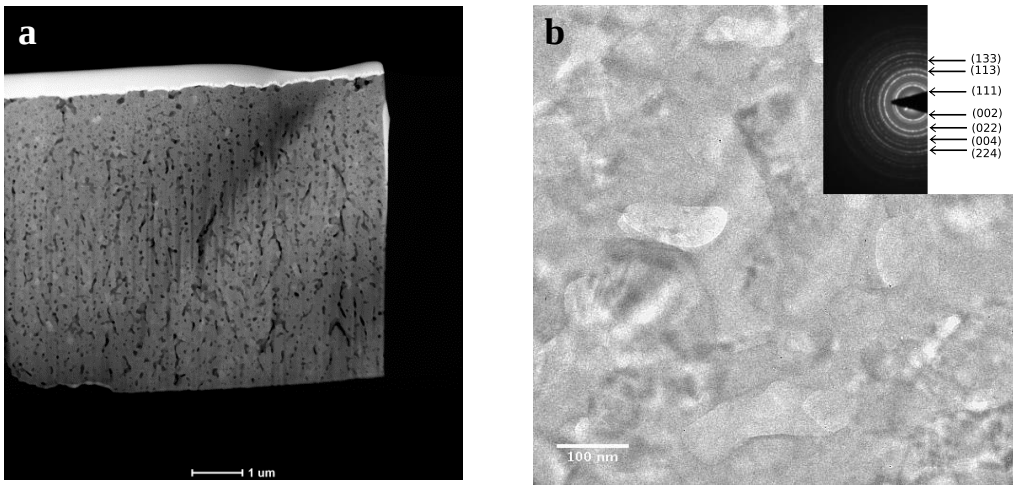

Figure 40 (a) SEM micrograph showing the fracture surface of a sample pressed at 475ºC. (b) Bright-field TEM image with indexed SAED pattern in insert, corresponding to the $BaCl_2$ cubic phase.

In an effort to isolate a section with both cubic and orthorhombic grains, a second sample was extracted from the bulk of the same ceramic. This sample reveals the presence of an untransformed orthorhombic grain (Figure 41-1) sharing an interface with a polycrystalline cubic $BaCl_2$ region (Figure 41-2). The diffraction pattern obtained by SAED has been indexed according to the 0 1 0 zone axis, with all d-spacings and interplanar angles agreeing well with those measured by XRD. However, due to the small grain size of the cubic phase, and the limitations of SAED, we were not able to determine the orientation relationship between the cubic and orthorhombic phases at the interface.

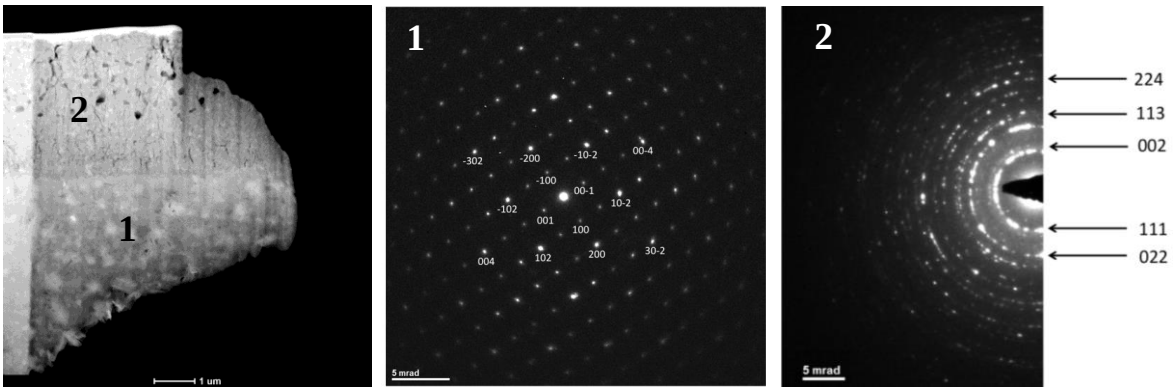

Figure 41 A second slice of the 450ºC sample showing the interface between an orthorhombic $BaCl_2$ single-crystal (1) and a cubic (2) polycrystalline region, as revealed by SAED (left images).

4.2.2 Temperature stability of the cubic phase

As seen above, a large molar fraction of the cubic phase is quenchable down to ambient conditions. Once at room temperature, c-$BaCl_2$ ceramics have been shown to remain stable for at least 12 months. In fact, annealing experiments carried out by x-ray diffraction on a hot-stage indicate that c-$BaCl_2$ does not fully revert to the orthorhombic phase until temperatures of about 300ºC (Figure 42a). Phase quantification by Rietveld analysis reveals that only small amounts (<14%) of orthorhombic phase are present below 300ºC and that phase reversion occurs very sharply thereafter (Figure 42b).

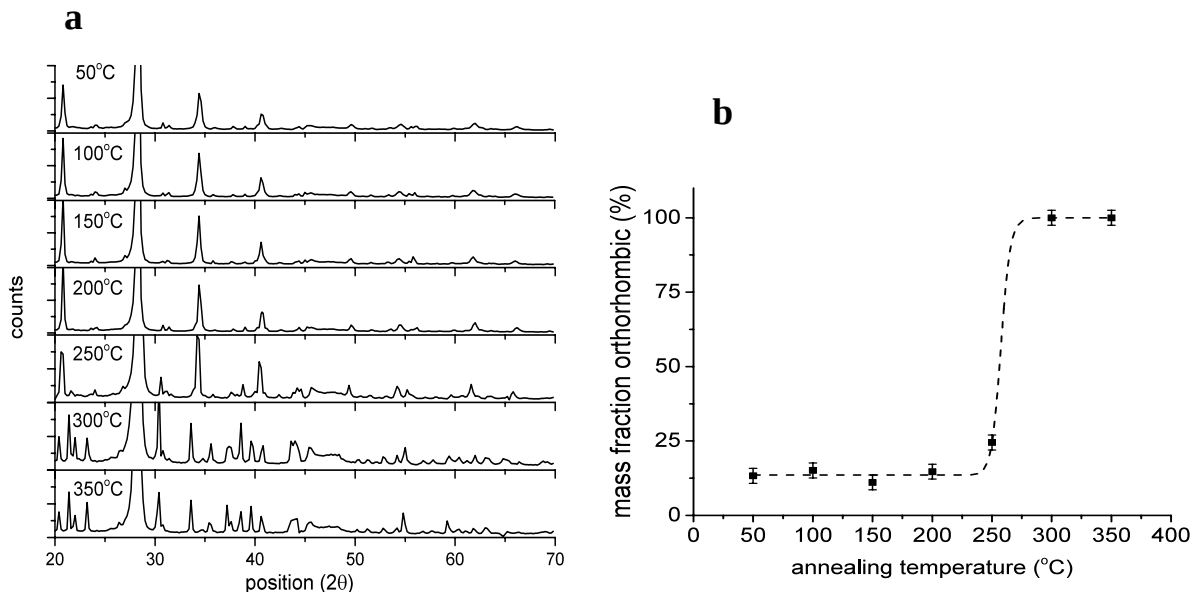

Figure 42 (a) XRD patterns collected under vacuum and at increasing annealing temperatures on a single sample of $BaCl_2$ ceramic, initially pressed at 450°C. (b) Mass fraction of orthorhombic phase determined by Rietveld refinement. The dashed line is to guide the eye only.

It is worth noting that differential scanning calorimetry experiments carried out at temperatures up to 400°C (a temperature slightly higher than the temperature range covered by the XRD experiments shown in Figure 42), show no specific thermal signature associated to the phase reversion detected by XRD near 250°C (Figure 43).

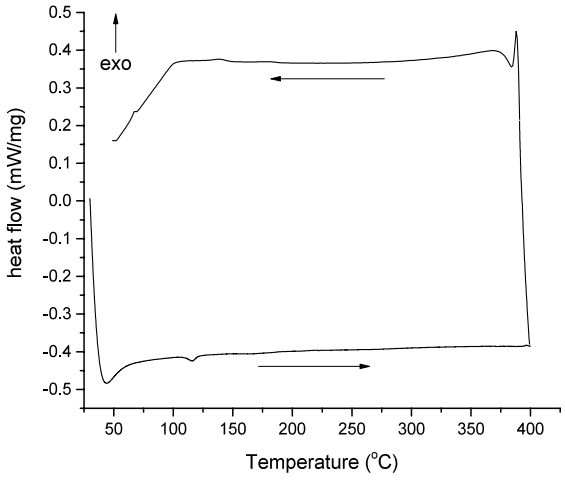

Figure 43 DSC signal trace for a piece of c-$BaCl_2$ ceramic sample.

4.2.3 Discussion

By hot-pressing with an NaCl pressure transmitting medium, we have showed that $BaCl_2$ powders undergo an orthorhombic-to-cubic phase transition, which enables their densification and the production of transparent ceramics. We now discuss the conditions pertaining to this unusual approach.

4.3 Nature of the observed transition

Previous high-pressure studies, carried out in diamond anvil cells (DAC) at ambient temperature, have revealed that orthorhombic $BaCl_2$ converts, to so-called post-cotunnite polymorphs of higher coordination with monoclinic and hexagonal symmetries, at 7 and 21 GPa, respectively [15,16]. These values lie far outside the range of pressures attainable by our press, which we estimate to be well under 2 GPa, that is, if we account for a tenfold stress-intensification factor in the early stages of powder compaction [99,144]. Also, contrary to DAC, our conditions

can produce a large amount of shear [145]. Moreover, the lack of thermal signature associated to the phase conversion (Figure 43) is consistent with a shear-induced athermal martensitic transition [146]. The symmetry-breaking operation between the fluorite spacegroup Fm-3m, with Wyckoff positions *4a*, *8c* and *8c*, and its cotunnite subgroup Pnma, with Wyckoff positions *4c*, $4c_1$ and $4c_2$, is characterized by the coordinate transformation matrix T=[(0 0 1)(-1 ½ 0)(1 ½ 0)], with origin offset P=[½ ¼ ¾], [147–149]. With these, one can derive the lattice parameters and orientation relationships between the cubic and orthorhombic cells as well as show that this transformation preserves the cell volumes:

$$\boldsymbol{a}_{ortho} = a_{cubic}[001]_{cubic} \tag{4.1}$$

$$\boldsymbol{b}_{ortho} = a_{cubic}\frac{\sqrt{2}}{2}\frac{[110]_{cubic}}{\sqrt{2}} \tag{4.2}$$

$$\boldsymbol{c}_{ortho} = a_{cubic}\sqrt{2}\frac{[1\bar{1}0]_{cubic}}{\sqrt{2}} \tag{4.3}$$

$$V_{ortho} = V_{cubic} \tag{4.4}$$

We find that the experimentally determined cell dilatation ratios (a_{ortho}/a_{cubic}, b_{ortho}/a_{cubic}, c_{ortho}/a_{cubic}) differ slightly from the theoretical values (1, 0.707, 1.41) and that the volume of the orthorhombic and cubic cells is not conserved as a truly martensitic transformation would. In fact, using DFT calculations, S. Boulfelfel *et al.* predicted a transformation path in calcium fluoride (CaF_2), a compound structurally analogous to $BaCl_2$, which includes a component of shearing in the cation sublattice [85] and in support to these discrepancies. However, our TEM analyses were not able to determine an orientation relationship between the orthorhombic and cubic lattice cells that would further validate this mechanism.

As proposed by A.G. McLellan [88], one can use a Clausius-Clapeyron relationship to estimate the magnitude of shear stress, $\tau = -\frac{\Delta s_{\alpha\beta}}{v_o}\frac{\Delta \mathrm{b}}{\mathrm{b}}\Delta T$, necessary to initiate the reverse

martensitic transformation on a single grain of o-$BaCl_2$. With the experimental transformation strain $\Delta b/b$=1-0.65 and temperature shift ΔT=500°C, an entropy variation $\Delta s_{\alpha\beta}$=14 J/mol/K [24], and a molar volume v_o=55x10^{-6} m^3/mol, one finds τ=45 MPa. It is difficult however to relate to the nominal uniaxial stresses in our press, as this equation will only predict the resolved shear stress acting on a single pair of similarly oriented particles. Given the random orientation of the powder compact, the nominal uniaxial stress would in fact need to be much higher in order to initiate transformation in almost all grains. Because this formulation does not seem to describe a powder compact adequately under a complex state of stress, we propose the following method to describe this phase transition.

4.4 Modeling a stress-induced transition in a powder compact

The elastic behavior and phase composition under stress in a polycrystalline material has been treated by micromechanical methods involving the homogenization of elastic properties, as well as a free-energy based phenomenological approach for application to dense shape-memory alloys [150,151]. In its simplest form and limiting this discussion to the first thermodynamic principle, i.e. neglecting energy dissipation rates during the powder compact deformation, the effect of combined isostatic and shear stresses on the phase content can be approached as follow. The free-energy of the mixture of phase is written as [88,152,153]:

$$\mu = \lambda_\alpha \mu_\alpha + (1 - \lambda_\alpha)\mu_\beta + E_{coh}(\lambda_\alpha) \tag{4.5}$$

where μ_α and μ_β are the chemical potentials of the cubic (α) and orthorhombic (β) phases, λ_α ($0 \leq \lambda_\alpha \leq 1$), the degree of advancement of the phase conversion and, $E_{coh}(\lambda_\alpha)$, a coherence energy term. Under a state of stress characterized by the tensor σ_{mn}, the chemical potential of each phase *i* (*i*=α,β) becomes:

$$\mu_i = \mu_i^o + S_{klmn}^i \sigma_{mn}\sigma_{kl} \tag{4.6}$$

where μ_i^o is the chemical potential in the absence of any external stress and $S_{klmn}^i$the compliance tensor. At equilibrium, $\frac{\partial \mu}{\partial \lambda_\alpha} = 0$, and one finds:

$$\Delta\mu_{\alpha\beta}^o + \frac{\partial E_{coh}}{\partial \lambda_\alpha} = \frac{1}{2}(S_{klmn}^\alpha - S_{klmn}^\beta)\sigma_{mn}\sigma_{kl} \tag{4.7}$$

which becomes, after separating the isostatic (σ) and deviatoric (s_{mn}) components of the stress tensor ($\sigma_{mn}=\sigma\delta_{mn} + s_{mn}$):

$$\Delta\mu_{\alpha\beta}^o + \frac{\partial E_{coh}}{\partial \lambda_\alpha} = \frac{1}{2}\Delta S_{kkmm}^{\alpha\beta}\sigma^2 + \frac{1}{2}\left[\Delta S_{klmm}^{\alpha\beta} s_{kl} + \Delta S_{kkmn}^{\alpha\beta} s_{mn}\right]\sigma + \frac{1}{2}\Delta S_{klmn}^{\alpha\beta} s_{mn} s_{kl} \tag{4.8}$$

In their polycrystalline forms, the compliance tensors of the orthorhombic and cubic phases reduce to isotropic forms (e.g. Hill average), which allow further simplification:

$$\Delta g_{\alpha\beta} = \Delta\mu_{\alpha\beta}^o + \frac{\partial E_{coh}}{\partial \lambda_\alpha} = \frac{1}{2}\Delta K^{\alpha\beta}\sigma^2 + \frac{1}{2}\Delta S_{44}^{\alpha\beta} J_2 \tag{4.9}$$

In this expression, J_2 represents the second deviatoric stress invariant, whereas $\Delta K^{\alpha\beta} = K^{\alpha,poly} - K^{\beta,poly}$ and $\Delta S_{44}^{\alpha\beta} = 1/G^{\alpha,poly} - 1/G^{\beta,poly}$ are the differences in isothermal compressibilities and shear modulus reciprocals between the polycrystalline forms of c- and o-$BaCl_2$ respectively. Hence, Eq. 5 takes a form akin to a von Mises condition for plastic yield:

$$1 = \left(\frac{\sigma}{\sqrt{\frac{2\Delta g_{\alpha\beta}}{\Delta K^{\alpha\beta}}}}\right)^2 + \left(\frac{\sqrt{J_2}}{\sqrt{\frac{2\Delta g_{\alpha\beta}}{\Delta S_{44}^{\alpha\beta}}}}\right)^2 \tag{4.10}$$

in which the elliptical branch, represented by Eq. 6 in the plane of stress invariants (σ, $\sqrt{J_2}$), defines the locus of the orthorhombic-to-cubic phase transition.

4.5 Phase-change sintering

The process of phase-change sintering results from the interplay between the yield of the powder compact (through the rearrangement of grains and the plastic deformation of individual particles above a given yield stress), a reverse martensitic transformation (enabling the formation of a crystalline phase of high-symmetry providing additional slip systems) and an associated flow rule under specific states of stress.

The continuously changing characteristics of the microstructure (e.g. porosity, grain refinement) and their effects on the mechanical properties of the densifying ceramic complicate, at present, any attempt at a thorough quantitative analysis of the overall process. While values of the free-energies are referenced in the NIST-JANF database [89], only DFT-calculated values of the elastic constants have been determined by Kumar and Vadeshwar [154] and Curtarolo *et al.* [155]. In addition, most temperature dependencies of the terms entering equation 4.10 are unknown. However, to illustrate our concept of stress-induced phase-change sintering, we can schematically represent the loci for yield and phase change along with typical loading paths for a powder in closed die compaction (Figure 44). The loading pathway accounts for the multiple stages of powder compaction, including particle flow, rearrangement and plastic yield. For samples pressed at 425^{o}C and 450^{o}C, the loading path must develop such that the phase change locus is exceeded (Figure 44, trajectory ①). Provided the phase change is complete, the powder can now yield on any of the six primary slip systems (001)[110] of the c-$BaCl_2$ fluorite structure in order to densify further. In the case of a lower pressing temperature, the phase change locus is broader and cannot be reached within the pressing die. In the case of a higher pressing temperature, deviation in the yield and phase change loci is such that the loading path takes the sample above its yield strength, relaxing the state of stress to a value below the phase change locus.

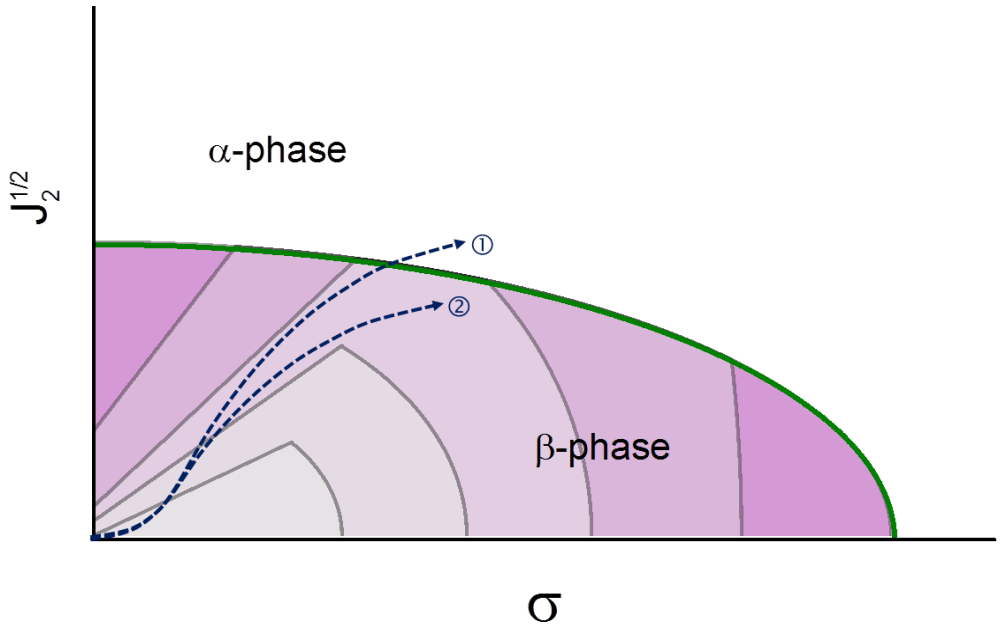

Figure 44 Schematic conditions for ceramic phase-change sintering via stress-induced reverse-martensitic transformation. The x- and y-axes represent the isostatic and deviatoric stresses respectively. The grey lines depict the yield loci of powder compacts, with darker shades of pink corresponding to increasing powder compact densities. The green line defines the locus of phase transformation between the martensite (β-phase) and austenite (α-phase). Successful conversion to the α-phase is achieved when the strength of the β-phase powder compact allows for sufficient elastic energy storage (trajectory ①). Trajectory ② corresponds to a traditional compaction route without phase conversion.

Upon creation of finely grained c-$BaCl_2$ phase from nucleation and growth during the martensitic transformation combined with subsequent plastic deformation, a moderate cooling rate of 500^{o}C/h is sufficient to quench the phase to room temperature and maintain that stability upon re-heating. Previous studies were only successful in quenching coarse grained c-$BaCl_2$ when stabilized with up to 12.5% lanthanum or cerium [60]. In this study, the stability of the cubic phase is contributed to the nano-structuring of c-$BaCl_2$.

The reverse martensitic transformation that we report here, and which can only operate in ceramic materials exhibiting diffusionless polymorphic transitions, complements the list of deformation processes, such as grain rearrangement, grain boundary sliding and diffusion

processes that are more traditionally used in ceramic processing. Due to the improved optical isotropy of the sintered samples, this technique is groundbreaking for the field of transparent ceramics even beyond the scintillator application.

5. OPTICAL CHARACTERIZATION OF $BaCl_2$ CERAMICS

As interesting as phase-change sintering is as a processing technique, the most important finding in the context of the motivation behind this work is the high transparency of cubic $BaCl_2$ ceramics. High transmittance is a necessity for scintillators, because the photons generated at europium sites in the volume of the scintillator, should escape to the photodetector. In the case of strongly colored samples, the blue light emitted a europium centers will be absorbed in the scintillator and not detected. In non-absorbing samples, transmittance will also be affected by scattering, whose contributions, identified by XRD and electron microscopy, include birefringence in o-$BaCl_2$, residual o-$BaCl_2$ embedded in c-$BaCl_2$, cracks, and porosity. The scattering is not directly relatable to our performance benchmarks of high light yield, good energy resolution, and good proportionality, however it can play a role when the optical path length of a photon is long enough such that the probability of absorption increases.

The optimization of a novel $BaCl_2$ ceramic processing technique to achieve high transparency is the capstone of this thesis. Yet, the process was designed keeping in mind the sensitivity of the scintillation process to certain charged defects. The next phase of research will be to characterize scintillation behavior of Eu:$BaCl_2$ samples. As the preparation of Eu:$BaCl_2$ powders by spray-drying has not yet been optimized, the incorporation of the dopant is achieved by melting the two materials in a sealed quartz ampoule. Two different raw-material feed-stocks have been used, a colorless 5% Eu:$BaCl_2$ single crystal grown at LBL, and a melt of 5% Eu:$BaCl_2$ prepared at UCF. Both feed-stocks have been ground, sieved, and pressed in accordance to the procedure developed in Chapter 4. For comparison, we also show the results of some early Eu:$BaCl_2$ samples prepared by sintering of $EuCl_2$ – $BaCl_2$ mixtures in the at 450^{o}C.

To probe for the presence of defects linked to additional emission centers present in Eu:$BaCl_2$, techniques of UV and x-ray excited luminescence are used. The presence of optical trapping states is investigated with the technique of thermally stimulated luminescence. Finally, to test the scintillation performance of these samples, the light yield and energy resolution are derived from pulse height spectroscopy measurements using a Tl:NaI standard sample.

Optical characterization will be separated into two main categories: First, the in-line transmittance ranging from the UV to the near IR and broadband IR photography to characterize the passive optical properties, and second the spectroscopic techniques used to study the scintillation process.

5.1 Optical Transmission

During the phase-change sintering studies, samples covering a broad range of microstructures and optical transmission were generated. The size and volume fractions of the three main components of microstructure, bulk phase, residual phase, and porosity, are used to deconvolve the transmission spectra on the basis of scattering theory. Appropriate scattering models are chosen based on the size, shape, concentration, and refractive index contrast of scatterers and in accordance to prior application of scattering theory to birefringent transparent ceramics including Al_2O_3 [40,41,156] and MgF_2 [43,157].

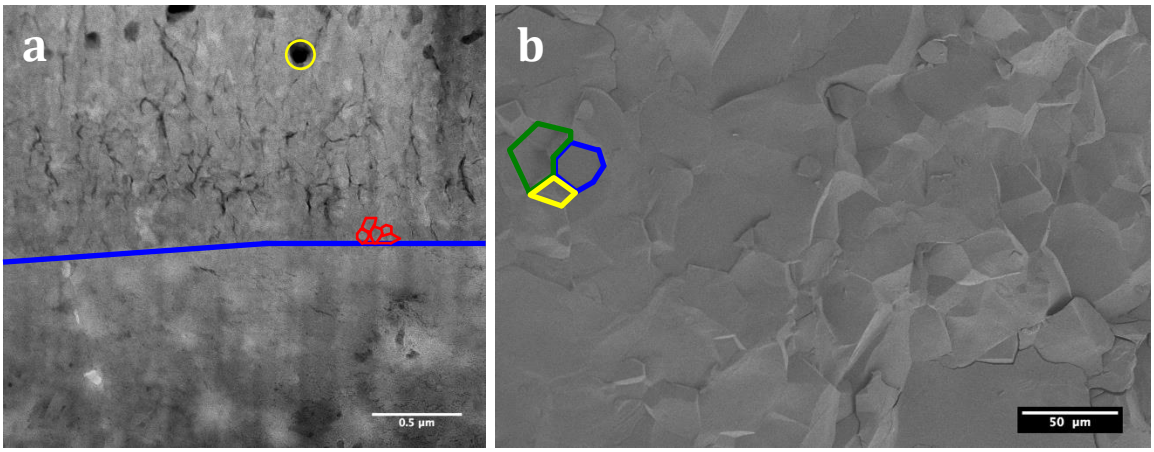

Figure 45 Representation of scattering sources identified by SEM and XRD. a) a ceramic composed of a majority nano-sized cubic grains (red), micrometer-sized orthorhombic grains (blue), and pores (yellow). b) a purely orthorhombic ceramic with randomly oriented grains. Colors are added as indication of variance in refractive index.

Two types of samples have been generated in this work, birefringent pure phase o-$BaCl_2$ (Figure 45b) and mixed phase $BaCl_2$ with residual porosity (Figure 45a), both of which are represented in the figure. For birefringent o-$BaCl_2$ ceramics with a small refractive index contrast between neighboring grains in the size range of tens of micrometers, Raman's model for multiple scattering in an inhomogenous media applies. This simple model, in which the crystal (of thickness D) is divided into cubic blocks of equal size d with two different refractive indices n_1 and n_2 is illustrated in Figure 46 [158]. Neglecting reflection and refraction effects, this "three-dimensional phase grating" will produce – due to the statistically fluctuating distribution of the n_1 and n_2 blocks – phase shifts between the pencils of lights, which transmit a row of D/d domains. As a consequence, diffracted wave fronts emerge behind the crystal in various directions, producing a "scattering halo". The experimental transmission is given by the ratio between I and I_0 and presented in the following formula (5.1). I_0 is the incident plane wave of intensity and emerges in its original direction with an attenuated intensity I.

$$T(\%) = \frac{I}{I_0} = (1 - \mathrm{R})^2 \exp(-\nu^2 \Pi^2 \Delta n^2 K D d) \quad (5.1)$$

where the "filling factor" K is determined by the relative amount of the n_1 and n_2 blocks (K_{max} = 1 for equal amounts).

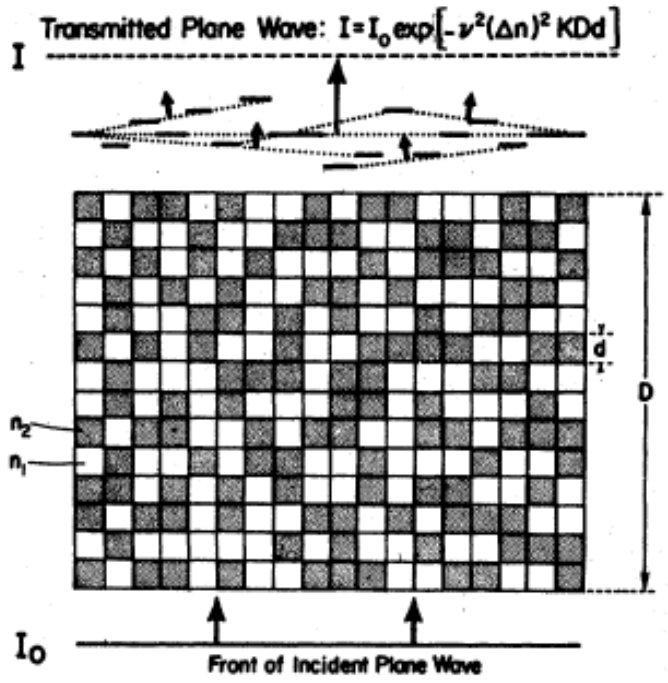

Figure 46 Schematic illustration of Raman's model for light scattering in optically inhomogeneous materials.

The scattering coefficient of a grain boundary takes the form:

$$\gamma_{gb} = \frac{\pi^2 \Delta n^2}{\lambda^2} G \quad (5.2)$$

where Δn is the maximum contrast between refractive index between misoriented grains, and G is the grain size. The c-$BaCl_2$ samples experience no birefringence scattering, but do have small concentrations of pores and residual phase o-$BaCl_2$. Because the pores are very small in size and the refractive index contrast between a pore (n~1) and the bulk ceramic (n~1.7) is so large, the scattering approximation above is not valid and a numerical solution to scattering efficiency must

be derived from Mie scattering theory. Assuming the scatterers have spherical geometry and are embedded in a continuous, optically homogenous matrix, the scattering coefficient for a small concentration of residual phase or a small concentration of porosity take the form:

$$\gamma_{p,r} = \frac{p}{\frac{4}{3}\pi r^3} C_{sca} \tag{5.3}$$

where p is the volume fraction occupied by porosity, r is the average radius of a pore or grain of residual phase, and C_{sca} is the Mie scattering cross-section of a single pore or grain. The calculation of real inline transmittance (RIT) accounting for reflection at the surfaces and scattering from the different sources in the volume of sample takes the form:

$$RIT = (1 - R_s)^2 \exp(-\gamma d) \tag{5.4}$$

$$R_s = \frac{2R'}{1+R'} \tag{5.5}$$

$$R' = \left(\frac{n-1}{n+1}\right)^2 \tag{5.6}$$

Here, R_s is the reflection loss at a surface at normal incidence, γ is the scattering coefficient, and d is the thickness of the sample.

5.1.1 UV-Vis-NIR spectrophotometry

Transmission measurements were made using a CARY 500 spectrophotometer in the spectral range of 200-2000nm. Samples were ground to a thickness of 1 mm and polished with dry alumina powders on tall nap polishing cloths inside the glovebox and held in the glovebox until just prior to measurement. Samples were centered in the beam path between the source and detector to limit the scattering angle accepted by the detector, and 3mm spots were masked off for measurement. Background and zero transmission measurements were collected for baseline correction.

Figure 47 shows an experimental RIT curve for a sample hot-pressed at 850°C, which has an average grain size of approximately 20μm as measured by SEM. A theoretical transmission curve according to the Raman model and accounting for $\Delta n=0.006$ (the average of the difference between the three principle axes in o-$BaCl_2$) and G=20μm is plotted on the same axes, and reflections based on a refractive index of ~1.7 (the wavelength dispersion calculated by Singh is used to increase accuracy). The model underestimates the transmission of the sample. One source of this discrepancy is the fact that the transmission measurements are not technically in the RIT geometry. The large size of the detector compared to the illuminated sample area allows for some scattered photons to be detected. For comparison, a theoretical transmission with G=5μm is also plotted. Both theoretical curves fail to predict the shape of the transmission spectra. Another source of error is the elimination of an absorption contribution to the transmission. Because this sample is darkly colored this term cannot be neglected.

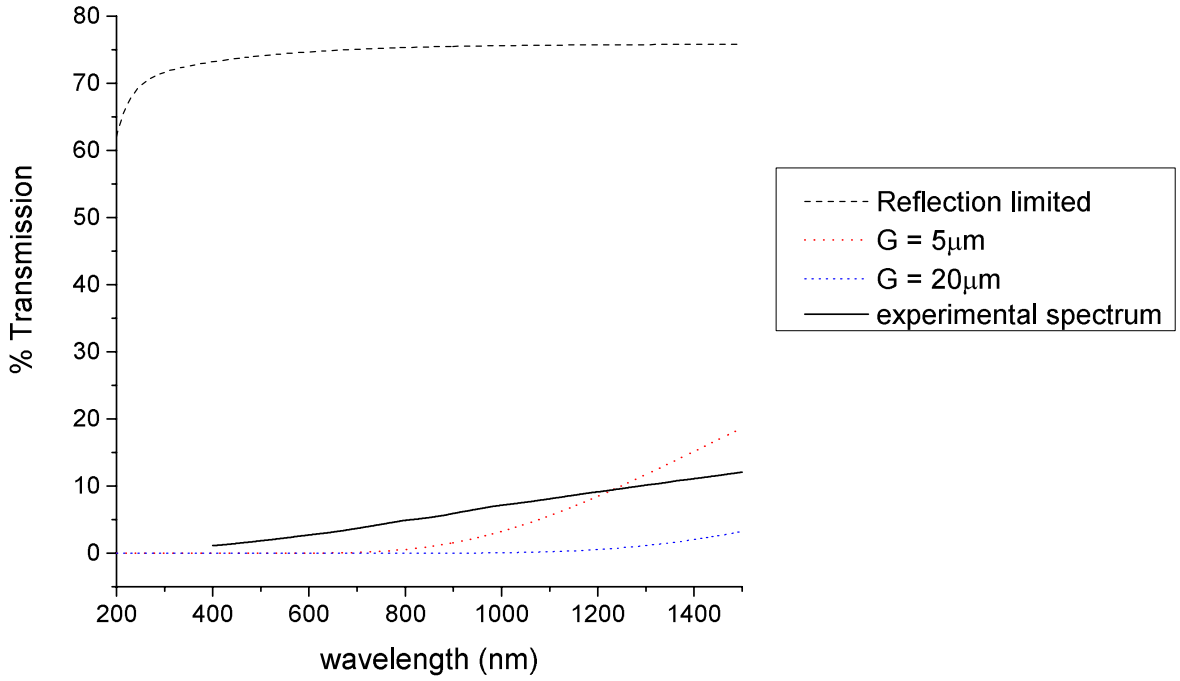

Figure 47 Transmission spectrum of a large grained o-$BaCl_2$ sample hot-pressed at 850ºC compared to the Raman model curves accounting for birefringence scattering in monodisperse from monodisperse scatterers of 5μm and 20μm.

A second transmission spectra is presented in Figure 48 as an example of the mostly cubic sample described in Figure 47a. To fit the experimental data, Mie scattering cross sections were calculated as a function of wavelength assuming $\Delta n=0.7$ between a pore and the bulk ceramic, and r=100 nm. To calculate the extinction a porosity of 0.1% was used (the porosity is not uniformly distributed so this average was difficult to estimate). The effect of 8 volume % residual o-$BaCl_2$ with an average grain size of 5μm is treated separately using an estimated $\Delta n=0.01$ (the refractive index of c-$BaCl_2$ is not known). In the final Beer-Lambert expression, the two Mie contributions are added. Results of the calculation are plotted in Figure 48. Again, the model does not accurately predict the shape of the transmission curve. One source of discrepancy could be that the pores

have a wide distribution. This distribution could be accounted for in future modeling efforts, however the pore size distribution was not known in this case.

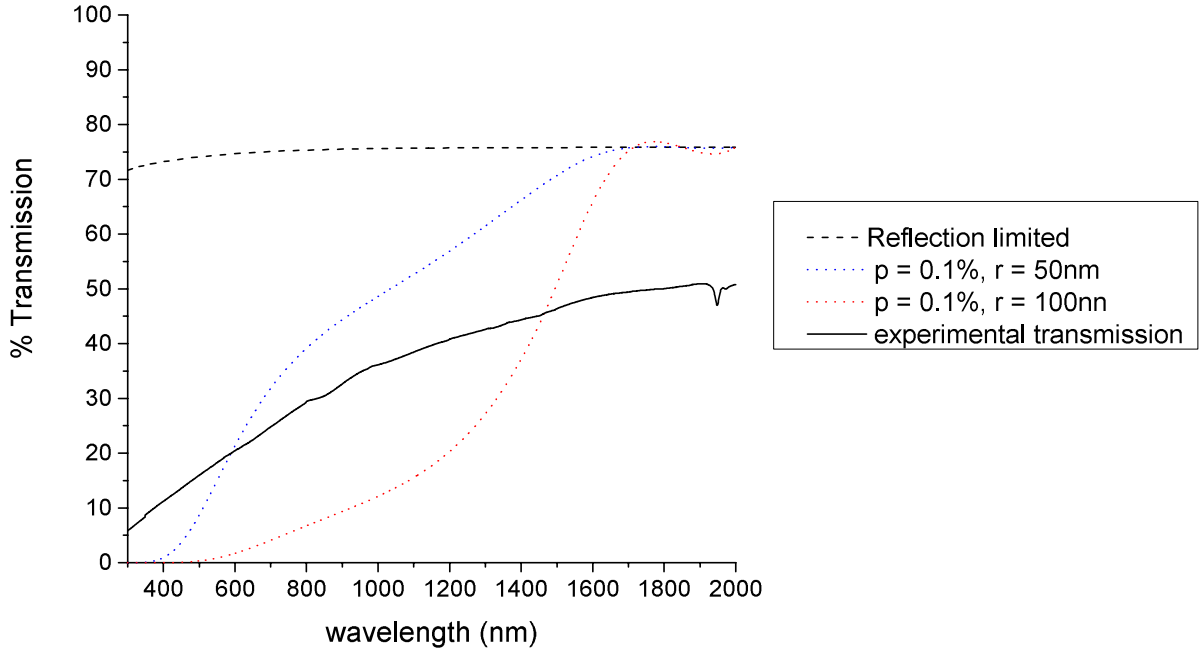

Figure 48 Transmission spectrum from a c-$BaCl_2$ sample pressed at 450ºC compared to two theoretial Mie scattering curves accounting for porosity at a level of 0.1% and a size of 50 and 100nm respectively.

In conclusion, uncertainties about the microstructure, which is difficult to characterize due to the hygroscopic nature of $BaCl_2$, and the multiple contributions to the transmission prevent the application of simple scattering models to describe the transmittance of $BaCl_2$ ceramic samples.

5.1.2 Broadband IR transmission

For qualitative assessment of optical homogeneity, the same samples from Figure 37 were imaged using a thermal camera and presented in Figure 49. A hot-plate, used as a broadband IR source, was placed 8" behind the samples and a metallic grid was placed 2" in front of the source.

The grid is clearly visible in four of the five samples, with no aberrations in the grid pattern when viewed through the samples.

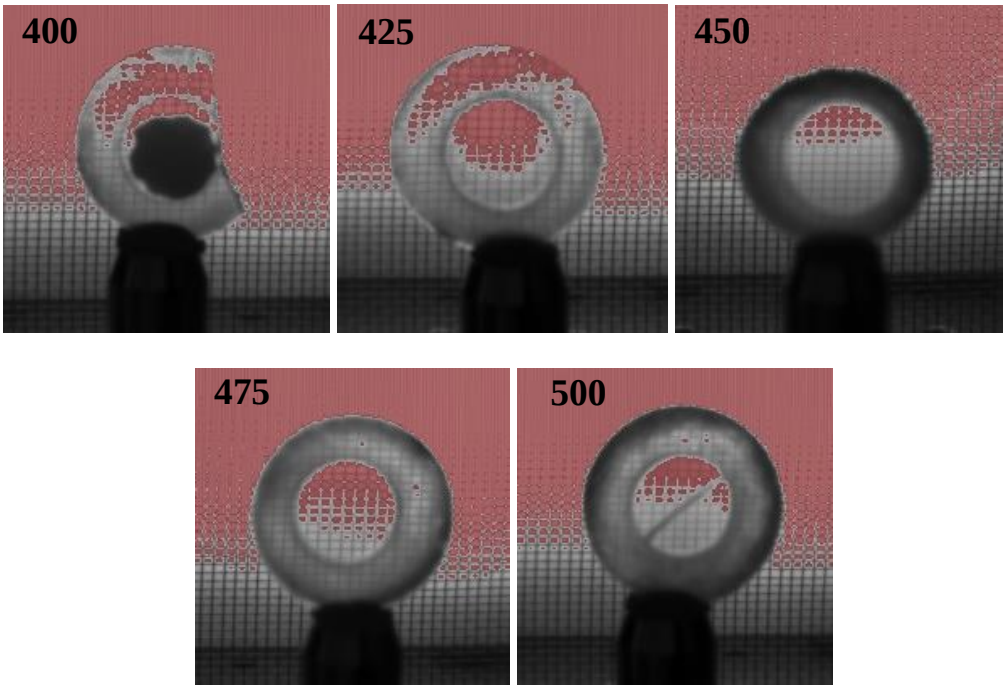

Figure 49 Broadband IR transmission photographs showing a cold metallic grid positioned 6 in behind the samples.

The color gradient arises from thermal inhomogeneities and is not interpreted as any effect on sample homogeneity. The main observation is that even with limited translucency in the visible spectrum (Figure 37), samples have good IR transmittance. Samples, which display some non-uniformity in visible-spectrum photographs (cloudy around the edges) do not display the same effects in the IR.

5.1.3 Spectroscopic studies

The samples prepared for spectroscopic and scintillation studies are pictured in Figures 50-52. Sample EU1, which has been prepared from a melt of 5 wt. % $EuCl_2$ in $BaCl_2$, displays good transparency and glows under a UV lamp. Sample EU2 in Figure 51 has been produced from material mechanically mixed before sintering and shows a slightly higher transparency (less brown coloration).

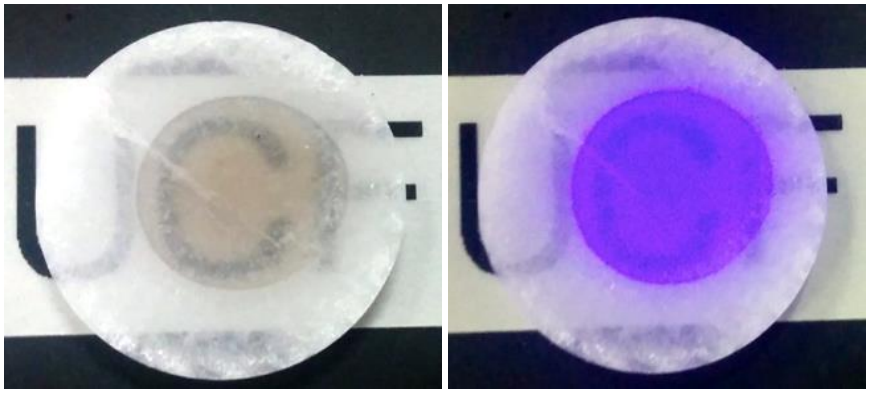

Figure 50 A 1.5 mm thick Eu:$BaCl_2$ sample (EU1) produced from a $EuCl_2$-$BaCl_2$ melt. The left image is taken under UV excitation.

Finally, Figure 52 shows the sample produced from a high quality single crystal grown at LBL (UCF031716, EU3). Pictured alongside EU3 is a Eu:$BaCl_2$ sample prepared from mechanically mixed powders and sintered in the commercial hot-press at 750^{o}C (EU4). This sample exhibits strong dark coloration just like the pure $BaCl_2$ samples pressed in the commercial furnace.

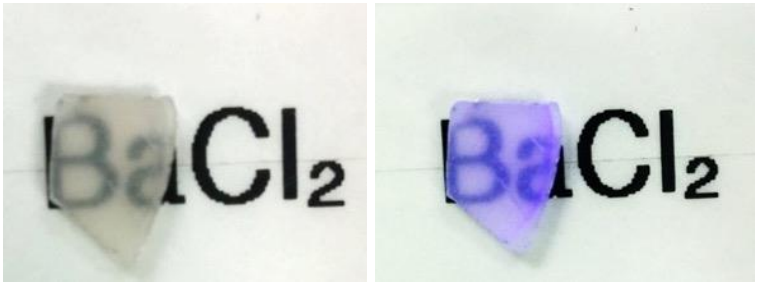

Figure 51 Photographs of 4 mm-diameter sample EU2 produced by mechanical mixing of $EuCl_2$ and $BaCl_2$ powders before sintering. The right hand image show the sample under UV lamp excitation

The spectral response of Eu:$BaCl_2$ was evaluated using excitation sources in the UV (intra-bandgap excitation), as well as in the x-ray regime (across bandgap excitation).

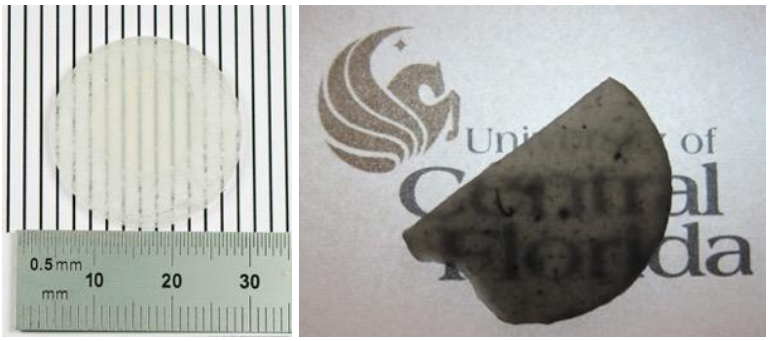

Figure 52 **Sample EU3 prepared from a crushed high-quality single crystal (left) and sample EU4 prepared in the commercial hot-press (right).**

The first sample tested is EU4. Emission spectra using both λ_{exc}=320 nm (optical excitation, OE) and x-ray (x-ray radioluminescence, XRL) are presented in Figure 53.

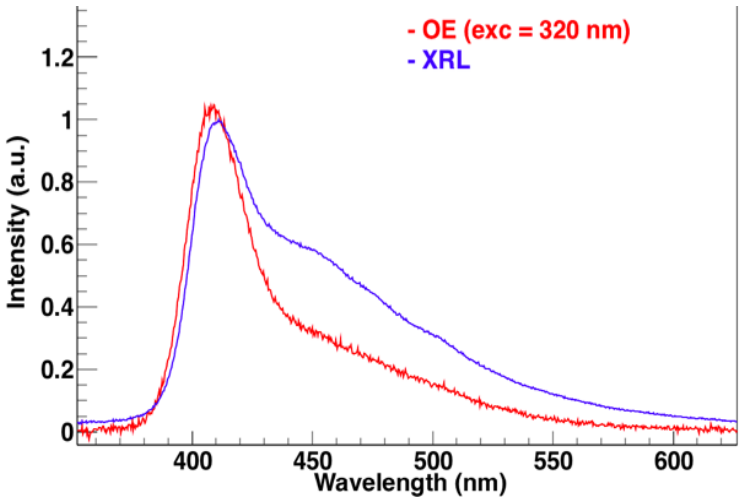

Figure 53 Emission spectra from an early Eu:$BaCl_2$ sample

The Eu^{2+} emission peak centered at 410 nm is present, but additional contributions lead to the asymmetric shape. Such a shape has been correlated to oxygen-based defect centers [159]. While contaminated with oxygen, this sample however does not show any sign of Eu^{3+} emission (611 nm emission). This result is consistent with the hypothesis that the samples pressed at high temperature in the commercial press are susceptible to oxygen contamination.

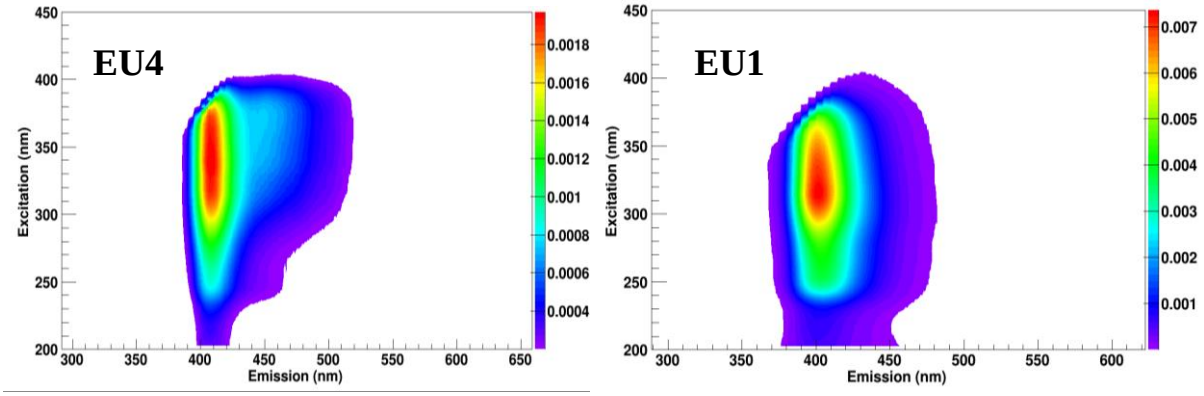

Figure 54 Excitation of luminescence spectra for Eu:$BaCl_2$ ceramic sample EU4 (left) and EU1 (right) showing improvement in phase-change sintering conditions to eliminate oxygen-mediated luminescence.

As the phase-change sintering process was developed and carried out under completely controlled conditions, luminescence and excitation of luminescence studies were performed to monitor the quality of the samples. Figure 54 shows the evolution of optically-excited emission spectra in two Eu:$BaCl_2$ ceramic samples (EU4 and EU1, respectively). The x-axis shows the emission while the y-axis shows the different excitation wavelengths. Intensity is given by the color scale on the right hand axis. The former sample has been processed with the powder exposed to ambient air during the pressing. The latter sample has been processed in the newly designed atmosphere-controlled press, avoiding exposure to air throughout the process. It is clear that the development of the atmosphere controlled hot-pressing chamber for phase change sintering has reduced the emission tail due to oxygen defects ($\lambda_{emission}$~475 nm). In conclusion, luminescence has been a helpful probe in judging the defect content and cleanliness of the ceramic fabrication process.

5.1.4 Thermo-stimulated luminescence studies

The emission spectrum measured at room temperature (298 K), does not tell the whole story of the oxygen and vacancy defects. Defects might not only act as emission centers, but also optical traps disrupting the energy transfer process. The method utilized to study traps is thermally stimulated luminescence (TSL). In this method, the emission is measured as a function of temperature (from cryogenic up to just above room temperature) and as such the signatures showing up in TSL plots correlate to the thermal energy required to empty the trap and allow the electron-hole pair to recombine on a luminescent center [160]. Figure 56 shows the spectroscopically resolved thermally stimulated luminescence in the temperature range of 25 to 300 K from both doped (EU2) and undoped (CP5) $BaCl_2$ ceramic samples. Here again the colored

scale corresponds to the intensity of the emission. The emission in the Eu-doped sample is slightly less symmetric as observed in Figures 47 and 48. Nevertheless, both samples show the presence of three distinct trapping levels. These traps are also located at different energy than those observed in single crystalline Eu:$BaCl_2$ (Figure 55).

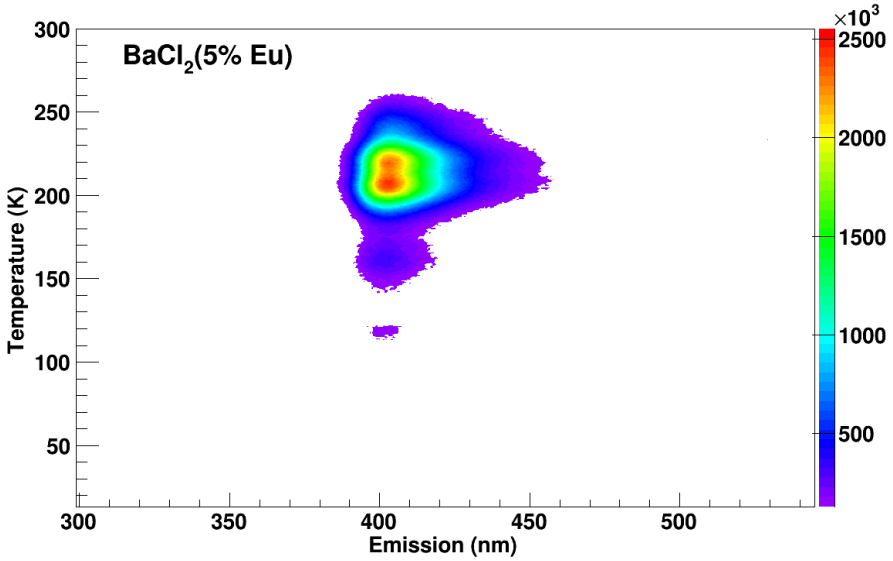

Figure 55 Thermally stimulated luminescence curve for a 5% Eu:$BaCl_2$ single crystal

With this TSL analysis at this single heating rate, the role of these traps in the scintillation process cannot be verified. Nevertheless, the fact that these traps appear at different energies than those we find in single crystalline Eu:$BaCl_2$, suggest we may be dealing with a type of defect not-present in the single crystal.

It is well known that a plastic deformation sintering process will produce a large number of dislocations. The samples studied in this section have not been annealed to relax residual stresses and remove dislocations formed during the pressing. Studying the link between dislocations (residual stress) and optical defects is left for future work. Finally, it was mentioned

in Chapter 1 that the high surface areas of powders can make them more susceptible to contamination. It is also left for future work to determine if the source of these traps is an impurity.

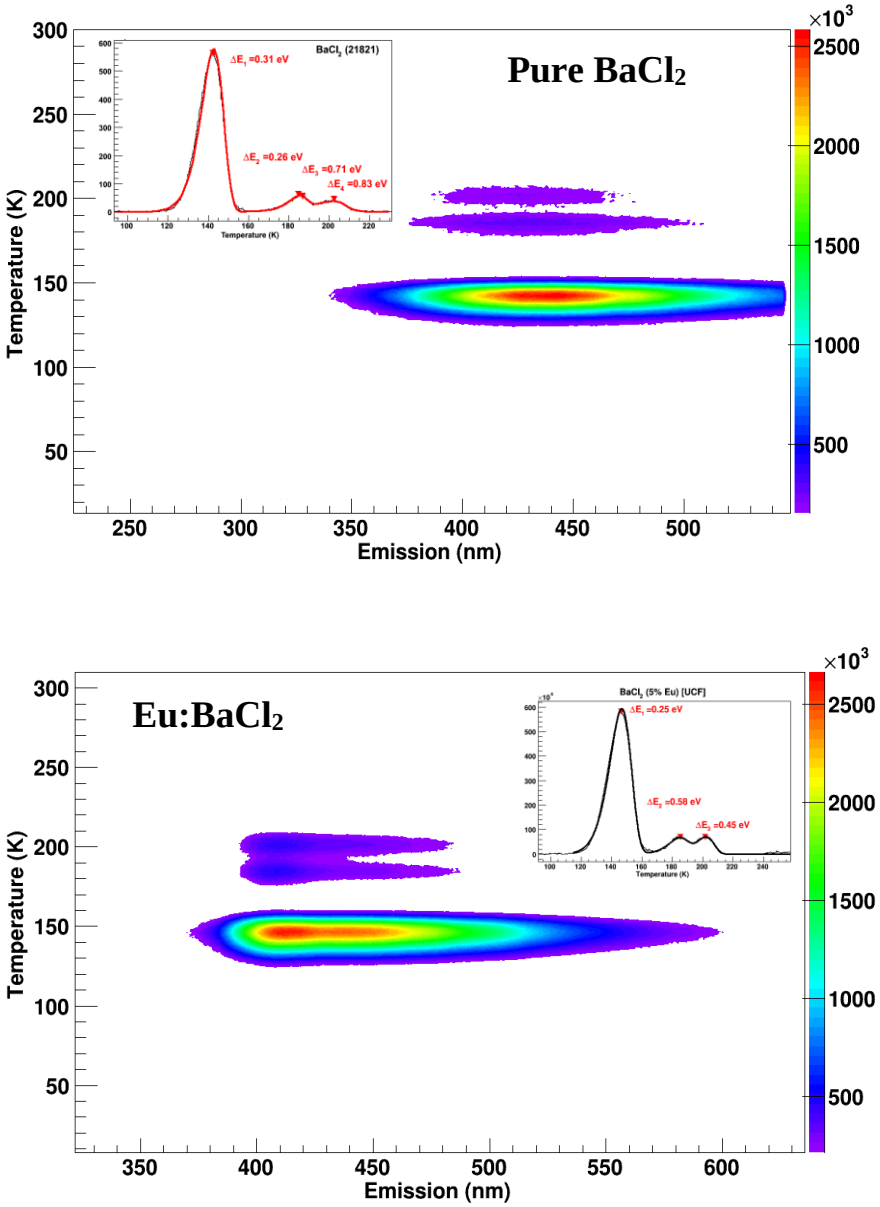

Figure 56 Thermally stimulated luminescence in pure $BaCl_2$ (top) and Eu:$BaCl_2$ (bottom) ceramics. The inset is the raw TSL data (not spectrally resolved), with the depth of each trap labelled.

5.2 Scintillation behavior of Eu:$BaCl_2$ ceramics

The gamma-ray response of Eu:$BaCl_2$ ceramics derived from three different doping techniques is presented. The technique used is pulse height spectroscopy. A sample is placed in contact with a PMT and covered with Teflon tape to direct all light towards the PMT. An active gamma source (^{137}Cs emitting 662 keV gamma rays in this case) is placed on top of the sample. The response of the PMT in terms of pulse height is amplified and fed into a multichannel analyzer where the pulse height of each successive pulse is placed into a bin. A histogram of these pulse heights is built. In order to relate this response to the energy resolution and light yield of the scintillator, the pulse height spectrum of the sample is related to that of a known standard (Tl:NaI crystal).

Samples EU1-EU3 have been tested for scintillation performance. Sintering conditions were identical between the three samples and as outlined in Chapter 4. Samples have dimensions of 1.5 mm thickness x 13 mm diameter except for EU2, which has been cut into a smaller 3 mm x 3 mm x 1 mm piece. The spectra were measured under 662 keV gamma-ray excitation of a ^{137}Cs source. The photopeak position and the energy resolution of the crystals were determined by fitting the photopeak with a single Gaussian function. The light output was estimated by comparing the response of a Saint- Gobain Tl:NaI (1cm thick x 1cm diameter cylinder) to that of the $BaCl_2$ samples. The light yield of NaI:Tl was taken between 43,000 and 45,000 ph/MeV, a commonly reported value [161]. The spectra were measured with a shaping time of 10 μs.

The pulse-height spectrum of EU2 in Figure 57 shows the first ever measured gamma photopeak on a powder-derived Eu:$BaCl_2$ ceramic. The energy resolution of 21% and light yield of 5000 ph/MeV are quite poor. It is also worth noting that this sample is smaller in area than all others presented in this section, which has been shown to have a strong effect on energy resolution.

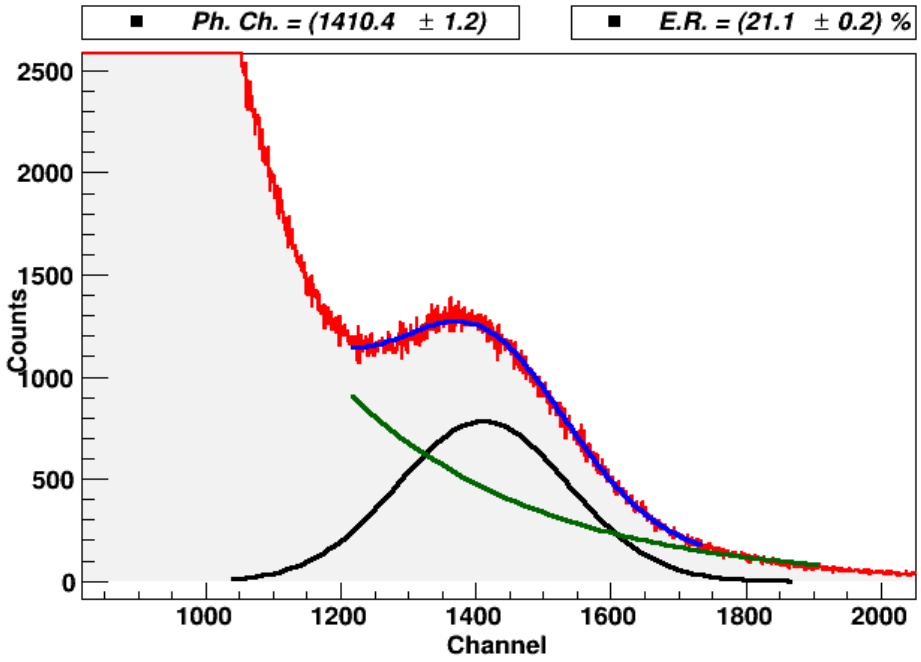

Figure 57 Pulse-height spectrum of sample EU2. The blue fit accounts for a Gaussian profile for the photopeak (black curve) and a noisy pedestal (green curve).

The second set of pulse height spectra compares samples made by the phase change sintering method after incorporation of the dopant at high temperatures (Figure 58). The photopeak in sample EU3 (red curve) is easily discernable, and leads to the calculation of a light yield of 20,000 ph/MeV and an energy resolution of 6%. Surprisingly, sample EU1 exhibits no clear photopeak even though it has been prepared in a very similar manner to EU3.

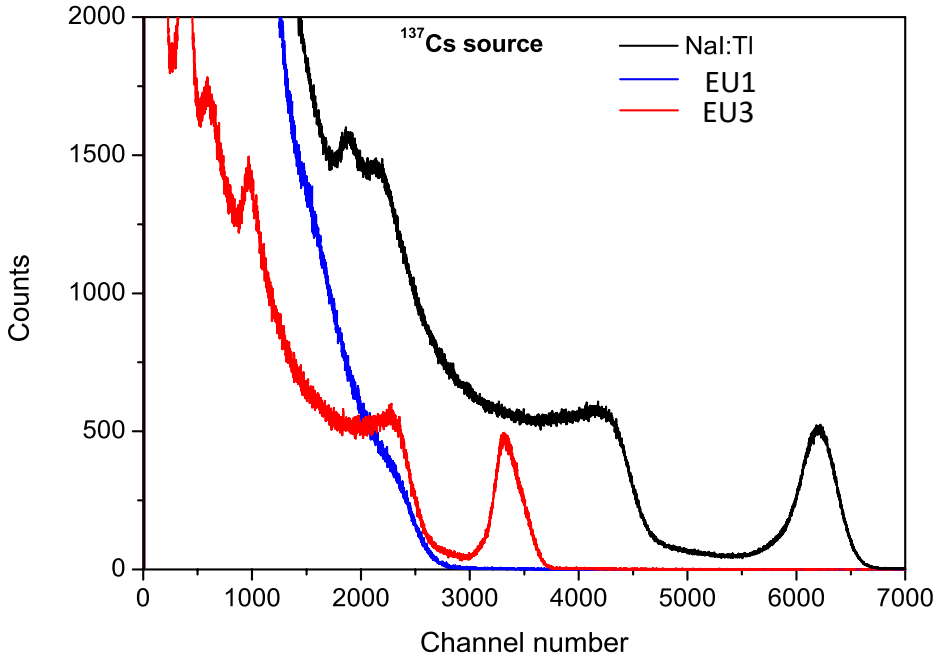

Figure 58 Comparison of the pulse-height spectra of 5% Eu:$BaCl_2$ ceramic samples EU1, EU3, and the Tl:NaI standard.

Thus, the high-quality of the starting material in the case of sample EU3 seems to make a major difference. In sample EU2, the dopant has been incorporated at low temperature and by mechanical mixing. In this case, scintillation performance may suffer due to the dopant not sitting on the Ba^{2+} atomic site of the $BaCl_2$ lattice and perhaps the clustering of $EuCl_2$ inclusions. Light yield and energy resolution can be expected to suffer due to these effects and also those related to the traps visualized in Figure 56. In the case of sample EU1, no photopeak is visible even though dopant incorporation is expected to be more homogeneous. The larger size of sample EU1 compared to EU2 can explain this discrepancy. Furthermore, the coloration in sample EU1 is the strongest of those examined by pulse height spectroscopy. Although complete analysis of trapping

states in these samples by TSL in other methods will be left for future work, it is possible the traps visualized do limit scintillation performance.

Even with some questions still remaining, we have managed to show a marked improvement in light yield and energy resolution under 662 KeV gamma-ray excitation on a limited set of Eu:$BaCl_2$ samples. Spectral analysis methods have been used to correlate this increase in performance to decrease in oxygen-based defects as the phase-change sintering method has been developed. Assessments of the most transparent and highest yield/resolution samples still show the presence of trapping states, even when the emission spectrum is very clean. This calls for a more thorough investigation of both the chemistry of the defects leading to those TSL signatures as well as the role of the traps in the scintillation mechanism.

CONCLUSION

The purpose of this thesis was to demonstrate the fabrication of transparent barium chloride scintillator ceramics by a new sintering method taking advantage of a stress-induced orthorhombic-to-cubic phase change as well as plastic deformation. Initial hot-pressing attempts at high temperatures (850^{o}C) relative to the melting point (962^{o}C) and uniaxial pressures of 45 MPa produced fully-dense translucent samples, which were highly colored. At least a portion of the coloration is related to carbon contamination as examined by Raman spectroscopy. Prior studies also suggest that oxygen impurities and anion vacancies also contribute to this coloration. Analysis of densification curves in light of sintering theory confirms that the densification occurs by plastic flow instead of diffusion transport. However, the role of a phase change in this densification cannot be confirmed without any evidence of residual cubic phase at room temperature after pressing, or any signature in the densification curve.

Further sintering studies were conducted in a better-controlled atmosphere (to limit moisture and oxygen contamination), lower temperature (to prevent point-defect formation), and higher state-of-stress (to initiate the phase change). Implementing these changes in the process has dramatically improved the clarity of the samples. High density were achieved at temperatures of about 450^{o}C and at a state-of-stress set by the application of a 120 MPa nominal load using sodium chloride as a pressure-transmitting medium. Through powder size and morphology studies, it is found that large particles with relatively narrow size distributions (150-300 μm) of both $BaCl_2$ and NaCl favor densification. An exhaustive study of spray-drying of pure and Eu^{2+}-doped $BaCl_2$ solutions has increased our understanding of how to achieve uniformly doped particle aggregates with various morphologies. Unfortunately, the sinterability of these powders is

currently not optimal in the temperature and pressure ranges examined for the phase change technique. Unlike samples pressed at high temperature, samples pressed at low temperature retain a large volume fraction (up to 96 %) of cubic phase after sintering. This is the first evidence that a phase-change sintering mechanism is acting during hot pressing. The amount of retained phase is found to be very sensitive to the pressing temperature. It is also directly correlated to the sample density, grain size, and transparency. The physical conditions leading to phase-change sintering, including the effects of stress intensification, phase conversion and plastic yield in a powder compact, are discussed to outline the specificities of that process and its possible extension to other material systems.

Inline with the original purpose of this thesis, transparent ceramic Eu^{2+}:$BaCl_2$ scintillators were produced and their optical properties were examined. As expected, the ceramic samples are not completely free of optical scattering from birefringent orthorhombic grains and pores, however, transparency is much improved in samples showing a large volume fraction of the cubic phase. In the current development of the process, pulse-height spectra measured with a 662 keV gamma-ray source, Eu:$BaCl_2$ ceramics exhibit a light yield of 20,000 ph/MeV and an energy resolution of 6%, compared to 58,000 and 3.5 % respectively for the single-crystal form.

FUTURE WORK

Phase-change sintering is an effective method for fabricating gamma-ray scintillators of Eu^{2+}-doped $BaCl_2$. The light yield and energy resolution are unprecedented for a halide ceramic scintillator. Nevertheless, there is still much room for improvement to fill the performance gap between the polycrystalline ceramic and single crystal. Studies of Eu^{2+}-doped samples and scintillation characterization only appeared in the latter stages of this work. Future tasks will include coming to a better understanding of the role of impurities and intrinsic defects in the scintillation process. One aspect not explored in this work is the possibility of residual stress (common in hot-pressed parts) playing a role in the scintillation process. It is well known that mechanical stress, by its effect on electronic band structure and defect (dislocation) concentration, can severely reduce and even completely quench the light output from a scintillator [162,163]. It would be key to directly (TEM) or indirectly (electrical conductivity) measure defects and perform residual stress analysis (XRD) as a function of processing and/or post-pressing annealing treatments. In the case of $BaCl_2$, where the phase composition is also believed to be important to the scintillation behavior, the task of studying the effect residual stress is made even more challenging.

Another study, which will be beneficial to improving the scintillation performance is revisiting dopant incorporation by spray-drying. During this thesis, the only successful doping pathway was to incorporate the Eu^{2+} by melting and/or growing a crystal at high temperature. Spray-drying is still a desirable doping pathway because it happens at low temperature and should not suffer from inhomogeneities often observed in grown single-crystals. To proceed on this route, the sinterability of spray-dried powders must be improved. Based on what we have learned

about the role of particle morphology on the sintering, this can be addressed by heat-treating powders to close residual porosity and grow grain size of spray-dried powders.

Besides improving the performance of Eu:$BaCl_2$ scintillator ceramics fabricated by the phase-change sintering technique, there is also room to refine the theory behind the technique and extend the technique to other material systems. The technique itself is still very new and will benefit from the exploration of additional parameter space. Perhaps the most unsatisfying aspect of the experiments described in this thesis work is the lack of accurate pressure measurements. We expect that the phase change requires a large shear component to the stress but we are unable to measure it. The use of gauged dies is one option, but implementing a radial strain gauge to operate at 450^{o}C and the accurate interpretation of the state of stress within the $BaCl_2$-NaCl composite structure is not trivial. Another option is to monitor the stress in-situ using a method such as neutron or x-ray diffraction. Such an experiment would require a highly penetrating probe beam (synchrotron or high-energy neutron) and an experimental setup modified to limit interference from the materials (mainly steel) surrounding the sample. A diffraction method would also have the advantage of pinpointing the instant the phase change occurs during the sintering process. A more simple method for monitoring a martensitic phase transformation and also used commonly in geology and metallurgy [164], is to monitor the acoustic emission from the powder compact during sintering. Bringing any of these additional measurement tools into the process will not only increase our understanding of the phase change in $BaCl_2$ for the betterment of scientific knowledge, but also help identify the unique aspects of phase transition that make it so useful in the context of sintering. We already know that it is important that the phase conversion requires a martensitic component and should lead to a higher symmetry, phase, but what are the other aspects of this transition that make it special?

Barium chloride does have a cousin, $SrBr_2$, which also exhibits a high temperature fluorite phase. Besides being good scintillators or IR windows, these materials are known for their "superionic conductivity" at elevated temperatures. The turning-on-point for superionic conduction has been directly traced to the phase transition [143]. It would be very interesting to see if the stabilization of the cubic phase in either $BaCl_2$ or $SrBr_2$ by the application of phase change sintering would lower the turning-on-point for superionic conduction.

APPENDIX A: PROTOCOL FOR ANALYSIS OF SINTERING CURVES

To relate the densification behavior to the sintering equations outlined in Chapter 1, we must transform the raw data into a strain rate. The strain rate, ε', is determined from the following expressions:

$$h = h_0 + d(t) - d_{base} \tag{A1}$$

$$\mathcal{E}' = -\frac{1}{h}\frac{dh}{dt} \tag{A2}$$

where h_0 is the initial height of the green body measured before the experiment, d(t) is the displacement measured by the sensor, and d_{base} is the baseline displacement curve measured in an empty die. Beginning from the density curve of a high temperature (750°C) hot-pressing experiment in Figure 13, we plot ln(ε') versus ϕP/μ as seen in equations 1.4 and 1.5, whence the exponent on the stress term can be calculated. The value of μ is taken as 7.5 MPa from DFT data [154]. The stress intensification factor is estimated by the Coble relationship as the inverse of the relative density, valid for a random distribution of isolated pores and densities in excess of 95 % [165]. Thus, the calculation should be valid near the maximum pressure, where the density reaches 1. The result shown in Figure 59 estimates a stress exponent, for the latter stage of the densification, between 3 and 4, as indicated by the blue and red linear fits respectively. This most closely matches the expected stress exponent for a plastic deformation mechanism with dislocation glide and climb. This mechanism is only predicted for the very final stages of densification and further examination of the earlier stages with constant low temperature steps will be necessary to identify the mechanisms acting over the entire sintering schedule.

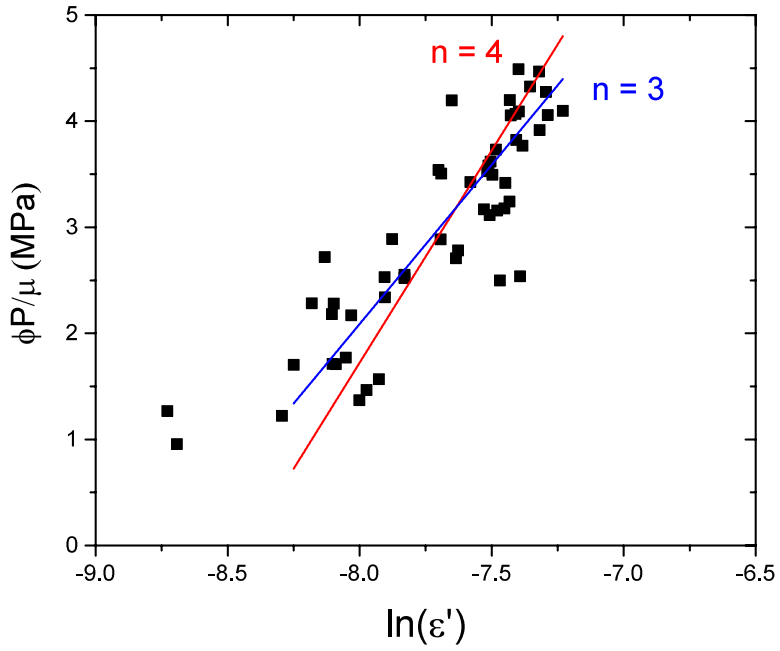

Figure 59 Estimation of the stress exponent in a $BaCl_2$ sintering run at 750°C.

We might think of probing for the densification mechanism in other sections of the curve, for instance in the region of constant increasing temperature and constant pressure in Figure 13. If we assume densification is proceeding by a diffusion mechanism in this temperature range, we can refer to Equation 1.1. First, the diffusion term must be expanded according to Fick's first law.

$$D = D_0 e^{Q/RT} \tag{A3}$$

Here, D_0 is the diffusion coefficient, Q is the activation energy for diffusion, R is the universal gas constant. Because all other terms should be constant in Equation 1.1 except for temperature, it can be re-written as ln(T ε') vs. 1/RT to calculate Q. The Q of 23 kJ/mol calculated in Figure 60 compares to an activation energy of 57 kJ/mol for ionic diffusion calculated from the curve presented in the publication of Hull [143]. These values falling in the same order of magnitude is not enough to confirm or deny a sintering mechanism by diffusive transport.

Application of any of the expressions to the sintering curves require many assumptions. The densification under 750°C and 45 MPa hot-pressing conditions could be driven by a combination of particle re-arrangement, particle fracture, plastic deformation, and diffusional flow. The current attempt on densification modeling has not gone far enough to definitively state the sintering mechanism of $BaCl_2$.

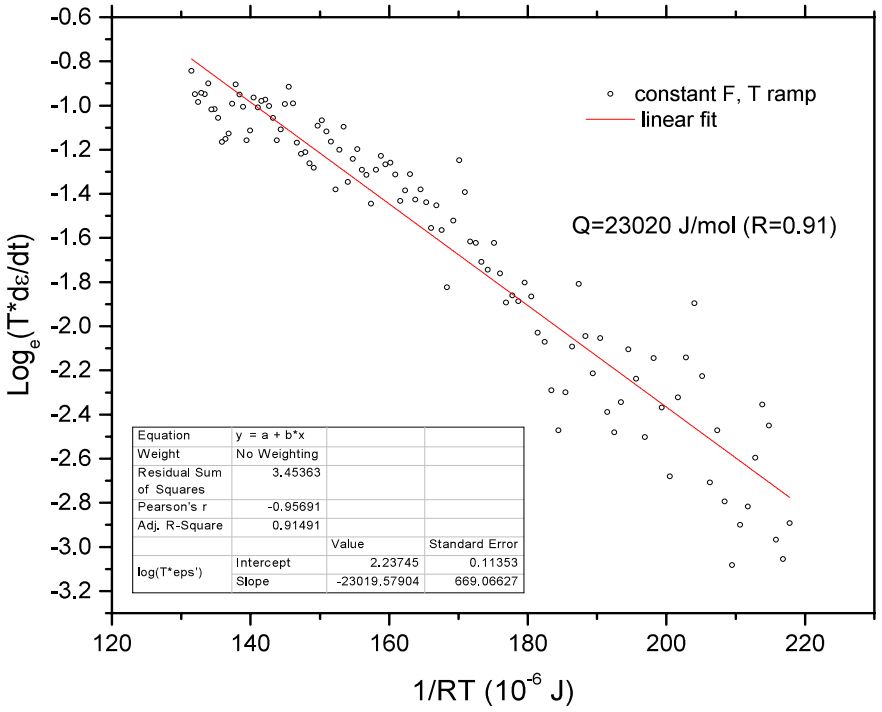

Figure 60 Activation energy for diffusion derived from a plot of the re-arranged of Equation 1.2 or 1.3 with an expanded diffusivity term.

For the sintering experiments conducted in the newly designed hot-press, the extraction of a smooth and consistent strain rate curve is difficult on account of the stepwise, manual pressure application. Thus, analysis of the stress exponent, activation energy, or any other constant from the strain rate equations is challenging in these experiments. The presence of the NaCl pressure-

transmitting medium further complicates the analysis. During this thesis, a die filled with the same mass of loose NaCl typically used in a $BaCl_2$ sintering experiment was used as the background. Because of the difference in geometry between the background and experiment, this method may not be sufficient. For these reason, calculation of stress exponents and analysis of sintering mechanism was not attempted for curves collected during experiments run in the newly designed press.

One additional calculation we did find helpful is the effective Young's modulus of the powder compact. In the case where temperature and pressure schedule are constant and only the powder characteristics are varied, the Young's modulus can be related to the sinterability of the powder. The Young's modulus is calculated as the slope of a stress-strain curve. These stress strain curves calculated for a range of $BaCl_2$ particle sizes are shown in Figure 61.

The curves show a low effective young's modulus at the beginning, which is consistent with the so called stage one sintering dominated by particle rearrangement and the beginning of particle fracture. The higher effective young's modulus during stage one in the sample with the smaller beginning crystallite size (SD1) indicates a higher threshold to begin fracture of particles due to both smaller crystallite size and smoother particle surfaces in the spherical spray-dried powders versus the irregularly shaped CP series powders. In the second and third stages of compaction, sample CP11 shows a gradual increase in effective young's modulus moving towards a very steep section of the stress-strain curve. This is interpreted as the plastic deformation up to the point full densification is reached (modulus becomes very large). On the contrary, the stress strain curve of sample SD1 shows a fairly consistent and steep slope beginning from around 150 MPa, indicating that the plastic deformation of individual particles requires a higher resolved stress.

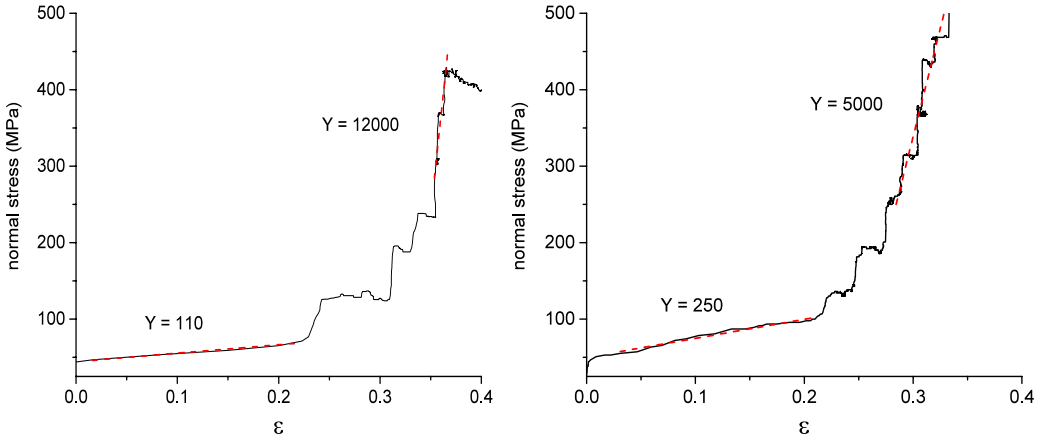

Figure 61 Stress-strain curves for sintering runs using coarse $BaCl_2$ powders (CP11) and spray-dried powders (SD1). The effective Young's modulus calculated by a linear fit to both the particle rearrangement stage and the latter stage of densification.

APPENDIX B: FULL DERIVATION OF POWDER YIELD LOCUS

Beginning from the chemical potential of the mixed system

$$\mu = \lambda_\alpha \mu_\alpha + (1 - \lambda_\alpha)\mu_\beta + E_{coh}(\lambda_\alpha) \tag{A5}$$

where λ_α is the state of advancement of the alpha (o-$BaCl_2$ phase), μ_n is the chemical potential of either the alpha (o-$BaCl_2$) or beta (c-$BaCl_2$) phase, and E_{coh} is the coherence energy. For a system under stress, the chemical potential is shifted to account for the elastic energy:

$$\mu = \mu_0 - \frac{1}{2} S_{klmn} \sigma_{mn} \sigma_{kl} \tag{A6}$$

where μ_0 is the chemical potential in the absence of an applied stress, S_{klmn} is the compliance tensor, σ_{ij} is the stress tensor, and the summation convention is used. At the equilibrium between the two phases: $\frac{d\mu}{d\lambda_\alpha} = 0$. Applying this condition to Equation A6, we write:

$$\mu_\alpha - \mu_\beta + \frac{\partial E_{coh}}{\partial \lambda_\alpha} = 0 \tag{A7}$$

Equation A7 can be expanded:

$$\Delta\mu^o_{\alpha\beta} + \frac{\partial E_{coh}}{\partial \lambda_\alpha} - \frac{1}{2}\left(S^\alpha_{klmn} - S^\beta_{klmn}\right)\sigma_{mn}\sigma_{kl} = 0 \tag{A8}$$

By expliciting the isostatic (σ_{kk}) and deviatoric (s_{kl}) components of the stress:

$$\sigma_{kl} = \frac{1}{3}\sigma_{kk}\delta_{kl} + s_{kl} \tag{A9}$$

one finds:

$$\Delta\mu^0_{\alpha\beta} + \frac{\partial E_{coh}}{\partial \lambda_\alpha} = \left[\frac{1}{2}\Delta S^{\alpha\beta}_{klmn}(\sigma\delta_{nm} + s_{mn})\right][\sigma\delta_{kl} + s_{kl}] \tag{A10}$$

The right hand side can be expanded

$$\frac{1}{2}\Delta S^{\alpha\beta}_{klmn}\sigma^2\delta_{nm}\delta_{kl} + \frac{1}{2}\Delta S^{\alpha\beta}_{klmn}\sigma\delta_{nm}s_{kl} + \frac{1}{2}\Delta S^{\alpha\beta}_{klmn}\sigma\delta_{kl}s_{mn} + \frac{1}{2}\Delta S^{\alpha\beta}_{klmn}s_{mn}s_{kl} \tag{A11}$$

where the Kronecker delta functions simplify the compliance tensors in each term

$$\frac{1}{2}\Delta S^{\alpha\beta}_{kkmm}\sigma^2 + \frac{1}{2}\Delta S^{\alpha\beta}_{klmm}\sigma s_{kl} + \frac{1}{2}\Delta S^{\alpha\beta}_{kkmn}\sigma s_{mn} + \frac{1}{2}\Delta S^{\alpha\beta}_{klmn}s_{mn}s_{kl} \tag{A12}$$

$\Delta S_{kkmm}^{\alpha\beta}$ is equivalent to the difference in isothermal compressibility between the two phases, thus

$$\Delta S_{kkmm}^{\alpha\beta} = \Delta\kappa^{\alpha\beta} \tag{A13}$$

The other terms of A12 can be expanded and simplified. First

$$\Delta S_{kkmm}^{\alpha\beta} = \Delta S_{1111}^{\alpha\beta} + \Delta S_{2222}^{\alpha\beta} + \Delta S_{3333}^{\alpha\beta} + 2\left(\Delta S_{1122}^{\alpha\beta} + \Delta S_{1133}^{\alpha\beta} + \Delta S_{2233}^{\alpha\beta}\right) \tag{A14}$$

Due to the symmetry of the tensor. Because our orthorhombic and cubic phases are orthotropic, there are only 9 independent, non-zero terms to the compliance tensor such that kl=mn or k=l and m=n. Thus:

$$\Delta S_{klmm}^{\alpha\beta} s_{kl} = \left(\Delta S_{1111}^{\alpha\beta} + \Delta S_{1122}^{\alpha\beta} + \Delta S_{1133}^{\alpha\beta}\right)s_{11} + \left(\Delta S_{2211}^{\alpha\beta} + \Delta S_{2222}^{\alpha\beta} + \Delta S_{2233}^{\alpha\beta}\right)s_{22} +$$

$$\left(\Delta S_{3311}^{\alpha\beta} + \Delta S_{3322}^{\alpha\beta} + \Delta S_{3333}^{\alpha\beta}\right)s_{33} \tag{A15}$$

Due to the symmetry in the isotropic powder compact, this is further simplified to:

$$\Delta S_{klmm}^{\alpha\beta} s_{kl} = \Delta S_{1111}^{\alpha\beta}(s_{11} + s_{22} + s_{33}) + 2\Delta S_{1122}^{\alpha\beta}(s_{11} + s_{22} + s_{33}) \tag{A16}$$

Because of the isotropy, the trace of the deviatoric stress tensor is zero, and A15 vanishes.

Moving on to the next term of Equation A12

$$\Delta S_{kkmn}^{\alpha\beta} s_{mn} = \left(\Delta S_{1111}^{\alpha\beta} + \Delta S_{2211}^{\alpha\beta} + \Delta S_{3311}^{\alpha\beta}\right)s_{11} + \left(\Delta S_{1122}^{\alpha\beta} + \Delta S_{2222}^{\alpha\beta} + \Delta S_{3322}^{\alpha\beta}\right)s_{22} +$$

$$\left(\Delta S_{1133}^{\alpha\beta} + \Delta S_{2233}^{\alpha\beta} + \Delta S_{3333}^{\alpha\beta}\right)s_{33} \tag{A17}$$

Based on the symmetry of the compliance tensor and the fact that tr(s) = 0, A16 also vanishes. For the final term of Equation A12

$$\Delta S^{\alpha\beta}_{klmn} s_{mn} s_{kl} = \Delta S^{\alpha\beta}_{1111} s^2_{11} + \Delta S^{\alpha\beta}_{2222} s^2_{22} + \Delta S^{\alpha\beta}_{3333} s^2_{33} + \left(\Delta S^{\alpha\beta}_{1122} + \Delta S^{\alpha\beta}_{2211}\right) s_{11} s_{22} + \left(\Delta S^{\alpha\beta}_{1133} + \Delta S^{\alpha\beta}_{3311}\right) s_{11} s_{33} + \left(\Delta S^{\alpha\beta}_{3322} + \Delta S^{\alpha\beta}_{2233}\right) s_{33} s_{22} + \Delta S^{\alpha\beta}_{1212} s^2_{12} + \Delta S^{\alpha\beta}_{1313} s^2_{13} + \Delta S^{\alpha\beta}_{3232} s^2_{23} \quad \text{(A18)}$$

This relationship simplifies to:

$$\Delta S^{\alpha\beta}_{klmn} s_{mn} s_{kl} = \Delta S^{\alpha\beta}_{1111} (s^2_{11} + s^2_{22} + s^2_{33}) + 2\Delta S^{\alpha\beta}_{1122} (s_{11} s_{22} + s_{11} s_{33} + s_{33} s_{22}) + \Delta S^{\alpha\beta}_{1212} (s^2_{12} + s^2_{13} + s^2_{23}) \quad \text{(A19)}$$

A18 can be further simplified by re-arranging the terms according to:

$$\Delta S^{\alpha\beta}_{klmn} s_{mn} s_{kl} = \Delta S^{\alpha\beta}_{1111} (s_{11} + s_{22} + s_{33})^2 + 2(\Delta S^{\alpha\beta}_{1122} - \Delta S^{\alpha\beta}_{1111})(s_{11} s_{22} + s_{11} s_{33} + s_{33} s_{22}) + \Delta S^{\alpha\beta}_{1212} (s^2_{12} + s^2_{13} + s^2_{23}) \quad \text{(A20)}$$

and the first term vanishes. We take advantage of the following identity for isotropic materials:

$$\Delta S^{\alpha\beta}_{1212} = 2(\Delta S^{\alpha\beta}_{1111} - \Delta S^{\alpha\beta}_{1122}) \quad \text{(A21)}$$

such that A20 simplifies to:

$$\Delta S^{\alpha\beta}_{klmn} s_{mn} s_{kl} = \Delta S^{\alpha\beta}_{1212} (s^2_{12} + s^2_{13} + s^2_{23} - (s_{11} s_{22} + s_{11} s_{33} + s_{33} s_{22})) \quad \text{(A22)}$$

By definition, the second stress invariant for the deviatoric tensor is:

$$J_2 = \frac{1}{2}(s^2_{11} + s^2_{22} + s^2_{33}) + s^2_{12} + s^2_{23} + s^2_{13} \quad \text{(A23)}$$

The stress terms of Equation A22 can be re-arranged to satisfy:

$$(s_{11} s_{22} + s_{11} s_{33} + s_{33} s_{22}) = -(s_{11} + s_{22} + s_{33})^2 + s^2_{11} + s^2_{22} + s^2_{33} \quad \text{(A24)}$$

And combining A23-A24, we get:

$$\Delta S^{\alpha\beta}_{klmn} s_{mn} s_{kl} = \Delta S^{\alpha\beta}_{1212} J_2 \quad \text{(A25)}$$

Grouping Equations A13 and A24 and accounting for the terms which go to zero, Equation A12 writes:

$$\Delta\mu^0_{\alpha\beta} + \frac{\partial E_{coh}}{\partial \lambda_\alpha} = \frac{1}{2}(\Delta\kappa^{\alpha\beta}\sigma^2 + \Delta S^{\alpha\beta}_{1212} J_2) \tag{A26}$$

Finally, A26 can be re-arranged to take the form of an ellipse. The left-hand term is equivalent to the Gibb's free energy, and is replaced with $\Delta g_{\alpha\beta}$.

$$1 = \left(\frac{\sigma}{\sqrt{\frac{2\Delta g_{\alpha\beta}}{\Delta K^{\alpha\beta}}}}\right)^2 + \left(\frac{\sqrt{J_2}}{\sqrt{\frac{2\Delta g_{\alpha\beta}}{\Delta S^{\alpha\beta}_{44}}}}\right)^2 \tag{A27}$$

REFERENCES

[1] C. L. Melcher, J. Nucl. Med. **41**, 1051 (2000).

[2] CMS Collaboration, J. Instrum. **8**, 1 (2013).

[3] A. Nikitin and S. Bliven, IEEE Nucl. Sci. Symp. Conf. Rec. 1214 (2010).

[4] T. Valentine, *Overview of Nuclear Detection Needs for Homeland Security* (2001).

[5] S. Derenzo and G. Bizarri, Nucl. Instruments Methods Phys. Res. A **652**, 247 (2011).

[6] E. D. Bourret-Courchesne, G. A. Bizarri, R. Borade, G. Gundiah, E. C. Samulon, Z. Yan, and S. E. Derenzo, J. Cryst. Growth **352**, 78 (2012).

[7] P. A. Rodnyi, *Physical Processes in Inorganic Scintillators* (CRC Press , Boca Raton, FL, 1997).

[8] P. Lecoq, A. Annenkov, A. Gektin, M. Korzhik, and C. Pedrini, *Inorganic Scintillators for Detector Systems* (Springer, The Netherlands, 2006).

[9] P. Dorenbos, J. Lumin. **104**, 239 (2003).

[10] P. Dorenbos, Ieee Trans. Nucl. Sci. **57**, 1162 (2010).

[11] R. Hofstadter, Phys. Rev. **75**, 796 (1949).

[12] M. Laval, M. Moszyński, R. Allemand, E. Cormoreche, P. Guinet, R. Odru, and J. Vacher, Nucl. Instruments Methods Phys. Res. **206**, 169 (1983).

[13] C. Plettner, G. Pausch, F. Scherwinski, C. M. Herbach, R. Lentering, Y. Kong, K. Römer, M. Grodzicka, T. Szcześniak, J. Iwanowska, and M. Moszyński, J. Instrum. **8**, P06010 (2013).

[14] C. M. Combes, P. Dorenbos, C. W. E. van Eijk, K. W. Krämer, and H. U. Güdel, J. Lumin. **82**, 299 (1999).

[15] N. J. Cherepy, G. Hull, A. D. Drobshoff, S. A. Payne, E. van Loef, C. M. Wilson, K. S. Shah, U. N. Roy, A. Burger, L. A. Boatner, W.-S. Choong, and W. W. Moses, Appl. Phys. Lett. **92**, 83508 (2008).

[16] R. Hofstadter, US3373279 A (12 March 1968).

[17] D. Singh, Phys. Rev. B **82**, 155145 (2010).

[18] E. Sakai, IEEE Trans. Nucl. Sci. **34**, 418 (1987).

[19] Z. Yan, G. Gundiah, G. A. Bizarri, E. C. Samulon, S. E. Derenzo, and E. D. Bourret-Courchesne, Nucl. Instruments Methods Phys. Res. Sect. A Accel. Spectrometers, Detect. Assoc. Equip. **735**, 83 (2014).

[20] J. W. McCauley, P. Patel, M. Chen, G. Gilde, E. Strassburger, B. Paliwal, K. T. Ramesh, and D. P. Dandekar, J. Eur. Ceram. Soc. **29**, 223 (2009).

[21] M. Rubat du Merac, H.-J. Kleebe, M. M. Müller, and I. E. Reimanis, J. Am. Ceram. Soc. **96**, 3341 (2013).

[22] A. Krell, J. Klimke, and T. Hutzler, J. Eur. Ceram. Soc. **29**, 275 (2009).

[23] J. Sanghera, S. Bayya, G. Villalobos, W. Kim, J. Frantz, B. Shaw, B. Sadowski, R. Miklos, C. Baker, M. Hunt, I. Aggarwal, F. Kung, D. Reicher, S. Peplinski, A. Ogloza, P. Langston, C. Lamar, P. Varmette, M. Dubinskiy, and L. Desandre, Opt. Mater. (Amst). **33**, 511 (2011).

[24] A. Ikesue and Y. L. Aung, Nat. Photonics **2**, 721 (2008).

[25] P. A. Ballea, A. S. Uganuma, F. D. Ruon, J. H. Ostalrich, P. G. Eorges, P. G. Redin, and M. M. Ortier, Optica **2**, 288 (2015).

[26] C. C. C. Willis, J. D. Bradford, J. Haussermann, E. McKee, E. Maddox, L. Shah, R. Gaume, and M. Richardson, Opt. Mater. Express **5**, 1389 (2015).

[27] C. Greskovich and S. Duclos, Annu. Rev. Mater. Sci. **27**, 69 (1997).

[28] E. Zych, C. Brecher, a. J. Wojtowicz, and H. Lingertat, J. Lumin. **75**, 193 (1997).

[29] T. Yanagida, H. Takahashi, T. Ito, D. Kasama, T. Enoto, M. Sato, S. Hirakuri, M. Kokubun, K. Makishima, T. Yanagitani, H. Yagi, T. Shigeta, and T. Ito, IEEE Trans. Nucl. Sci. **52**, 1836 (2005).

[30] S. R. Podowitz, R. M. Gaumé, and R. S. Feigelson, J. Am. Ceram. Soc. **93**, 82 (2010).

[31] A. Fukabori, T. Yanagida, J. Pejchal, S. Maeo, Y. Yokota, A. Yoshikawa, T. Ikegami, F. Moretti, and K. Kamada, J. Appl. Phys. **107**, 73501 (2010).

[32] Z. M. Seeley, J. D. Kuntz, N. J. Cherepy, and S. A. Payne, Opt. Mater. (Amst). **33**, 1721 (2011).

[33] S. M. Loureiro, Y. Gao, and V. Venkataramani, J. Am. Ceram. Soc. **88**, 219 (2005).

[34] E. V. van Loef, W. M. Higgins, J. Glodo, C. Brecher, A. Lempicki, V. Venkataramani, W. W. Moses, S. E. Derenzo, and K. S. Shah, IEEE Trans. Nucl. Sci. **54**, 741 (2007).

[35] N. J. Cherepy, Z. M. Seeley, S. A. Payne, P. R. Beck, O. B. Drury, S. P. O'Neal, K. M. Figueroa, S. Hunter, L. Ahle, P. A. Thelin, T. Stefanik, and J. Kindem, IEEE Trans. Nucl. Sci. **60**, 2330 (2013).

[36] D. J. Wisniewski and L. A. Boatner, Proc. SPIE **6706**, (2007).

[37] S. R. Podowitz, R. M. Gaume, W. T. Hong, A. Laouar, and R. S. Feigelson, IEEE Trans. Nucl. Sci. **57**, 3827 (2010).

[38] H. H. Li, J. Phys. Chem. Ref. Data **9**, 283 (1980).

[39] J. Silbiger, Isr. J. Chem. **3**, 84 (1965).

[40] R. Apetz and M. P. B. van Bruggen, J. Am. Ceram. Soc. **86**, 480 (2003).

[41] B.-N. Kim, K. Hiraga, K. Morita, H. Yoshida, T. Miyazaki, and Y. Kagawa, Acta Mater.

57, 1319 (2009).

[42] M. Atterer, *Gmelin-Handbuch Der Anorganischen Chemie System-Nummer 30, Barium* (Verl. Chemie, Weinheim/Bergstr., 1960).

[43] T.-C. Wen and D. K. Shetty, J. Am. Ceram. Soc. **98**, 829 (2015).

[44] Z. A. Munir, U. Anselmi-Tamburini, and M. Ohyanagi, J. Mater. Sci. **41**, 763 (2006).

[45] E. A. Olevsky, S. Kandukuri, and L. Froyen, J. Appl. Phys. **102**, 114913 (2007).

[46] X.-H. Wang, P.-L. Chen, and I.-W. Chen, J. Am. Ceram. Soc. **89**, 431 (2006).

[47] M. Zhuravleva, A. Burger, M. Zhuravleva, L. Stand, H. Wei, C. Hobbs, and L. A. Boatner, in *IEEE Nucl. Sci. Symp. Med. Imaging Conf.* (n.d.).

[48] B. D. Blalock, Spectroscopic , Thermal , and Physical Analysis of the Raw Materials in Europium Doped Cesium Strontium Iodide Scintillator, University of Tennessee, Knoxville, 2013.

[49] J. M. Jewell, M. S. Spess, and J. E. Shelby, J. Am. Ceram. Soc. **73**, 132 (1990).

[50] H. F. Hu and F. Y. Lin, in *C-MRS Int. 1990 Symp. Proc.* (1990), pp. 475–480.

[51] G. Guery, T. Cardinal, A. Fargues, V. Rodriguez, M. Dussauze, D. Cavagnat, P. Thomas, J. Cornette, P. Wachtel, J. D. Musgraves, and K. Richardson, Int. J. Appl. Glas. Sci. **5**, 178 (2014).

[52] D. C. Harris, Proc. SPIE, Wind. Dome Technol. Mater. X **6545**, 654502 (2007).

[53] D. Lezal, J. Optoelectron. Adv. Mater. **5**, 23 (2003).

[54] W. P. Norris, A. L. Olsen, and R. G. Brophy, Appl. Spectrosc. **26**, 247 (1972).

[55] S. Schweizer, U. Rogulis, K. S. Song, and J.-M. Spaeth, J. Phys. Condens. Matter **12**, 6237 (2000).

[56] C. Kinoshita, T. Sonoda, and A. Manabe, Philos. Mag. A **78**, 657 (1998).

[57] Y. Wu, L. A. Boatner, A. C. Lindsey, M. Zhuravleva, S. Jones, J. D. Auxier, H. L. Hall, and C. L. Melcher, Cryst. Growth Des. **15**, 3929 (2015).

[58] L. A. Boatner, J. O. Ramey, J. A. Kolopus, J. S. Neal, N. J. Cherepy, P. R. Beck, S. A. Payne, A. Burger, E. Rowe, and P. Bhattacharya, in *Proc. SPIE 9213, Hard X-Ray, Gamma-Ray, Neutron Detect. Phys. XVI*, edited by A. Burger, L. Franks, R. B. James, and M. Fiederle (2014), p. 92130J.

[59] *Private Communication from Edith Bourret-Courchesne* (n.d.).

[60] A. Edgar, J. Zimmermann, H. von Seggern, and C. R. Varoy, J. Appl. Phys. **107**, 83516 (2010).

[61] A. Edgar, M. Bartle, C. Varoy, S. Raymond, and G. Williams, IEEE Trans. Nucl. Sci. **57**, 1218 (2010).

[62] L. Dixie, A. Edgar, and M. Bartle, Phys. Status Solidi **8**, 132 (2011).

[63] A. Azushima, R. Kopp, A. Korhonen, D. Y. Yang, F. Micari, G. D. Lahoti, P. Groche, J. Yanagimoto, N. Tsuji, A. Rosochowski, and A. Yanagida, CIRP Ann. - Manuf. Technol. **57**, 716 (2008).

[64] M. S. Akchurin, T. T. Basiev, A. A. Demidenko, M. E. Doroshenko, P. P. Fedorov, E. A. Garibin, P. E. Gusev, S. V. Kuznetsov, M. A. Krutov, I. A. Mironov, V. V. Osiko, and P. A. Popov, Opt. Mater. (Amst). **35**, 444 (2013).

[65] K. H. Rosette and H. Packer, US 4171400 (1977).

[66] P. Yan, T. J. Boyle, N. S. Bell, M. R. Sanchez, L. A. M. Ottley, and C. C. Chen, *Fabrication of Large-Volume , Low-Cost Ceramic Lanthanum Halide Scintillators for Gamma Ray Detection* (Albuquerque, NM, 2008).

[67] Rice and R. W., J. Am. Ceram. Soc. **55**, 90 (1972).

[68] S. Swider, S. Motakef, A. Datta, and W. M. Higgins, Proc. SPIE **8852**, (2013).

[69] D. Cusano, F. Holub, and S. Prochazka, US4242221 A (30 December 1980).

[70] J. E. Carnall, S. E. Hatch, L. S. Ladd, and W. F. Parsons, US3365271 A (1968).

[71] C.-S. Chang, M.-H. Hon, and S.-J. Yang, J. Mater. Sci. **26**, 1627 (1991).

[72] N. Neuroth and K. Warnach, US 3465074 A (1969).

[73] E. C. Letter, US 3431326 A (1959).

[74] S. P. M. Loureiro, US 7879284 B2 (2007).

[75] R. L. Coble, J. Appl. Phys. **41**, 4798 (1970).

[76] M. N. Rahman, in *Ceram. Process. Sinter.*, 2nd ed. (2003), pp. 470–539.

[77] S.-I. Karato, *Deformation of Earth Materials: An Introduction to the Rheology of Solid Earth* (Cambridge University Press, 2008).

[78] H. Kim and A. J. Moorhead, J Am Ceram Soc **501**, (1990).

[79] R. Goodall, J.-F. Despois, and A. Mortensen, J. Eur. Ceram. Soc. **26**, 3487 (2006).

[80] R. S. Coe, Contrib. to Mineral. Petrol. **26**, 247 (1970).

[81] R. S. Coe and S. H. Kirby, Contrib. to Mineral. Petrol. **52**, 29 (1975).

[82] R. H. J. Hannink, P. M. Kelly, and B. C. Muddle, J Am Ceram Soc **83**, 461 (2000).

[83] A. G. Evans, D. B. Marshall, and N. H. Burlingame, Adv. Ceram. (1980).

[84] C. Ji, V. I. Levitas, H. Zhu, J. Chaudhuri, A. Marathe, and Y. Ma, Proc. Natl. Acad. Sci. **109**, 19108 (2012).

[85] S. Boulfelfel, D. Zahn, O. Hochrein, Y. Grin, and S. Leoni, Phys. Rev. B **74**, 94106 (2006).

[86] J. M. Leger and A. Atouf, J. Phys. Condens. Matter **4**, 357 (1992).

[87] J. M. Léger, J. Haines, and A. Atouf, J. Appl. Crystallogr. **28**, 416 (1995).

[88] A. G. McLellan, Proc. Roy. Soc. A. **307**, 1 (1968).

[89] M.W. Chase, C. A. Davies, J. R. Downey, D. J. Frurip, R. A. McDonald, and A. . Syverud, in *NIST-JANAF Thermochem. Tables* (1985).

[90] R. K. McGEARY, J. Am. Ceram. Soc. **44**, 513 (1961).

[91] R. D. Carneim, Characterization of Uniaxial Compaction in Spray Dried Ceramic Powders, The Pennsylvania State University, 2000.

[92] F. Tuinstra, J. Chem. Phys. **53**, 1126 (1970).

[93] C. Bohley, J.-M. Wagner, C. Pfau, P.-T. Miclea, and S. Schweizer, Phys. Rev. B **83**, (2011).

[94] G. M. Venkatesh and P. Neelakantan, Proceeding Indian Acad. Sci. **64**, 36 (1966).

[95] S. Swider, S. Lam, S. Motakef, E. Donohoe, L. Coers, S. Taylor, and S. Spencer, Nucl. Instruments Methods Phys. Res. Sect. A Accel. Spectrometers, Detect. Assoc. Equip. **784**, 5 (2015).

[96] J. Kelly, J. Phys. E J. Sci. Instruments **2**, 369 (1969).

[97] V. Tyrpekl, C. Berkmann, M. Holzhäuser, F. Köpp, M. Cologna, T. Wangle, and J. Somers, Rev. Sci. Instrum. **86**, 23904 (2015).

[98] J. R. Davis, *ASM Specialty Handbook: Tool Materials* (1995).

[99] M. N. Rahaman, in *Ceram. Process. Sintering, 2nd Ed.* (2003), p. 831.

[100] T. Vasilos and W. Rhodes, in *Sinter. Key Pap.* (Springer Science & Business Media, 2012), p. 759.

[101] B. Xue, L. Calvez, V. Nazabal, X. H. Zhang, G. Delaizir, J. Monnier, G. Martinelli, and Y. Quiquempois, J. Non. Cryst. Solids **377**, 240 (2013).

[102] B. B. Bokhonov, A. V. Ukhina, D. V. Dudina, A. G. Anisimov, V. I. Mali, and I. S. Batraev, RSC Adv. **5**, 80228 (2015).

[103] C. Xie, Phys. Teach. **50**, 237 (2012).

[104] A. C. Bravo, L. Longuet, D. Autissier, J. F. Baumard, P. Vissie, and J. L. Longuet, Opt. Mater. (Amst). **31**, 734 (2009).

[105] S. J. Lukasiewicz, J. Am. Ceram. Soc. **72**, 617 (1989).

[106] B. B. Patel, J. K. Patel, and S. Chakraborty, Recent Pat. Drug Deliv. Formul. **8**, 63 (2014).

[107] M. Serantoni, A. Piancastelli, A. L. Costa, and L. Esposito, Opt. Mater. (Amst). **34**, 995 (2012).

[108] X. . Cao, R. Vassen, S. Schwartz, W. Jungen, F. Tietz, and D. Stöever, J. Eur. Ceram. Soc. **20**, 2433 (2000).

[109] Y. Yamauchi, P. Gupta, K. Sato, N. Fukata, S. Todoroki, S. Inoue, and S. Kishimoto, J. Ceram. Soc. Japan **117**, 198 (2009).

[110] V. N. Daggupati, G. F. Naterer, K. S. Gabriel, R. J. Gravelsins, and Z. L. Wang, Int. J. Hydrogen Energy **36**, 11353 (2011).

[111] G. Brenn, T. Wiedemann, D. Rensink, O. Kastner, and A. L. Yarin, Chem. Eng. Technol. **24**, 1113 (2001).

[112] J.-C. Lin and J. W. Gentry, Aerosol Sci. Technol. **37**, 15 (2003).

[113] M. H. Sadafi, I. Jahn, A. B. Stilgoe, and K. Hooman, Int. J. Heat Mass Transf. **78**, 25 (2014).

[114] D. H. Charlesworth and W. R. Marshall, A.I.Ch.E. J. **6**, 9 (1960).

[115] D. E. Oakley, Dry. Technol. **22**, 1371 (2004).

[116] M. Eslamian, M. Ahmed, and N. Ashgriz, Dry. Technol. **27**, 3 (2009).

[117] C. S. Handscomb, Simulating Droplet Drying and Particle Formation in Spray Towers, King's College, 2008.

[118] W. J. Walker, J. S. Reed, and S. K. Verma, J. Am. Ceram. Soc. **82**, 1711 (1999).

[119] P. Seydel, J. Blömer, and J. Bertling, Dry. Technol. **24**, 137 (2006).

[120] M. Mezhericher, A. Levy, and I. Borde, Dry. Technol. **28**, 278 (2010).

[121] G. V. Jayanthi, S. C. Zhang, and G. L. Messing, Aerosol Sci. Technol. **19**, 478 (1993).

[122] J. Henning, K. Beckenkamp, and H. D. Lutz, Appl. Spectrosc. **44**, 992 (1990).

[123] R. K. Osterheld and P. R. Bloom, J. Phys. Chem. **82**, 1591 (1978).

[124] R. J. Hunter and R. W. O. Brien, in *Encycl. Surf. Colloid Sci. Vol. 3*, edited by P. Somasundaran (Taylor & Francis, 2005), pp. 2000–2016.

[125] C. A. Schneider, W. S. Rasband, and K. W. Eliceiri, Nat. Methods **9**, 671 (2012).

[126] *Standard X-Ray Diffraction Powder Patterns*, v12 ed. (US Department of Commerce, National Bureau of Standards, 1975).

[127] H. D. Lutz, W. Buchmeier, and B. Engelen, Acta Crystallogr. Sect. B Struct. Sci. **43**, 71 (1987).

[128] L. Gránásy, T. Pusztai, G. Tegze, J. Warren, and J. Douglas, Phys. Rev. E **72**, 11605 (2005).

[129] N. Goldenfield, J. Cryst. Growth **84**, 601 (1987).

[130] N. Dalmaz, H. O. Ozbelge, A. N. Eraslan, and Y. Uludag, Dry. Technol. **25**, 391 (2007).

[131] R. Vehring, Pharm. Res. **25**, 999 (2008).

[132] D. Huang, in *Eur. Dry. Conf. 2011* (2011), pp. 26–28.

[133] M. Huysmans and A. Dassargues, Hydrogeol. J. **13**, 895 (2005).

[134] C. T. Crowe, J. D. Schwarzkopf, M. Sommerfeld, and Y. Tsuji, *Multiphase Flows with Droplets and Particles* (CRC Press, 1997).

[135] K. Masters, *Spray Drying Handbook*, 4th editio (Longman Scientific & Technical, Essex, UK, 1991).

[136] C. Arpagaus and H. Schwartzbach, *Scale-up from the Büchi Mini Spray Dryer B-290 to the Niro MOBILE MINOR* (2008).

[137] R. T. Balmer, *Thermodynamic Tables to Accompany Modern Engineering Thermodynamics* (Academic Press, 2011).

[138] *CRC Handbook of Chemistry and Physics, 93rd Edition* (CRC Press, 2012).

[139] Y.-H. Li and S. Gregory, Geochemical Cosmochem. Acta. **38**, 703 (1974).

[140] *Buchi B-290 Operation Manual, Version G* (n.d.).

[141] W. T. Shoulders, R. Locke, and R. M. Gaume, Rev. Sci. Instrum. **87**, 63908 (2016).

[142] *National Bureau of Standards Monograph 25* (1971).

[143] S. Hull, S. T. Norberg, I. Ahmed, S. G. Eriksson, and C. E. Mohn, J. Solid State Chem. **184**, 2925 (2011).

[144] J. M. Montes, F. G. Cuevas, and J. Cintas, Comput. Mater. Sci. **36**, 329 (2006).

[145] L. C. R. Schneider, Compaction and Yield Behavior of Particulate Materials, University of Leisester, 2003.

[146] F. J. Pérez-Reche, E. Vives, L. Mañosa, and A. Planes, Phys. Rev. Lett. **87**, 195701 (2001).

[147] M. I. Aroyo, J. M. Perez-Mato, D. Orobengoa, E. Tasci, G. de la Flor, and A. Kirov, Bulg. Chem. Commun. **43**, 183 (2011).

[148] M. I. Aroyo, J. M. Perez-Mato, C. Capillas, E. Kroumova, S. Ivantchev, A. Madeariaga, A. Kirov, and H. Wondratschek, Z. Krist **221**, 15 (2006).

[149] M. I. Aroyo, A. Kirov, C. Capillas, J. M. Perez-Mato, and H. Wondratschek, Acta Crystallogr. **A62**, 115 (2006).

[150] D. C. Lagoudas, P. B. Entchev, P. Popov, E. Patoor, L. C. Brinson, and X. Gao, Mech. Mater. **38**, 430 (2006).

[151] D. Chatziathanasiou, Y. Chemisky, F. Meraghni, G. Chatzigeorgiou, and E. Patoor, Shape Mem. Superelasticity **1**, 359 (2015).

[152] A. G. McLellan, Proc. R. Soc. Lond. A. Math. Phys. Sci. **314**, 443 (1970).

[153] M. B. Geilikman, Phys. Chem. Miner. **7**, 1 (1980).

[154] P. Kumar and A. G. Vedeshwar, J. Phys. D. Appl. Phys. **48**, 105301 (2015).

[155] M. de Jong and et. al., Sci. Data **2**, 150009 (2015).

[156] J. G. J. Peelen and R. Metselaar, J. Appl. Phys. **45**, (1974).

[157] T.-C. Wen and D. K. Shetty, J. Am. Ceram. Soc. **99**, 551 (2016).

[158] M. D. Julian and F. Liity, Pysical Rev. B **21**, 1647 (1980).

[159] E. Radzhabov and V. Otroshok, J. Phys. Chem. Solids **56**, 1 (1995).

[160] P. Dorenbos, C. W. E. van Eijk, A. J. J. Bos, and C. L. Melcher, J. Lumin. **60**–**61**, 975 (1994).

[161] I. Holl, E. Lorenz, and G. Mageras, IEEE Trans. Nucl. Sci. **35**, 105 (1988).

[162] R. M. Gaume, S. Lam, M. Gascon, W. Setyawan, S. Curtarolo, and R. S. Feigelson, Rev. Sci. Instrum. **84**, (2013).

[163] M. V. Astakhov, G. S. Belanov, V. G. Vasil'chenko, a. O. Rodin, V. D. Samoilenko, and a. S. Solov'ev, Instruments Exp. Tech. **49**, 637 (2006).

[164] J. A. Simmons and H. N. G. Wadley, J. Res. Natl. Bur. Stand. (1934). **89**, 55 (1984).

[165] R. L. Coble, J. Appl. Phys. **32**, 787 (1961).